2005 SUMMER RESEARCH PROGRAM FOR HIGH SCHOOL JUNIORS

AT THE

UNIVERSITY OF ROCHESTER'S

LABORATORY FOR LASER ENERGETICS

STUDENT RESEARCH REPORTS

PROGRAM COORDINATOR

Dr. R. Stephen Craxton

March 2006   **Laboratory Report 343**

2005 SUMMER RESEARCH PROGRAM FOR HIGH SCHOOL JUNIORS

AT THE

UNIVERSITY OF ROCHESTER'S

LABORATORY FOR LASER ENERGETICS

STUDENT RESEARCH REPORTS

PROGRAM COORDINATOR

Dr. R. Stephen Craxton

LABORATORY FOR LASER ENERGETICS
University of Rochester
250 East River Road
Rochester, NY 14623-1299

During the summer of 2005, 15 students from Rochester-area high schools participated in the Laboratory for Laser Energetics' Summer High School Research Program. The goal of this program is to excite a group of high school students about careers in the areas of science and technology by exposing them to research in a state-of-the-art environment. Too often, students are exposed to "research" only through classroom laboratories, which have prescribed procedures and predictable results. In LLE's summer program, the students experience many of the trials, tribulations, and

rewards of scientific research. By participating in research in a real environment, the students often become more excited about careers in science and technology. In addition, LLE gains from the contributions of the many highly talented students who are attracted to the program.

The students spent most of their time working on their individual research projects with members of LLE's scientific staff. The projects were related to current research activities at LLE and covered a broad range of areas of interest including computational hydrodynamics modeling, cryogenic target fabrication and characterization, liquid crystal chemistry, materials science, the development and control of laser fusion diagnostics, and OMEGA EP Laser System design and engineering. The students, their high schools, their LLE supervisors, and their project titles are listed in the table. Their written reports are collected in this volume.

The students attended weekly seminars on technical topics associated with LLE's research. Topics this year included laser physics, fusion, holographic optics, fiber optics, and femtosecond lasers and their applications. The students also received safety training, learned how to give scientific presentations, and were introduced to LLE's resources, especially the computational facilities.

The program culminated on 24 August with the "High School Student Summer Research Symposium," at which the students presented the results of their research to an audience including parents, teachers, and LLE staff. Each student spoke for approximately ten minutes and answered questions. At the symposium the William D. Ryan Inspirational Teacher award was presented to Mr. Stephen Locke, a chemistry teacher at Byron-Bergen High School. This annual award honors a teacher, nominated by

alumni of the LLE program, who has inspired outstanding students in the areas of science, mathematics, and technology. Mr. Locke had the rare distinction of receiving his nomination from a whole family—Christine Balonek (2002) and her brothers Gregory, Robert, and Daniel (2004).

A total of 191 high school students have participated in the program since it began in 1989. The students this year were selected from approximately 50 applicants. Each applicant submitted an essay describing their interests in science and technology, a copy of their transcript, and a letter of recommendation from a science or math teacher.

In the past, several participants of this program have gone on to become semifinalists and finalists in the prestigious, nationwide Intel Science Talent Search. This tradition of success continued this year with the selection of two students (Frank Fan and Lauren Weiss) as among the 300 semifinalists nationwide in this competition.

LLE plans to continue this program in future years. The program is strictly for students from Rochester-area high schools who have just completed their junior year. Applications are generally mailed out in early February with an application deadline near the end of March. Applications can also be obtained from the LLE website. For more information about the program, please contact Dr. R. Stephen Craxton at LLE.

High School Students and Projects (Summer 2005)			
Name	**High School**	**Supervisor**	**Project Title**
Mary Brummond	Honeoye Falls-Lima	M. J. Guardalben	Correcting Pulse-Front Errors in the OMEGA EP Pulse Compressor
Philip Chang	Pittsford Sutherland	K. L. Marshall	Application of Computational Chemistry Methods to the Prediction of Electronic Structure in Nickel Dithiolene Complexes
Brandon Corbett	Allendale Columbia	T.J.B. Collins/ P. B. Radha	Maximization of Inertial Confinement Fusion Yields Through Laser Pulse Optimization
Adam DeJager	Greece Odyssey	S. F. B. Morse/ R. Kidder	Optical Time Domain Reflectometry for the OMEGA EP Laser
Frank Fan	Webster Schroeder	R. S. Craxton	Investigation of the Effect of a Plastic Ring on the Uniformity of Ice Layers in Cryogenic Inertial Confinement Fusion Targets
Alex Grammar	Brighton	R. Boni/ P. A. Jannimagi	Relative Quantum Efficiency Measurements of the ROSS Streak Camera Photocathode
Stewart Laird	Harley School	J. P. Knauer	Characterization of a High-Energy X-Ray Compound Refractive Lens
Brian MacPherson	Penfield	R. Epstein	Dynamic Energy Grouping in Multigroup Radiation Transport Calculations
Karyn Muir	Honeoye Falls-Lima	J. C. Lambropoulos	Micromechanics and Microstructure of WC Hard Metals
Brian Pan	Penfield	W. Seka	Improving the Illumination Uniformity of a Cryogenic Target with a Layering Sphere
Nicholas Ramos	Palmyra-Macedon	S. Mott/ D. J. Lonobile	X-Ray Framing Camera Characterization Automation
Valerie Rapson	Greece Olympia	K. L. Marshall	Contaminant Resistant Sol-Gel Coatings
Martin Wegman	McQuaid	W. R. Donaldson	Superconducting Electronics for the ICF Environment
Lauren Weiss	Brighton	L. M. Elasky	Categorization and Analysis of Defects in Cryogenic Laser Fusion Targets
Rosie Wu	Brighton	D. H. Edgell	Analysis of Inner Ice Surface Perturbations Using Bright Ring Characterization

Correcting Pulse-Front Errors in the OMEGA EP Pulse Compressor

Mary Brummond

Honeoye Falls-Lima High School
Honeoye Falls, NY

Advisor: Mark Guardalben

Laboratory for Laser Energetics
University of Rochester
Rochester, NY

Correcting Pulse-Front Errors in the OMEGA EP Pulse Compressor

Abstract:

In the Omega EP laser, the pulse must be stretched in time, amplified, and subsequently compressed in a grating compressor in order to obtain high peak power. A model was used to characterize the temporally resolved near-field and far-field beam distributions for several different compressor configurations that included grating alignment errors and grating surface figure errors. The spatio-temporal effect of correcting the compressor output wavefront by use of a deformable mirror (DM) is presented and a trade-off between best spatial and temporal performance is elucidated.

1. Introduction

1.1 Pulse Compression

In order for a short laser pulse to be amplified, it must first be stretched because it may otherwise cause damage to the optics required for amplifying it. After being stretched through time, the pulse must be recompressed. To do this, a pulse compressor consisting of four diffraction gratings is required which will provide for a stretched pulse to be propagated through. In going through the compressor, the wavelengths of the pulse are separated before being focused together. However, since the diffraction gratings required for the pulse compressors need to be quite large, three gratings are placed in series to form each complete diffraction grating. Errors may be caused if the gratings are out of alignment or if there is any curvature on the grating tiles. Misalignment and surface figure errors broaden the pulse and degrade the far-field focal spot. Some error is anticipated because it may not be possible to perfectly align the diffraction tiles.

1.2 Deformable Mirror

Once built, the OMEGA EP laser will be the most powerful laser in the world. The laser will use a femto-second pulse which will be split and amplified before being focused on a target to aid in the creation of fusion reactions with the release of energy. Fusion is being explored as a solution to providing an alternate source of energy. However, the laser pulse may have errors in the wavefront that may affect the efficiency of the laser. The deformable mirror (DM) is useful in correcting any errors in the

wavefront by using a series of pistons to adjust itself to compensate for the wavefront error.
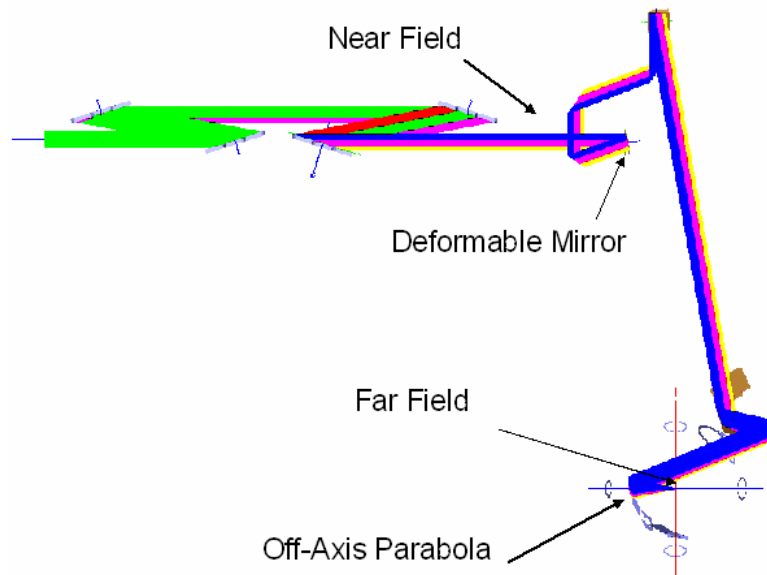
2. Methodology

2.1 FRED

Figure 1 – **Modeling in FRED** – Beams are propagated through the pulse compressor to the deformable mirror and on to the off-axis parabola. The encircled energy and FWHM of the compressor are found at analysis planes in the near field and far field.

FRED is an advanced optical engineering software program capable of simulating the propagation of light through virtually any optical/mechanical system. In this case, FRED was used in order to trace waves at different frequencies as they propagated through the pulse compressor to the deformable mirror and the off-axis parabola (OAP) to the target chamber (see Fig. 1). The OAP is used to focus the beam. The diffraction

gratings were modeled in FRED to conform to a set of design parameters such that the grating pairs were a certain distance apart from one another.

A 30 by 30 beam grid was traced through the compressor, originating from an optical source. Data collection took place at two separate analysis surfaces; one just before the beams hit the DM and the second at the focus of the OAP. These two planes have been designated the near field and far field, respectively. This allowed for observation of the spatial and temporal movement of the pulse in both fields.

Through the use of FRED, error could be applied to the diffraction gratings so that its effect on the pulse could be observed, and numeric feedback on the pulse performance could be calculated. The primary evaluated data were the temporal full width at half maximum (FWHM) and the percent of the pulse energy focused inside a circle of diameter 20 μm (known as the encircled energy). This diameter corresponds to laser rays deviating by 9.58 μrad from the ideal direction.

2.2 MATLAB

Once an error was created in FRED, the data from the near-field and far-field raytraces was used in MATLAB to create graphs of the FWHM and the spatially integrated pulse through time. This was helpful in observing the effect of error on the pulse compression model.

3. Results

In order to properly consider the effect of error upon the grating tiles of the pulse compressor, a "perfect" compressor model was configured in FRED in order to meet up to the proper specifications. Data was collected from the "perfect" raytrace that could be compared to later raytraces in which error was applied on the tiles. The results of the calculated total encircled energy and the FWHM were compared to the desired values. The desired value of total encircled energy is ≥80%; that of the FWHM is ≤1 picosecond (ps). The FWHM of the "perfect" compressor was 523 fs; its total encircled energy was 100% (see Fig. 2).
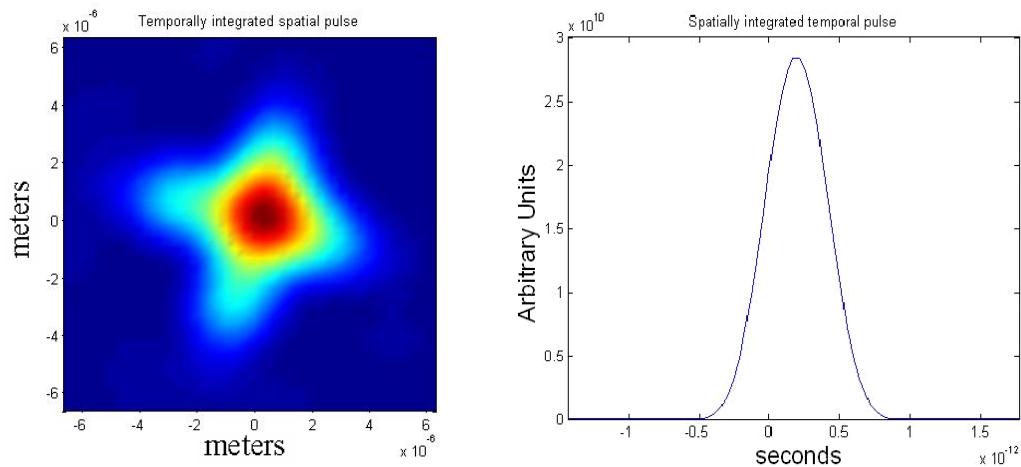
Figure 2 – **"Perfect" Compressor** – The encircled energy of the pulse of the "perfect" compressor may be viewed in the temporally integrated spatial pulse (left). The spatially integrated temporal pulse (right) shows the FWHM of the pulse.

3.1 Tip, Tilt, and In-plane Rotation

The first types of error which were considered when examining the pulse compressor model were those caused by tip, tilt, and in-plane rotation. Tip refers to a
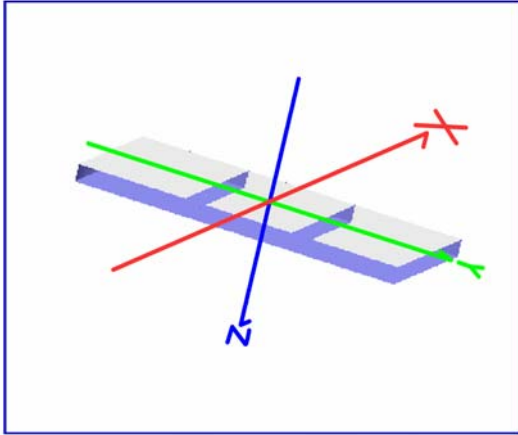
Figure 3 – **Orientation of a Diffraction Grating with three tiles.**

rotation across the horizontal axis. Tilt is the rotation about the vertical axis, and in-plane rotation is rotation about the axis normal to the diffraction grating (see Fig. 3). There already existed pre-determined grating alignment tolerances. For tip, the alignment tolerance was 33 µrad; for tilt the alignment tolerance was 10 µrad and for in-plane rotation, the alignment tolerance was 61 µrad. These errors were applied to each grating plane as well as each of the tiles in the diffraction grating planes. The tiles of the diffraction grating had different tolerances. The tiling tolerance for tip was 0.14 µrad, that of tilt was 0.33 µrad, and that of in-plane rotation was 0.15 µrad.

A "worst-case scenario" model of the pulse compressor was created that applied tip, tilt, and in-plane rotation to the diffraction gratings of the model. The effect of this error on the far field of the laser's focus was that the FWHM was 1.089 ps. This is a very good result, especially when compared to the FWHM of the "perfect" compressor, which was 523 fs. The total encircled energy of the pulse was 27%.

3.2 Tile Shifts

The second type of error that was applied to the compressor model was tile shifts in which the tiles making up the diffraction gratings were moved out of alignment along the horizontal, vertical, or normal axis. The tolerance for tile shifting along any of the x, y, and z axes (see Fig. 3) was 36 nm. In one raytrace which applied the "worst-case"

scenario described in 3.1 to the three tiles making up the diffraction gratings as well as the tile shifts, the error observed was less than that for the "worst-case" scenario when applied to the entire diffraction grating.

3.3 Power on the tiles

Surface error also must be taken into consideration. There is no guarantee that the surface of the diffraction grating tiles will not have some sort of curvature or error on them that will cause error in the pulse front. Quarter-wave concave parabolic curvature (at 1.053 micron wavelength) was applied to each of the three tiles making up each complete diffraction grating to observe the effect of concave and convex curvature on the gratings. Figure 4(a) shows the results of a raytrace that applied the quarter-wave curvature on each of the three tiles in each diffraction grating. The FWHM was found to be 674 fs while the encircled energy was 39.42% in the far field.

It was anticipated that it would perhaps be easier to correct for wavefront error if the curvature errors on the tiles were arranged so that they formed a continuous curve rather than three separate curves. Thus, a raytrace was performed that applied the quarter-wave curvature to each of the diffraction gratings that were altered in FRED so that one large diffraction grating took the place of the three separate tiles. The FWHM of this raytrace was 1.99 ps and the encircled energy was 7.13% in the far field [see Fig. 5(a)]. Both this wave front and the one involving curvature on the three-tiled diffraction grating were applied to the deformable mirror to observe its effect on correcting their error.

One unique observation made in the far field of the single-tiled diffraction grating model with 1.053 micron concave power applied to it was that an astigmatism appeared,

creating two separate but distinct foci. This explains the low encircled energy that was found in this raytrace; the data for the encircled energy was taken at a point between the two foci. It was anticipated that the astigmatism would be corrected for by the DM.
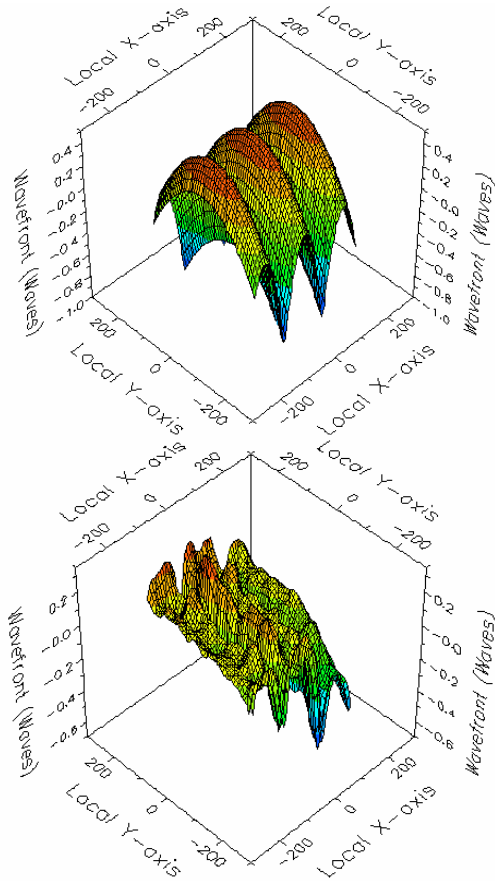
Figure 4 – **The DM corrects for the broadening of the pulse** – The upper image is the wavefront of the pulse when quarter-wave error is applied to the diffraction gratings. The lower wavefront shows the corrections of the DM in narrowing the pulse.

The wavefronts of both scenarios of power applied on the tiles of the diffraction grating were corrected by the deformable mirror [see Figs. 4(b) and 5(b)]. The DM corrects for the concave surface error on the three-tiled diffraction grating model from 39.42% to 75.13% encircled energy in the far-field. However, this still does not meet the desired value of 80% encircled energy. When the wavefront of the single-tiled diffraction grating scenario was applied to the DM, the results were much more promising (see also Fig. 6). The encircled energy that resulted from the raytrace once the corrections of the DM were applied to the compressor model was 87.07%, as opposed to its original 7.13%. This also corrected for the astigmatism that had occurred in the far field. This is significant because if curvature appears on the tiles, then they may be arranged so that they form a continuous curve rather than three separate curves. The DM is able to correct a continuous curve to a greater extent than three separate curves

because it is easier for the pistons to adjust to the single curve. The alternative of pulling

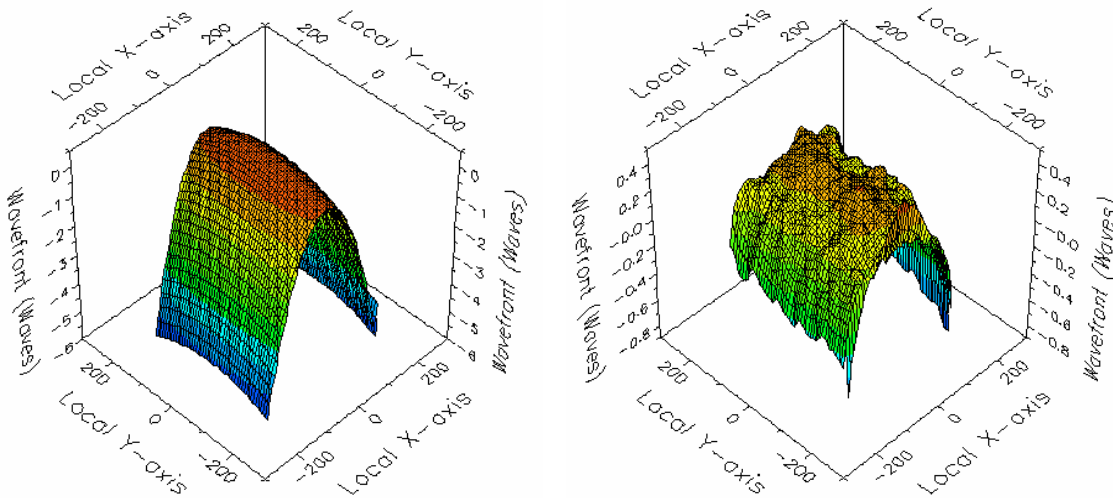the DM in different directions diminishes its effectiveness.

Figure 5 – **The DM corrects better when the power error on the diffraction grating is continuous** – The wavefront of the corrected pulse (right) is narrower and smoother than that of the corrected pulse in Fig. 4. The DM is better equipped to correct for a smooth, continuous error (left).
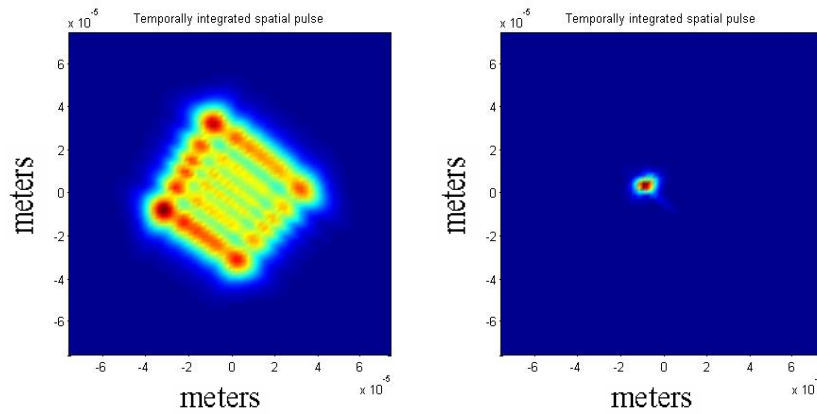

Figure 6 – **The DM is able to correct the encircled energy of the continuous curvature error to within the desired value** – The smearing evident on the uncorrected far field (left) is nearly eliminated when the DM is applied to the wavefront.

Though the DM was able to correct for the encircled energy of the two curvature

scenarios, the temporal FWHM still was not corrected. Though both FWHM's were

within the short-term desired value of 10 ps, eventually scientists will want the FWHM to be within 1 ps. The fact that the DM was incapable of presenting a solution to correcting temporal error in the pulse shows that there exists a trade-off between best spatial and temporal performance.

4. Conclusion/Further Work

Though errors may exist in the pulse compressor, the deformable mirror is able to correct for spatial error in the wavefront. The DM corrects for the concave surface error on the three tiles of the grating to 75% encircled energy at 9.58 μrad while it corrects for the concave parabolic surface error in the single tiled grating to 87%. However, though encircled energy is improved in the single tiled grating, there exists a larger FWHM of 1.93 ps as compared to 671 fs. This shows that a trade-off between best spatial and best temporal performance exists between the two compressor configurations. Thus, though the requirement of 80% encircled energy is met by the corrections found in the single tiled grating raytrace, the FWHM may yet be optimized.

Further work may show improved results. The off-axis-parabola alignment has yet to be optimized; doing so may improve the encircled energy and FWHM of the pulse. In addition, corrections from the DM may be applied to further raytrace scenarios and elucidate the trade-off between spatial and temporal performance and help produce a median between the two.

5. Acknowledgements

I would like to thank Dr. R Stephen Craxton for providing the opportunity to work at the University of Rochester's Laboratory for Laser Energetics as well as my advisor Mark Guardalben. In addition, I would like to thank George Dahl for his work on the MATLAB programs for compiling the data from FRED, Sharyl Abbey and Bryan Krushwitz for their work with the deformable mirror, and Jenny Hamson for her help in creating videos to include in my symposium presentation.

6. References

1. E.B. Tracy, "Optical Pulse Compression With Diffraction Gratings," IEEE J. of Quantum Electronics, vol. QE-5, pp 454-458, September 1969.

2. M. Guardalben, private communication.

Application of Computational Chemistry Methods to the Prediction of Electronic Structure in Nickel Dithiolene Complexes

Philip Chang

Advisor: Kenneth L. Marshall

Laboratory for Laser Energetics
University of Rochester
250 East River Road
Rochester, NY 14623

1. INTRODUCTION

Advances in the science of computational chemistry over the past 20 years, the widespread availability and increasing ease of use of computational chemistry software, and an exponential reduction in the cost and size of extremely powerful computer hardware now make some degree of computational predictive capability for physical properties (e.g. solubility, electronic and vibrational spectra, reactivity, molecular configuration, and chirality) within the reach of nearly every laboratory that is involved in new materials research and development. Previously, researchers out of necessity would have to follow an empirical approach of synthesizing, isolating, characterizing, and purifying hundreds of different compounds in order to establish structure-property relationships that could be used to further direct the design and development effort toward the desired goal. Of these hundreds of compounds synthesized, only a handful would have the necessary combination of physical characteristics to be deemed worthy of further study and development. As can be imagined, this process is extremely time consuming, labor intensive (weeks to months to completely synthesize and characterize each compound), costly, and sometimes highly frustrating for organic chemists engaged in the synthesis of new materials—especially for those with limited resources. Modern hardware and user-friendly software now make it possible to model new compounds and their physical properties with remarkable accuracy within a few hours or days. Only a few years ago it would have taken from weeks to months of work to achieve the same results.

Nowhere has there been more evidence of the predictive capability of computational chemistry than in the pharmaceutical industry, where computational molecular design techniques have been used to great advantage for a number of years in the rapid development of new drugs with enhanced biological activity and specificity at lower cost. More recently, computational

chemical methods have been applied to the molecular engineering and design of liquid crystal materials for use in the multibillion-dollar information display industry and the optoelectronic, photonics, military, scientific, and life sciences sectors. In all of these examples, the vast majority of the target materials systems consist of organic molecules containing combinations of carbon, hydrogen, nitrogen, sulfur, fluorine, and phosphorous, for which the computational algorithms and procedures have been well defined in a large body of existing literature. Modeling of compounds containing other elements (in particular, transition metal organometallics) represents a substantial challenge for several reasons: (1) the scarcity of previous literature references on the subject, (2) the lack of parameter files (basis sets) that can adequately account for the unique nature of the coordinate-covalent bonds that are formed in these materials, (3) the intensive computational resources required to accomplish the calculations, and (4) the scarcity of software capable of modeling organometallics.

In the research described in this paper, a computational modeling methodology employing both molecular mechanics and *ab initio* computational methods was developed and used to calculate the expected electronic absorbance spectra in the near-IR region for both existing and novel zerovalent transition metal dithiolene near-IR dye complexes containing nickel as the central metal atom. This is believed to be the first time that calculations of this nature have been attempted in nickel dithiolene systems, or in any other transition metal organometallic complex. This new computational capability now makes it possible to determine, before synthesis, the effect of structural changes in either the dithiolene core, the ligands (or both) on the physical and optical properties of the complexes and accelerate their development for applications in optical devices.

2. NICKEL DITHIOLENE COMPLEXES

Transition metal dithiolenes are composed of a central metal atom (in this case, nickel) bonded to four sulfur atoms, which in turn are bonded to four carbon atoms to form a square planar geometry (Figure 1) composed of two five-member planar rings (the *dithiolene* core).
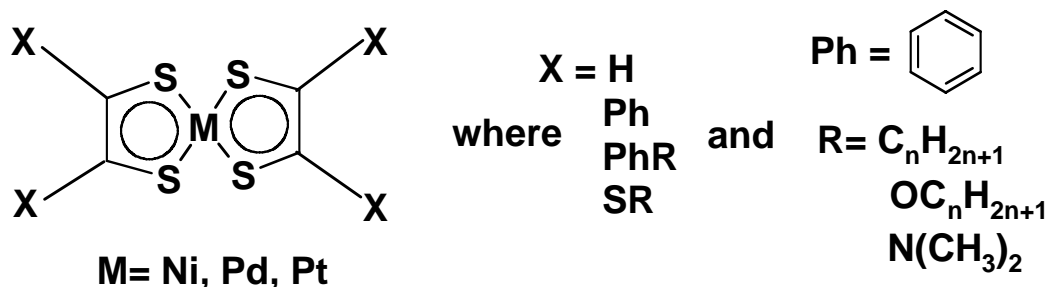

Figure 1. The base structure of the nickel dithiolene system

The metal atom is zerovalent, due to overlap of d-orbitals on the metal with the extended π-electron system of the dithiolene core. As a result, the bonding in the complex is coordinate covalent and possesses very little (if any) ionic character. The high degree of electron delocalization results in a very intense electronic absorbance transition in the near-IR region (600-1600 nm, depending on structure). The zerovalent nature of the complexes makes them highly soluble in nonpolar organic solvents such as benzene, toluene, and hexane, which makes them unique among both metal complexes and other near-IR dyes. The terminal R groups can be selected from a large number of substituents (alkyl, alkoxy, aryl, thioether), and these terminal groups can have a large effect on the physical properties of the complexes.

Nickel dithiolenes are both thermally and photochemically stable, and thus have been of interest for a number of years as passive absorbers in xerography, as Q-switching absorbers for lasers, and for optical power limiting and all-optical switching. Most recently, they are of special interest as dye dopants for liquid crystal near-IR devices for optical modulation, switching and

night vision/avionics imaging. Their high solubility in nonpolar organic solvents also renders them highly soluble in liquid crystals, which is a distinct advantage over other near-IR dyes that are primarily ionic in nature and thus have poor solubility in organic host media. They can also possess liquid crystal phases in their own right, depending on the structure of the complex and the number and position of the functional groups attached. This property is a distinct advantage for use in liquid crystal systems, as it allows them to be used at much higher concentrations in the host material without adversely affecting the unique physical and optical properties of the liquid crystal host. The recent increased technological importance of these materials in near-IR optical modulation devices based on liquid crystals, along with the challenging nature of the modeling task, makes these interesting materials an ideal subject for study.

3. COMPUTATIONAL MODELING TECHNIQUES

Modeling of electronic transition states in organometallic systems represents a significant technical and computational challenge. There is a scarcity of both previous literature references on the subject and, even more significantly, a very limited number of basis sets that adequately account for the unusual coordinate-covalent bonding in these materials. Because of the complexity of the calculations, substantial computational resources are also required.

In general, the process of modeling the electronic absorbance spectra is composed of three key steps:

- Minimization of the free energy of the molecular structure using molecular mechanics methods.

- Determination of the electronic distribution in the molecule and calculation of the available electronic energy levels and excited states.

- Calculation of the allowable ground-state to excited-state transitions that are responsible for the electronic absorbance spectrum.

Molecular mechanics calculations use Newtonian mechanics and empirical force fields to model the potential energy of an atom in its molecular structure. This process examines the chemical bonds of a molecular structure to generate a particular molecular conformation that represents an energy-minimized state with respect to bond angles, electrostatic repulsions, and steric factors. This energy-minimized structure represents an approximate equilibrium conformation that must be further refined using quantum mechanical methods.

The electronic distribution within the molecule and its effect on the energy-minimized equilibrium molecular conformation can be determined by using either semi-empirical or *ab initio* quantum mechanical computation methods. Semi-empirical methods use some approximations in order to achieve reduced computation times. They are used primarily in situations when a certain degree of computational accuracy can be sacrificed in exchange for reduced computational resources and run time. *Ab initio* methods provide a much more detailed and accurate description of the quantum mechanical aspects of a molecular structure, but do so at a cost of increased computational resource requirements and time. The substantially better accuracy of a*b initio* calculations make them the preferred method for modeling the exceedingly complex electronic distribution and excited state transitions found in organometallic compounds.

Ab initio calculations are based on a detailed description of the quantum mechanical aspects of a molecular structure using the Schrödinger equation, defined as

$$H_{op}\Psi = E\Psi$$

where H_{op} is defined as the Hamiltonian operator, Ψ as the wavefunction of the system, and E as the energy of the system. The Hamiltonian of the system represents its kinetic and potential energy. In a three-dimensional system, the Hamiltonian operator is defined as

$$H_{op}\Psi = \frac{-h^2}{8\pi^2 m}\left[\frac{\partial^2\Psi}{\partial x^2} + \frac{\partial^2\Psi}{\partial y^2} + \frac{\partial^2\Psi}{\partial z^2}\right] + U\Psi$$

where h is Planck's constant and m is the mass of an electron. The terms x, y, and z are the Cartesian coordinates of an electron with respect to the nucleus, while U refers to the potential energy of the system.[1]

A wavefunction is a mathematical expression that describes the wave nature of an electron after certain restrictions are placed upon it by basis sets, which give specific information on the electronic structure and orbitals of the atoms as well as describing the path and behavior of electrons. The wavefunction expression is a group of Gaussian Type Orbital (GTO) equations for which the generic equation is

$$\Psi = Nx^l y^m z^n e^{-\alpha r^2}$$

Again, the x, y, and z are the Cartesian coordinates. The variables *l*, *m*, and *n* are positive integer values that describe the angular momentum of the orbital, while r is the distance to the center of the atom. The variable N is the normalization constant, and the variable α represents the orbital exponent of the Gaussian function. All of these variables change as different methods are used and different molecules are examined.

While it is impossible to solve the Schrödinger equation for a many-electron system, various methods can be used to approximate certain values in the equation to make it solvable. The Hartree-Fock method is based on the use of three approximations to estimate the many-electron wavefunction: (1) The Born-Oppenheimer approximation, which assumes that all nuclei

are motionless with respect to the electron; (2) The Linear Combination of Atomic Orbitals (LCAO) approximation, which assumes that electron orbitals may be expressed as one-electron basis functions centered on each atom, and (3) the Hartree-Fock approximation, which assumes that the sum of all single-electron calculations of a molecule is the same as the multi-electron calculation of the molecule. Because of errors associated with the Hartree-Fock approximation, the entire Hartree-Fock computational method becomes less accurate with increasing molecular size.[2]

Density Function Theory (DFT) makes use of a different approach. Unlike the Hartree-Fock method, where the calculations start with an exact Hamiltonian and have approximate wavefunctions written in terms of a product of one-electron functions, the DFT method replaces the many-electron wavefunction with electronic density as the basic quantity.[3] Although not as well established and time-tested as the Hartree-Fock method, the DFT method is widely employed in the field of computational chemistry and is considered to be a good method to use with transition metal complexes.

The expected excited-state electronic transitions are determined by including the configuration interaction (CI) model in the *ab initio* quantum mechanical calculations. The CI model is derived from Hartree-Fock calculations that are expanded to incorporate electron promotion and changing shell levels.

4. MODELING IN NICKEL DITHIOLENE SYSTEMS

Following the general approach outlined in the previous section, a modeling methodology was developed to determine the electronic spectrum of nickel dithiolene complexes in the near-IR region. A series of nickel dithiolene systems that had previously been prepared and reported in the literature by Mueller-Westerhoff[4] was modeled and the calculated wavelengths were compared to the experimental literature data to test the accuracy of the modeling method. Because there is no single software package that can accomplish all of the steps required to calculate the electronic spectrum for the nickel dithiolene complexes, it became necessary to use several different software packages on two different computing platforms and develop methods to allow interchange of data and parameters between the various software packages. Table 1 gives an overview of the computational tasks that summarizes the details of the hardware and software used to perform the computations.

Computational task	Software	Hardware
Molecular mechanics optimization	Spartan 4.0[5]	2 GHz dual-processor Intel XEON server
Output-input file conversion	OpenBabel[6]	
Ab initio calculations	General Atomic and Molecular Electronic Structure System (GAMESS)[7]	SGI Altix Server (16-2.5 GHz Itanium 2 processors)
Electronic spectra generation	WebMO[8]	

Table 1: A summary of the computational tasks and resources utilized for the calculation of near-IR spectral transitions in nickel dithiolenes

Spartan was used to actually build the molecule and to run molecular mechanics optimization. The output file of optimized atom coordinates was then transferred to GAMESS

using OpenBabel. Specifying the appropriate conditions under which to conduct the *ab initio* calculations using GAMESS proved to be extremely challenging for a number of reasons. Parameter options and appropriate basis sets for the calculations must both be selected and specified properly in order to achieve accurate and useful results. This process is non-trivial under the best of circumstances, because there are a large number of calculation options and not all of these options are universally applicable to all calculation types or molecular systems. For relatively small organic molecules there is existing literature to guide in the selection of appropriate options and parameter sets, but in the case of nickel dithiolenes there is no pre-existing body of literature from which to draw guidance. Therefore, it became necessary to determine the proper calculation conditions based on: (1) extensive study of the general literature on *ab initio* molecular modeling theory, (2) review of the handful of existing references on *ab initio* modeling in unrelated transition metals and their complexes, and (3) testing of the selected modeling parameters and conditions by means of an iterative trial and error process.

The calculation options for GAMESS that were critical in obtaining an accurate model of the electronic distribution in the nickel dithiolene complexes are described below:

- *SCFTYP (self-consistent field wavefunction)*- specifies the basic calculation type that is used. For our work, the Restricted Hartree-Fock[9] (RHF) and Density Functional Theory[10] (DFT) options were used. The RHF method was ultimately chosen for the final calculations because (1) it was found to be more accurate than the DFT method in initial test trials, and (2) because the CI calculations that are required to calculate the absorbance spectra are based on the RHF calculations, they cannot be run concurrently with the DFT option.

10

- *GBASIS-* specifies the type of basis set used for the calculation and what type of basis set function to choose. The minimal basis sets (GBASIS=STO) and split-valence basis sets (GBASIS=N31) were chosen initially because they were two of the few basis sets that supported both nickel and the other atoms commonly contained in organic compounds (and consequently were the only ones capable of producing accurate calculations for the electronic structure of nickel dithiolenes). The minimal basis set used was STO-3G.[11-12] The 3G indicates the use of three Gaussian functions. Split-valence basis sets used were 6-31G with six Gaussian functions (indicated by the 6), and 6-31G(d),[13] which includes both six Gaussian functions and functions that incorporate *d*-orbital calculations. The split-valence basis sets proved to be more accurate because they correctly predicted that valence electrons do most of the bonding. The inclusion of *d*-orbitals increases the accuracy of the calculations.

- *SCF and DIRSCF*- specify whether the self-consistent field wavefunction will be calculated directly or indirectly.[14] Hartree-Fock calculations make use of a large number of two-electron repulsion integrals that are stored and retrieved from hard disk storage. The direct SCF calculation reevaluates the integrals directly without storing to disk during each Hartree-Fock iteration, which dramatically speeds up processing time.

- *CITYP* (Configuration Interaction Model Type) – includes and specifies CI models in the *ab initio* calculations for electronic spectra calculations. The CI method used for determining the electronic structure of a compound was configuration interaction single-promotion (CIS) because it gave accurate results within a reasonable time.[15]

- *NSTATE*- specifies how many different peaks in the electronic spectrum should be solved for during the calculations. The optimal value for NSTATE was found to be 10

because lower values generated inaccurate results while higher values significantly increased calculation times without any significant gain in accuracy.

- *DAMP* - aids in allowing the system to converge to an energy minimum state during SCF calculations[16-17]. *Ab initio* calculations were found to fail consistently in nickel dithiolene systems unless this crucial option is added.

The computational conditions listed above were used to verify the accuracy of the computational method and test its ability to predict near-IR electronic absorbance bands in novel, yet-to-be synthesized nickel dithiolene complexes.

5. COMPUTATIONAL RESULTS

Figure 2 below shows the calculated wavelength of near-IR absorbance bands using the new computational method together with the experimental wavelength reported in the literature by Mueller-Westerhoff[18] for a number of different solvents.

M = Ni
X = R1, R2, R3 or R4
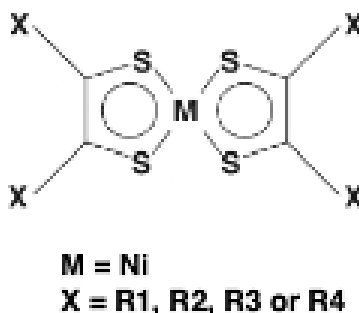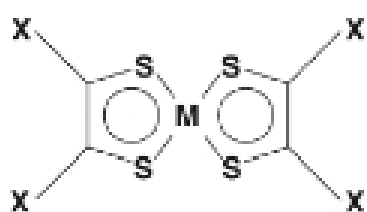
Terminal Group	Experimental Solvent	Experimental Wavelength (nm)	Calculated Wavelength (nm)
R=H	Hexane	720	720.91
R=CH$_3$	CHCl$_3$	774	843.08
R=CF$_3$	Pentane	715	775.05
R=S-C$_4$H$_9$	CHCl$_3$	1104	1012.31
R=C$_6$H$_5$	CHCl$_3$	866	845.19
R=2-Napthyl	CHCl$_3$	905	993.08
R$_1$,R$_4$=H; R$_2$,R$_3$=C$_6$H$_5$	CH$_2$Cl$_2$	805	857.78

Figure 2. The near-IR absorbance wavelengths for several nickel dithiolene compounds previously prepared and reported in the literature. The experimental wavelength is the actual wavelength of the near-IR absorbance band in the experimental solvent. The calculated wavelength represents the prediction of the new computational method.

The experimental wavelengths were measured using certain solvents. This may offset the calculated wavelengths. However, a Pearson correlation of the calculated near-IR absorbance data to the corresponding experimental near-IR data was determined for the compounds in Figure 2. The Pearson correlation *r* is a measure of the fit of a least-squares linear regression

through the data set. Likewise, the correlation coefficient R^2 describes the proportion of the points that can be accounted for by the linear regression. Calculation of a correlation coefficient R^2 between the experimental and calculated near-IR wavelength data yields a value of 0.91, which represents an excellent correlation between calculated and experimental results for a majority of the compounds modeled. The computational model currently assumes that the compound is in a vacuum. The excellent correlation is strong evidence of the predictive capability of the computational method developed in this work and validates its use in predicting electronic transition states in yet-to-be-explored nickel dithiolene systems. The following section describes the first steps in this direction.

The new computational method described in the previous sections was applied to a series of nickel dithiolene systems with ligands of varying structure in order to establish structure-property relationships that could be used in the design of new materials with an advantageous combination of physical and optical properties (high host solubility, large absorbance oscillator strength, and control of the peak absorbance maximum through ligand selection). The goal of this initial effort was to determine what structural features would allow the main near-IR absorbance band to be shifted to longer wavelengths without negatively impacting the solubility in a liquid crystal host material. Figure 3 below shows the predicted near-IR wavelength maxima for several nickel dithiolene compounds with varying terminal groups. The figure also includes for reference one nickel dithiolene complex with C_6 alkyl terminal groups that has been previously synthesized.

Terminal Groups	Experimental Wavelength (nm)	Predicted Wavelength (nm)
R=C_6H_5	866	845.19
R = S-H	?	1053
R = S-Ph	?	972
R_1, R_4 = S-H ; R_2, R_3 = S-Ph	?	1004
R_1, R_4 = H ; R_2, R_3 = S-Ph	?	1038
R_1, R_4 = H ; R_2, R_3 = S-H	?	1055

Figure 3: Predicted electronic spectral maxima for a series of candidate nickel dithiolene compounds that have yet to be synthesized. The first entry in the table is a compound that has been synthesized and included for reference.

One significant trend that can be observed on examination of the table is that the near-IR peak wavelength is red-shifted when sulfur-containing groups are bonded directly to the dithiolene core, whereas the near-IR maximum is blue-shifted in the case where phenyl groups are bonded directly to the dithiolene core. This observed trend is somewhat counter-intuitive, as it is normally accepted that the addition of aromatic groups in conjugation with another aromatic structure generally shifts the absorbance maximum of the molecule to *longer* wavelengths because of resonance stabilization (the energy gap between electron levels is reduced, thus allowing electronic state transitions to occur at lower energy and longer wavelengths). Clearly the *d*-orbitals on the sulfur-containing terminal groups are providing a greater degree of resonance stabilization than the phenyl groups. The nature of this stabilization is not yet understood, and will be investigated in the future.

One serious problem that was encountered with the model was the inability of GAMESS to produce accurate electronic spectral data for compounds containing nitrogen atoms. Failures in computation were routinely encountered in every attempt to model nitrogen-containing nickel dithiolene structures. In an attempt to determine the source of the problem, we modeled some very simple, classical nitrogen-containing organic compounds using the method and came up

with similar results. The source of the problem at this point is still unresolved, but it appears to be a basic functional issue with GAMESS itself and not with our specific computational methodology or parameter files. An investigation into this issue is ongoing.

5. CONCLUSION

A computational method has been developed that can accurately predict the electronic spectra of nickel dithiolenes. It now becomes possible to model new nickel dithiolenes prior to synthesis so that synthesis efforts can be concentrated only on those compounds that by theoretical predictions have the best chance of showing the desired physical and optical properties for device applications. A large number of trials can be run to see how different terminal groups will affect the electronic spectrum. One limitation of the current method is that the accuracy of the Hartree-Fock calculations is substantially reduced as the size of the molecule increases. DFT calculations may provide a workaround to this problem and should be investigated as an alternative. A more serious limitation is the current inability of GAMESS to accurately calculate electronic spectra when nitrogen atoms are included in the terminal groups. Future investigations will concentrate on improving the model to overcome these two limitations as well as further applying its predictive capability to new nickel dithiolene compounds in the low-to-medium molecular weight range.

ACKNOWLEDGEMENTS

REFERENCES:
1. K.B. Wiberg, *Physical Organic Chemistry*. New York: Wily & Sons, 1964.

2. W.J. Hehre, *A Guide to Molecular Mechanics and Quantum Chemical Calculations*. Irvine: Wavefunction, 2003.

3. W.J. Hehre, L. Radom, J.A. Pople, and P.v.R. Schleyer, *Ab Initio Molecular Orbital Theory*." New York, Wily and Sons, 1986.

4. U. T. Mueller-Westerhoff, B. Vance and D.I. Yoon, *Tetrahedron*, 47, 909, 1991.

5. M.W. Schmidt, K.K. Baldridge, J.A. Boatz, S.T. Elbert, M.S. Gordon, J.J. Jensen, S. Koseki, N. Matsunaga, K.A. Nguyen, S. Su, T.L. Windus, M. Dupuis, J.A. Montgomery, *J. Computational Chem*. 14, 1347-1363 (1993).

6. http://openbabel.sourceforge.net/

7. J. Kong, C.A. White, A.I. Krylov, C.D. Sherrill, R.D. Adamson, T.R. Furlani, M.S. Lee, A.M. Lee, S.R. Gwaltney, T.R. Adams, C. Ochsenfeld, A.T.B. Gilbert, G.S. Kedziora, V.A. Rassolov, D.R. Maurice, N. Nair, Y. Shao, N.A. Besley, P.E. Maslen, J.P. Dombroski, H. Daschel, W. Zhang, P.P. Korambath, J. Baker, E.F.C. Byrd, T. Van Voorhis, M. Oumi, S. Hirata, C.P. Hsu, N. Ishikawa, J. Florian, A. Warshel, B.G. Johnson, P.M.W. Gill, M. Head-Gordon, and J.A. Pople, *J. Computational Chem*. 21, 1532 (2000).

8. http://webmo.net/index.html

9. C.C.J. Roothaan, *Rev.Mod.Phys*. 23, 69-89, (1951).

10. P.M.W. Gill *Aust.J.Chem*. 54, 661-662(2001)

11. W.J. Hehre, R. Ditchfield, R.F. Stewart, J.A. Pople *J.Chem.Phys*. 52, 2769-2773 (1970).

12. M.S. Gordon, M.D. Bjorke, F.J. Marsh, M.S. Korth *J.Am.Chem.Soc*. 100, 2670-2678 (1978).

13. M.M. Francl, W.J. Pietro, W.J. Hehre, J.S. Binkley, M.S. Gordon, D.J. DeFrees, J.A. Pople, *J.Chem.Phys.* 77, 3654-3665(1982).

14. M. Haser, R. Ahlrichs, *J.Comput.Chem*. 10, 104-111 (1989).

15. R.M. Shroll, W.D. Edwards, *Int.J.Quantum Chem*. 63, 1037-1049 (1997).

16. E.R. Davidson *J.Comput.Phys*. 17,87 (1975).

17. M.L. Leininger, C.D. Sherrill, W.D. Allen, H.F. Schaefer, *J.Comput.Chem.* 22, 1574-1589 (2001).

18. U. T. Mueller-Westerhoff, B. Vance and D.I. Yoon, *Tetrahedron*, 47, 909, 1991.

Brandon Corbett
University of Rochester Laboratory for Laser Energetics
Advisors:
Dr. P. B. Radha
Dr. T. J. B. Collins
2/28/06

Maximization of Inertial Confinement Fusion Yields through Laser Pulse

Optimization

Abstract

A method has been developed for the optimization of high-gain inertial

confinement fusion targets. Using this method, software simulations have yielded pulse

shapes that produce high fusion gain and demonstrate good target stability using a 1

megaJoule (MJ) laser source. These pulse shapes could help attain ignition on the

National Ignition Facility inertial confinement fusion system.

Introduction

For many years Inertial Confinement Fusion (ICF) has been of interest as a

source of clean energy. ICF is a technology that uses high-powered laser pulses to

implode a small target containing deuterium and tritium fuel, compressing it to high

enough densities and temperatures to initiate a self-sustaining thermonuclear burn wave

resulting in ignition. The goal of this technology is power production. ICF is, in

principle, capable of greater efficiencies than nuclear fission and uses fuels that are

plentiful without the dangerous by-products of fission. Experimental and theoretical

results at the University of Rochester's Laboratory for Laser Energetics and elsewhere

have demonstrated that ICF may be feasible in practice as well.

The National Ignition Facility (NIF), currently under construction at Lawrence Livermore National Laboratory in California, is a project of particular importance for ICF development. It will be capable of energies believed to be sufficient to achieve ignition, where the energy produced is greater than the laser energy incident on the target. The NIF will be able to provide increased energy on targets three times as large as the targets in use today. In order for this project to succeed, however, targets must be designed and manufactured that are stable and produce high gain. We describe here promising new targets designed for the NIF. Key measures of a target design are its gain—the ratio of energy produced to the incident laser energy—and stability during the implosion (described below). A program has been written that systematically varies pulse shapes in order to improve the ease and efficiency of designing these targets. The targets analyzed using this program have demonstrated high gain and good stability, indicating a very high likelihood of ignition on the NIF using these designs. We will describe here an ICF target designed and optimized for the NIF using this program.

Targets and Pulse Shape Design

An ICF target design consists of both the target pellet structure and the laser pulse used to implode it. The target pellet is a spherical structure about 3 millimeters in diameter, composed of a number of layers of materials, the most important of which is the deuterium-tritium (DT) fusion fuel. The simplest target consists of an outer DT ice shell containing DT vapor, with a thin outer polymer shell used in the fabrication process. It has been shown that the absorption efficiency of targets can be enhanced by

replacing the outer portion of the DT ice layer with a layer of *wetted foam* – a polymer

foam saturated with DT ice.[1] The foam layer is located just inside the spherical plastic

shell; its bubbles are filled with the DT ice. In our designs, the thickness of each layer

was determined by scaling another target design,[2] intended for a 1.5 MJ ignition pulse,

to 1 MJ - the planned initial energy of the NIF. The resulting target has an inner shell

radius of 1300 microns, a 280-micron DT ice layer, a 90-micron wetted foam layer and

a 3-micron plastic layer. This structure is the same for all the designs discussed here.

An ICF implosion has three stages - acceleration, coasting and deceleration.

When the laser pulse begins, the target is imploded by laser ablation of material from its

outer surface. The laser illumination rapidly heats the pellet. This causes the material

at the surface of the target to ablate outward, forcing the shell inward. When this

process is taking place the implosion is in the acceleration phase. An acceleration phase

for a typical target lasts around 10 nanoseconds (ns). After the laser pulse terminates,

the shell material "coasts" toward the center with the inertia imparted by the

acceleration phase. Finally, deceleration occurs when the pressure of the vapor inside

the shell is sufficient to decelerate the imploding shell material. A critical part of the

design process is determination of the laser pulse power as a function of time to

optimize this sequence. This laser pulse power function can be varied to produce

different implosion characteristics.

A typical ICF laser pulse sequence is shown in Figure 1. This pulse sequence

consists of a picket pulse (the small-amplitude pulse at 0 – 1 ns), a foot-pulse (the pulse

roughly between 1 ns and 4 ns), and a drive-pulse (the large-amplitude pulse at 4 – 8

ns.) More complex pulse sequences may have additional "picket" pulses and relaxation

periods (the time between the picket and the main pulse).
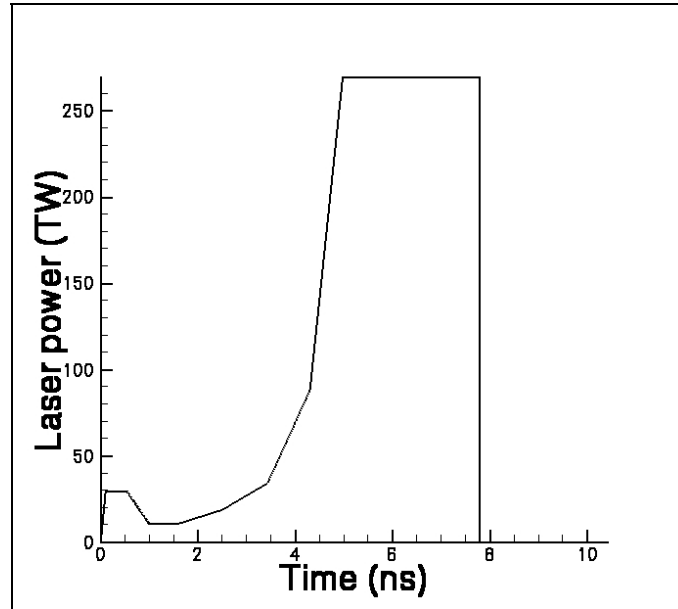
Figure 1: A sample laser pulse shape.

A shock wave propagates into the shell whenever the laser power increases

rapidly. A shock is a wave of abrupt compression that propagates through a target.

Shocks are significant because as they pass through a target they concentrate energy,

increasing the temperature of the target. As the DT fuel becomes hotter it becomes

harder to compress. The lower the density of the fuel remaining after the laser has

turned off, the lower the fusion rate, and the lower the energy released by the implosion.

In order to minimize the loss in gain that is caused by a series of shocks, pulse shapes

must be designed to time shocks to heat specific parts of a target. This timing is

accomplished by varying aspects of pulse shapes such as foot-pulse length or drive-

pulse height. For this pulse shape, shocks are launched at the start of the pulse, and

during the rise in power from the foot-pulse to the drive-pulse.

Instability

Imploding targets are subject to a phenomenon called the Rayleigh-Taylor instability. This instability occurs when a light fluid accelerates a heavier one. A simple example of this phenomenon is an inverted glass of water, as shown in Figure 2. When a glass of water is inverted, the pressure in the atmosphere is sufficient to hold the water at the top of the glass. However, any small perturbations in the water's surface result in pressure perturbations. These perturbations grow exponentially in time, causing bubbles of air to rise into the water and "fingers" of water to fall into the air at the bottom of the glass, eventually resulting in the air and water changing places.
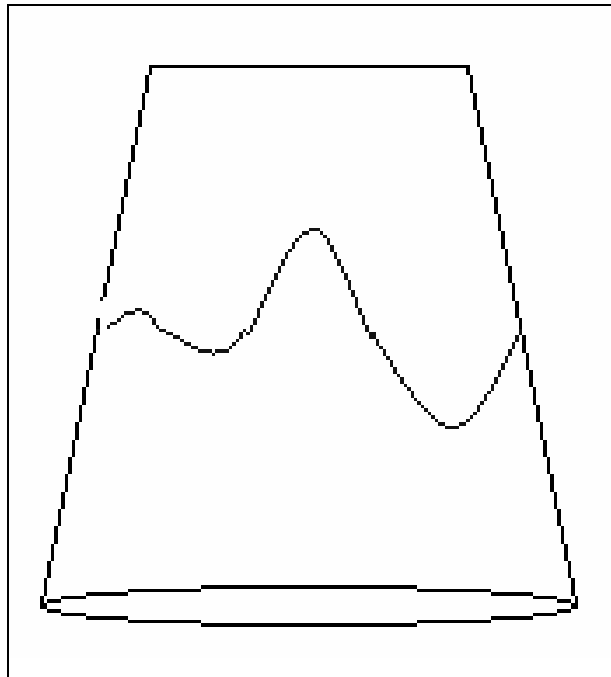
Figure 2: Rayleigh-Taylor instability demonstrated in an inverted glass of water

The Rayleigh-Taylor instability occurs in two places during the implosion of a

target - first within the ablated material at the outer surface of the shell during the acceleration phase, and later between the DT vapor and the interior of the shell during the deceleration phase. Although other instabilities exist, the Rayleigh-Taylor instability is the most significant because its growth is exponential. When the bubbles and fingers caused by the Rayleigh-Taylor instability grow too large, holes are punched through the shell of the target, preventing it from achieving ignition.

To predict the effect of the Rayleigh-Taylor instability during the acceleration phase, the ratio Q of the root-mean-square (RMS) bubble amplitude to the shell thickness ratio at the end of the acceleration phase is calculated. To gauge the degree of instability during the deceleration phase, the peak implosion velocity of the shell is calculated. This can be related to the degree of growth the inner-surface perturbations will experience. The growth rate of the Rayleigh-Taylor instability of each mode number was used to calculate of the bubble amplitude using the Betti formula, [3]and taking into account non-linear effects through Haan saturation.[4]

One of the factors that affects the stability of the shell during the acceleration phase is the amount by which the shell has been preheated and the area in which it has been preheated. This preheating can be changed by shocks that travel through the shell. Preheating on the exterior of the shell allows for material to ablate more easily, effectively reducing instability; preheating on the interior of the shell makes the target harder to compress, reducing the effectiveness of the target. In order to create this gradient of preheating from the inside to the outside of the shell a power spike or "picket" is added as seen in Figure 1. Another factor that affects stability is ablation

velocity. As the ablation velocity increases a target becomes more stable. This is the case because the fingers that form on the target receive more heat flux than the bubbles. Because of this they ablate faster and are thus minimized. Another important thing to note is the presence of Haan saturation. Haan saturation essentially levels off the exponential growth that occurs when a target is imploded.

There are trade offs between the amount of stability at different points within a given target and the gain that a given target will produce. For example, as the stability on the inside of the target during the deceleration phase increases there may be a loss of stability on the exterior of the target. This occurs because to increase stability on the inside of the shell the implosion velocity must be high. To attain a high implosion velocity the shell must be accelerated faster meaning more force must be exerted on the shell and thus the outer surface has a lower stability. Other such tradeoffs also exist between stability on either surface and gain. This is indicated by the fact that perfect shock timing indicated by high gain is usually not the best solution for good stability.

<u>Optimization and results</u>

A program has been written that allows the user to vary the parameters of the pulse shape over specified ranges. For each point in the variation a 1-D simulation of the implosion is performed and the gain and stability properties calculated. The program is capable of varying either one variable at a time, or two simultaneously. (To improve simulation efficiency, 1-D simulations may be performed simultaneously up to a system limit the of number of concurrent jobs.) First, based on laser system

restrictions, the program creates a pulse using the Kidder model.[5] The Kidder model is based on the concept of a pulse shape that sends an infinite number of infinitely small shocks through the target. Once a pulse shape is created, certain parameters of it are varied based on user inputs such as foot-pulse length and drive-pulse height. The results of the simulations are written to a final output file in a format that can be plotted graphically. Ratios of the RMS bubble amplitude to shell thickness of less than 20% (or 0.2) were sought to maintain sufficient acceleration-phase stability. In order to maintain sufficient deceleration-phase stability, we generated designs for which the implosion velocity must be comparable to or greater than 430 microns per nanosecond (μm/ns).

Three basic designs have been tuned to produce the highest gain possible with acceptable stability. First, a simple Kidder pulse constrained by NIF laser system requirements was tuned. This pulse shape demonstrated a highest gain of 80, but the variation that produced the highest gain had a low implosion velocity, indicating greater susceptibility to deceleration-phase growth and therefore the likelihood of failure. However, slight variations in drive-pulse height brought implosion velocities up to the marginal speed of 410 μm/ns. For this design the bubble amplitude to shell thickness ratio was 0.4.

A final scan of both drive-pulse power and foot-pulse duration is shown in Fig. 3. In this plot the grayscale contours show the gain, while the contour lines give the values of Q. The same plot, but with the contour lines marking the implosion velocity, is shown in Fig. 4. Note from these two figures that while the peak gain corresponds to a foot-pulse length of 2.4 ns and a drive-pulse height of about 185 TW, the highest gain

which can be achieved while maintaining the desired implosion velocity and bubble amplitude is in the neighborhood of 2.4 ns and 200 TW. It is interesting to note the way in which gain, bubble amplitude, and implosion velocity vary with drive-pulse height and foot-pulse length. As seen in Fig. 3, there is a large drop off of gain for each drive-pulse height as the foot-pulse length is increased. This is because as foot-pulse length increases past a certain point the shocks become poorly timed. It is also interesting to note that the contours of minimum implosion velocity on Fig. 4 run roughly parallel to the horizontal axis. This indicates that as the drive-pulse power increases the implosion velocity increases and is relatively independent of foot-pulse length.
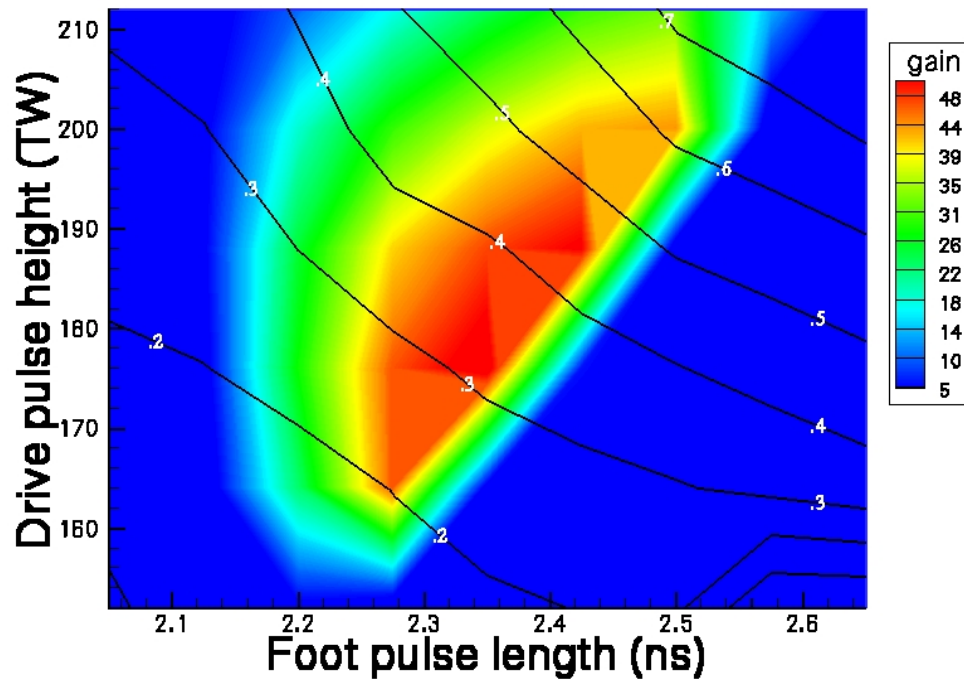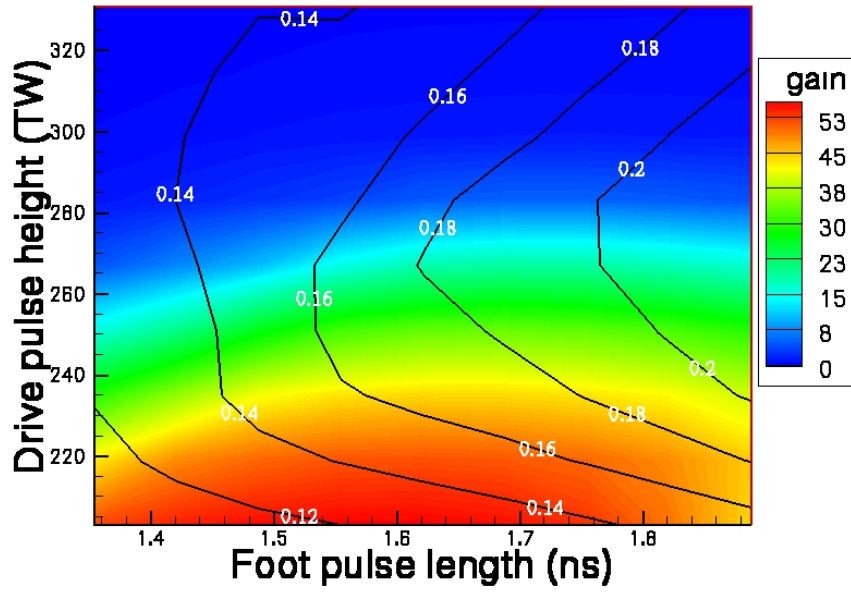

Figure 3: Plot of simulations of a picket-less design showing gain in color contours and bubble amplitude ratio Q in line contours as they vary with changes in foot-pulse length and drive-pulse power. Each simulation has the same input laser energy (1 MJ).
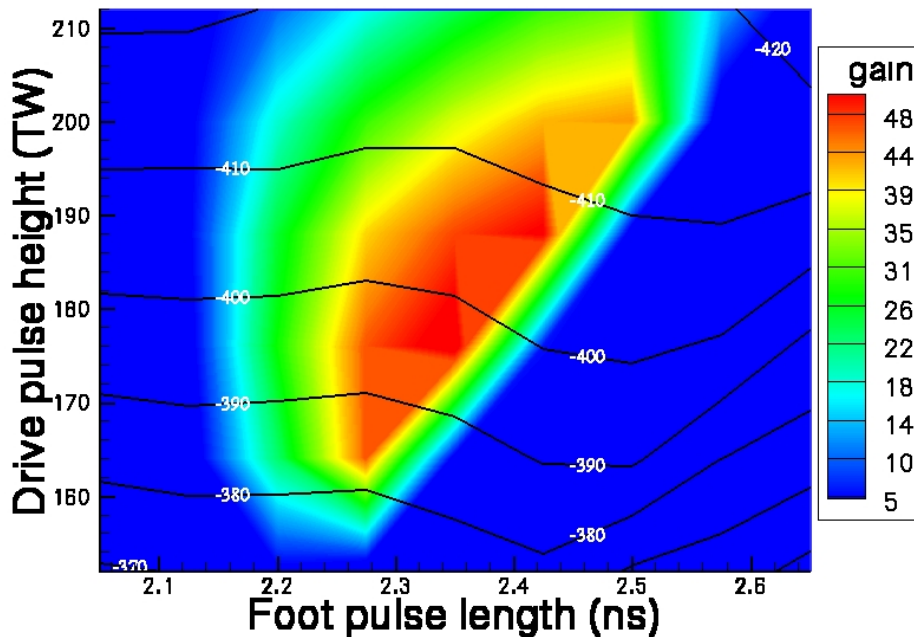
Figure 4: Plot of simulations of a picket-less design showing gain in color contours and implosion velocity (μm/ns) in line contours as they vary with changes in foot-pulse length and drive-pulse power

Second, a pulse was tuned which included a picket at the start of the pulse. A series of variations were made, varying the foot-pulse length, drive-pulse power, and picket height. These yielded a number of promising targets. Maximum gains peaked around 60 but had implosion velocities of around 400 μm/ns. Values of Q for these designs were all below 0.40. One pulse shape in particular produced a gain of near 50 with an implosion velocity of around 440 μm/ns and bubble amplitude ratio of 0.15. Since this is a promising result, future investigations may focus on further optimizing this target.

Third, a pulse was tuned which was preceded by a picket, followed by a period

of relaxation during which the laser power was zero. An initial pulse shape was provided[6] that combined a Kidder pulse with an extremely short picket, a relaxation period, and a foot-pulse. This pulse shape successfully ignited fusion in a wetted-foam target design. With variations of picket power and relaxation time, a pulse shape was arrived at that produced a gain of 80 with a reasonable bubble amplitude to shell thickness ratio. However, the implosion velocity was too low. In order to increase the velocity, the drive-pulse power was varied over a large range using the pulse shape with the maximum gain as a starting point. From this variation a pulse shape was chosen with an implosion velocity of 406 μm/ns. Variation of relaxation time and drive-pulse height of these pulse shapes produced high gain with good implosion velocity, but the ratio of bubble amplitude to shell thickness was extremely high (approaching 1).

Next, a pulse from the initial variation set was chosen with a gain of 60 but with better stability. Using this pulse drive, the pulse power and foot-pulse length were varied. In this variation a maximum gain of 64 was found but the stability was moderate. After three more variations the grid of targets shown in Figures 5 and 6 was created. Within this grid, at a foot-pulse length of around 1.5 ns and a drive-pulse height of around 220 TW, there are pulse shapes that produce gains in the 50's, implosion velocities around 440 μm/ns and bubble amplitude to shell thickness ratios of around 0.14. With slight modifications, this pulse shape could prove very stable and productive for use on the NIF.

Figure 5: Plot of simulations of a picket design showing gain in color contours and bubble amplitude ratio Q in line contours as they vary with changes in foot-pulse length and drive-pulse power.
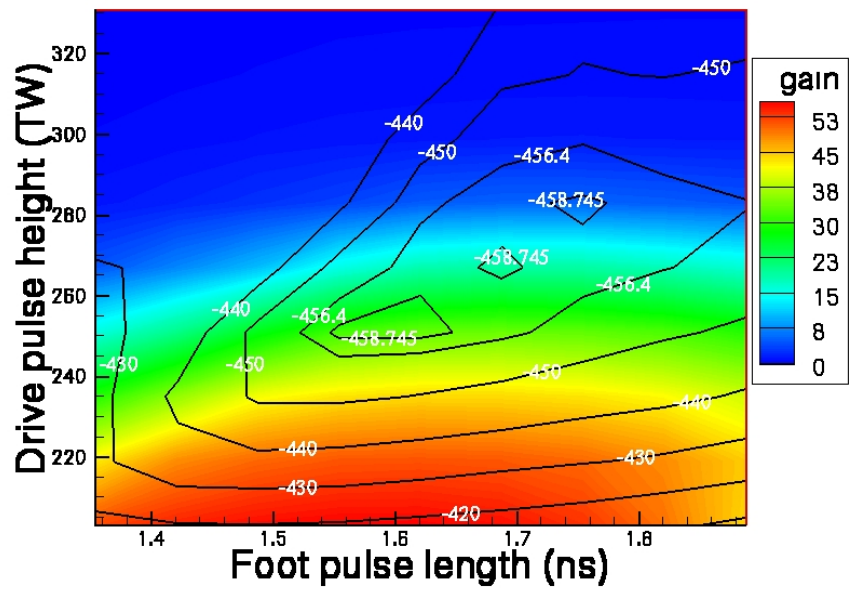

Figure 6: Plot of simulations of a picket design showing gain in color contours and implosion velocity (μm/ns) in line contours as they vary with changes in foot-pulse length and drive-pulse power.

Conclusions

Targets and laser pulse shapes have been designed that show very good likelihood of ignition on the National Ignition Facility (NIF). These designs demonstrate possible starting points from which highly efficient, finely tuned pulse shapes can be designed. These improved pulse profiles may provide the basis for demonstrating high-yield fusion on the NIF, proving the concept of Inertial Confinement Fusion. This would be a first step towards proving the viability of Inertial Confinement Fusion as an energy resource.

References

[1] Sacks, R. A. and Darling, D. H., *Nuclear Fusion*, **27**, 447 (1987)
[2] P. W. McKenty et al., *Physics of Plasmas*, **8**, 2315 (2001)
[3] Betti, R., et al., *Physics of Plasmas*, **5**, 1446 (1998)
[4] Haan, S. W., *Physical Review*, **A39**, 5812 (1989)
[5] Kidder, R. E., Nuclear Fusion, **14**, 797 (1974)
[6] Anderson, K., private communication (2005)

Acknowledgements

Optical Time Domain Reflectometry for the OMEGA EP Laser

Adam DeJager

Greece Odyssey Academy

Advisors: Samuel Morse and Richard Kidder

Laboratory for Laser Energetics

University of Rochester

Summer High School Research Program

2005

Abstract

Optical Time-Domain Reflectometry (OTDR) refers to the return of light back through the laser after it is fired. The OTDR device at the laser source is used to track the return signals of that light. When a shot is fired, the laser beam passes through several optical components on its way to the target chamber. When passing through each optic, a small amount of the laser is reflected backwards through the laser. Anti-reflective coatings help reduce the reflection, but if they malfunction, a significant percentage of the laser's power can be lost. When the reflected signals arrive back at the laser source, they are recorded by the OTDR. A computer program has been written to handle the OTDR data on the new OMEGA Extended Performance laser. The program finds all the return signals and if there is an unexpected spike, it will identify which optic it came from. The program produces a user-friendly display of all reflected signals to allow easy interpretation and corrective action.

Introduction

The Research Project - Purpose and Rationale

The research topic involving computed optic failure identification using Optical Time-Domain Reflectometry (OTDR) was chosen because there was no existing method on the current or new laser to easily identify which of many optics had failed and needed to be replaced in order to maintain peak system transmission of light to the target. Knowing which optic has failed will minimize system down time needed to identify and replace failed optics and to maximize energy on target for each experiment using the laser(s).   When system down time is minimized, the number of shots per unit time increases. This allows more experiments to be conducted. When energy to the target is insufficient, certain experiments cannot be conducted at all or will need to be repeated. In general, progress in support of the laboratory's mission is diminished if on-target energy is insufficient or if a reduction in the number of shots is encountered. The ability to quickly and correctly identify the specific optic that has failed is important to the success of the laboratory. The research project deliverable meets this need for the new laser and closes a gap in the capabilities of the existing laser.

The research project consists of two major components: Optics and Software.

OMEGA Extended Performance (EP)

The OMEGA EP laser will provide the Laser Laboratory with a new resource to explore research into laser-driven fusion in order to obtain a cheap and renewable source of energy. This new laser is built tangent to the existing OMEGA laser; the two lasers

will work together to perform experiments neither could do alone. The new experiments possible with the OMEGA EP laser will advance science towards the ultimate goal of achieving fusion, most directly through experimental support of the National Ignition Facility under construction.

The OMEGA EP laser uses a new multi-pass architecture, which means that the light from a single laser shot is reflected so that it passes through the same optical components, in particular the amplifiers, multiple times. This is much more efficient than passing through different, identical optics, and results in a very powerful laser by the time it hits the target.

Figure 1.0 below shows the path of the laser beam from the source to the target.

Figure 1.0 Omega EP laser light path

RP0 = Laser Source	**POL = Polarizer**	**CEM = Cavity End Mirror**
TSF = Transport Spatial Filter	**PEPC = Pockel Cell**	
BAMP = Booster Amplifier	**SPPOLS = More Polarizer**	
FM = Fold Mirror	**CSF = Cavity Spatial Filter**	
MAMP = Main Amplifier	**DM = Deformable Mirror**	

Optical Time Domain Reflectometry

When the laser beam passes through the optical components of the OMEGA EP laser, small amounts of light are reflected back through the laser towards the laser source. While the percentage of the beam normally lost per optic is small, by time the laser beam hits the target, the beam could have passed through enough optics that there could be insufficient energy left in the beam. If an optic is damaged or has failed, the on-target energy could be severely diminished.

Anti-reflection coatings can reduce the amount of reflected light to an acceptable amount of 0.05% per optic. However, during a shot, an immense amount of energy is fired through the laser, meaning that over time, some coatings may become damaged. When this happens, the light reflected by the damaged optic is greatly increased, resulting in the needless loss of energy. This situation could impact the success of the experiment and the ability of the Laser Lab to ultimately achieve its mission.

To keep track of the reflections back to the laser source, a detector and oscilloscope are installed at the point of laser beam initiation. The oscilloscope produces a signal of the light coming back through the laser (amplitude vs. time) that can be read to determine if all reflective coatings and optics are working properly. If an optic is malfunctioning, there will be a large unwanted spike in the graph, representing the increase in reflected light.

By noting the time that the spike occurred, a computer program can determine which optics are causing the high return signals and display them to the user. Once identified, the damaged optic can be replaced or repaired so that the beam no longer loses

a critical amount of energy. Figure 2.0 below shows an example of how reflected light

from a lens occurs.

Small regions of the center of each lens reflect light backwards into the small apertures of system pinholes

• On the Cavity lens there are 4 separate 1.25 mm diameter areas that directly reflect 0.5% of the forward going laser to the 4 pinholes

• Forward going power of 1 Gigawatt/cm^2 creates pencil beams at 5 Megawatts/cm^2 power stray light

• The stray light may see additional amplification as it returns towards the OTDR detector
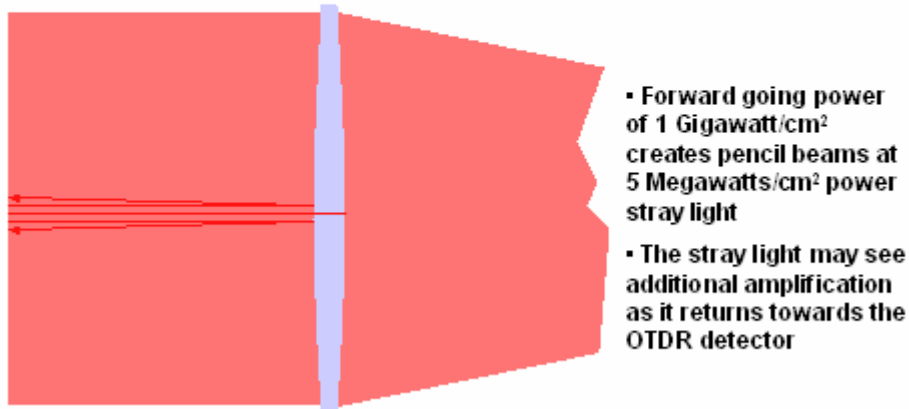
Figure 2.0 Lens Based Reflected Light Opportunities

Method

Data Tables

Data containing the future spatial placement of the optical components of the

EP laser were available at the beginning of the project. They were used to fill the

database that the computer would use when calculating the sources of the return signals

in the laser.

MATLAB

The program used for the creation of the Graphical User Interface and

calculation of sources was written using MATLAB M-files and GUI editors. All code

was written in the MATLAB language.

Optical Analysis

Optical Time Domain for Equal Path Scenarios

When the laser is fired, every optical component that is passed through along the way to the target has the potential to generate a return signal that would make it back to the laser source. Lenses have the greatest probability to create such signals. The most common way that light is reflected backwards through the laser is called an equal-path scenario. This means that the light will hit the optic, and its reflected inbound path to the detector (the path taken to get back to the laser source) will retrace its outbound path from the source (the path originally taken to reach the optic).

In order to predict when such possibilities may reach the oscilloscope, the time delay for the light to reach any given optic must be doubled; the resulting value accounts for the time taken to travel the inbound and outbound paths (which are equal) and thus accounts for the total path. This calculation was performed for each optic so as to create the time-based values for the return signal for every equal-path scenario.

OTD for Unequal Path Scenarios

While most cases for the return of laser light are equal path scenarios, there are specific cases where the paths of the outbound beam and the inbound beam are unequal. This occurs because of the multi-pass architecture of the EP beam path. Since the multi-pass system causes the laser beam to pass through the same optics multiple times, returning laser light could end up 'bouncing' around in the laser cavity. This creates scenarios where the inbound path is greater than the outbound path. Also, there are scenarios where the returning light's inbound path is less than the outbound path. For

example, if the laser was on pass 3, passing towards the Deformable Mirror for the second time, but was reflected, it could follow a short path directly back to the laser source.

This bouncing creates possibilities for the laser beam to arrive at the laser source at unusual times. For example, if the laser bounces around the cavity and finally arrives back at the laser source at 1000 ns after the shot, but there is no optic at 500 ns delay, this then represents situation of unequal inbound and outbound path lengths. Figure 3.0 shows an example of an unequal path scenario.
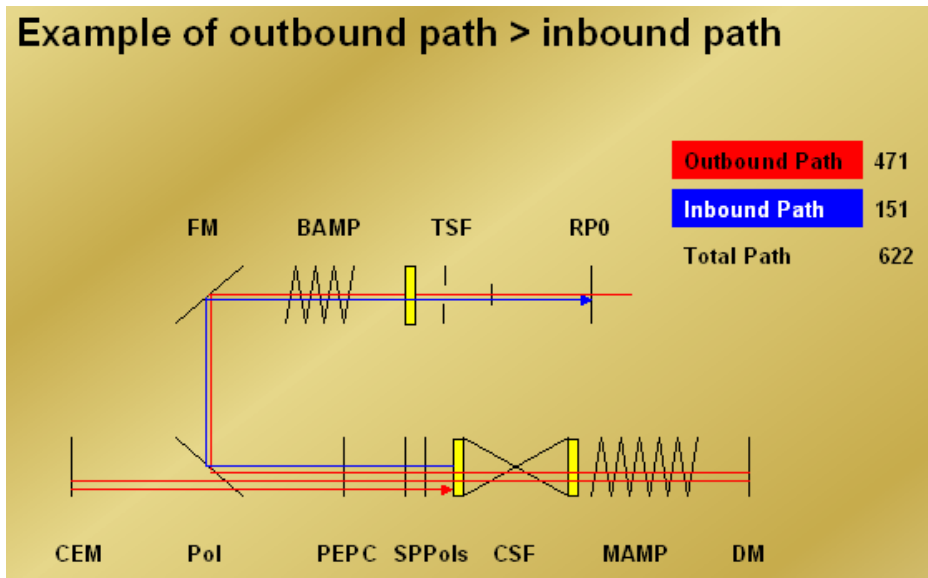
Figure 3.0 Unequal Path Scenario

The number of lenses that the laser beam passes through limits the number of unequal path possibilities. Because there are a total of ten passes through lenses, there are only ten cases where an unequal path scenario could occur. For each of these ten, the path the bouncing light would follow was traced, and the total time delay of the new path was then calculated. The results of these calculations were then added to the program's

database, so that when unequal path scenarios occur, they do not confuse the program. Instead, it recognizes the arrival times of those ten cases as what they are. For example, if case 7 results in the laser beam returning at 1250 ns, and case 7 occurs, the program recognizes the 1250 ns to mean that case 7 has occurred.

Some of the unequal paths overlap in expected return times. This is because the inbound path of one scenario is often equal to the outbound path of another and vice versa, resulting in two possibilities. If this happens, the program will list both possibilities for investigation.

Finally, the reflections measured at the detector will only be those of primary reflections of equal and unequal path lengths. In other words, any signal from secondary or more reflections will simply be too small to measure and in any event, would be below the threshold of interest.

The finished database contains the data for all equal path scenarios, along with all ten unequal cases. Thus, the program has knowledge of every predictable scenario in which laser light may find its way back to the laser source. Using the data from the oscilloscope after a shot, the program will use the database to calculate where the return signals came from by comparing the time delay of the return signals to the list of return signal possibilities in the database.   In the unlikely event that an unforeseen reflected return time is obtained, the program will list the return time and indicate a need for further investigation.

Software Development

Iterative Process

The approach to developing the software was a highly planned and iterative method. Before any code was written, the requirements were analyzed to determine what exactly the end program needed to do. Then, elements of the program were planned to specifically meet those requirements. After those elements were designed, they were compared to the original requirements to see whether the requirements were indeed being met. Only then was code written. After the code was complete, and at several steps along the way, it was again checked against the original requirements to make sure the program was going to do what it needed to do. This iterative process is known as the RUP, (Rational Unified Process) method of programming. It resulted in the end-product-program doing exactly what it was meant to do. Figure 4.0 shows a flow diagram of the Rational Unified Process.
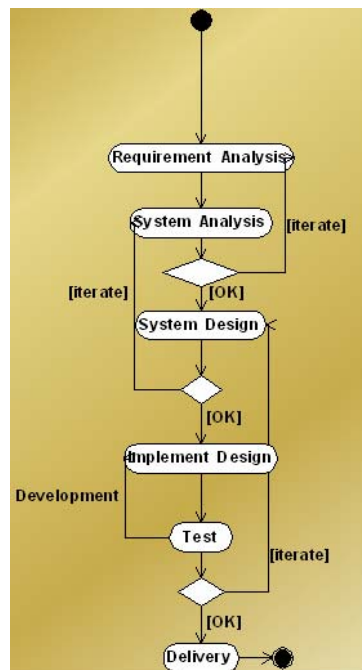
Figure 4.0 Rational Unified Process

Creation of OTD Databases

Data was inserted by rows into a database where information on each optical component is stored. Information such as component ID, component label, and time delay were kept for each component. When the program accesses the database it gains knowledge of the entire laser beam system because it contains all vital information on all components of the laser.

Internal Working of the Program

After each shot from the laser, the OTDR program will be launched. It will establish a connection to the database containing time delay data. For each return signal, it compares the time of the return to the times in the database and looks for matches. The matches are where the program calculates the return light to come from.

Output

The end output of the program is a graphical user interface that displays a graph of amplitude vs. time of return signals for each beamline (total of four graphs) and a table summarizing the signal spikes and their likely origin. Also, the GUI has several buttons that allow for commands, like saving all of the data for the past shot in an .hdf file for future reference, or loading the data for those past shots to be viewed again.

The program allows for user customization of the display. Each optical component has a corresponding "tick mark" on the graphs. The tick marks can be toggled on or off by the user. The tick mark toggle changes the appearance of the graph in such a

way as to visually align the tick mark with the spikes to more readily discern which

components are the causes of the return signals. Figure 5.0 below shows the output of the

program that facilitates user understanding and interpretation of the results.
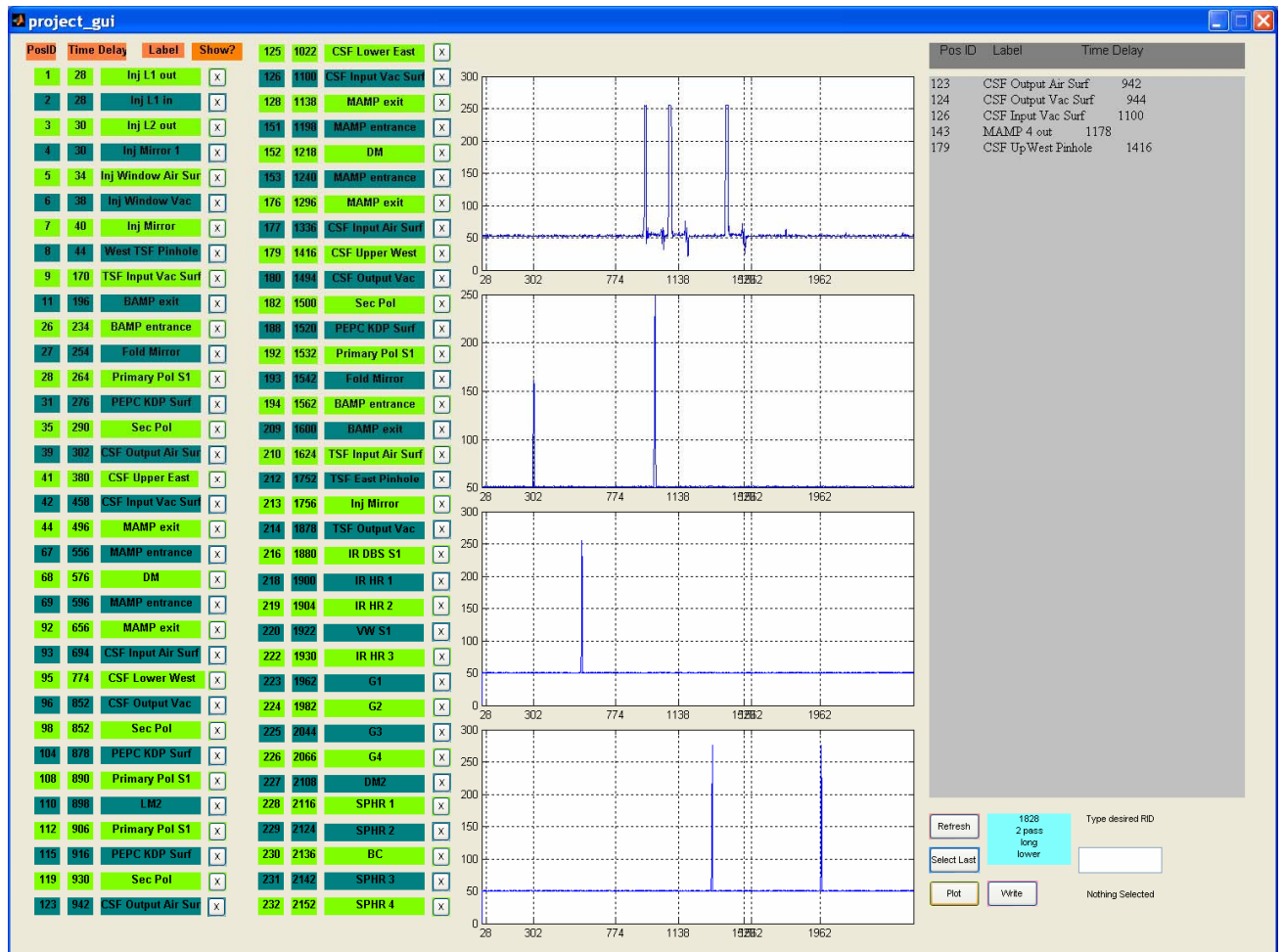
Figure 5.0: GUI Output with graphs and table of return signals.

Future Work

The next step for the OTDR project is to add features that allow the estimation of the magnitude of possible return signals. This will tell whether the return signals present a threat of damaging the laser.

Also, the same OTDR program built for the OMEGA EP laser will be implemented on the original OMEGA laser. Once the OMEGA laser components are entered into their own database, the program will do for OMEGA exactly what it is planned to do for OMEGA EP. Therefore, the program benefits both laser systems.

Conclusion

Reflected light from optical components in the OMEGA EP laser represents a significant barrier to the Laser Lab goal of supporting laser driven fusion research. It is minimized to an acceptable degree by anti-reflection coatings, but these coatings can wear out and fail over time. The OTDR program was created to be able to tell if an optical component is malfunctioning so that it can be isolated and replaced. By minimizing the reflections, light loss is minimized, meaning that the laser beam will hit the target at near full power, with no damage to the OMEGA EP laser.

Investigation of the effect of a plastic ring on the uniformity of ice layers in cryogenic inertial confinement fusion targets

Frank Fan

Webster Schroeder High School
Webster, NY

Advisor: Dr. R. S. Craxton
Senior Scientist

Laboratory for Laser Energetics
University of Rochester
Rochester, NY

Abstract:

A program has been written to model the evolution of the cryogenic ice layer during the layering of a target for inertial confinement fusion. The program simulates the thermal diffusion in the layering sphere, as well as the sublimation and deposition of the deuterium. This will facilitate the design and production of more-uniform targets. It has been found that any nonuniformities caused by the plastic rings of the recently proposed "Saturn" targets are too small to significantly impact fusion performance.

1. Introduction

Controlled nuclear fusion is a promising technology for producing clean, abundant energy. Laser-based inertial confinement fusion (ICF) is one method under investigation for producing the extreme temperatures and pressures required for fusion reactions to occur. In direct-drive ICF, an array of powerful laser beams fires upon a target from many directions, heating and compressing the target[1]. The target is a spherical plastic shell containing the hydrogen isotopes deuterium (D_2) and tritium (T_2). When the target is compressed, the deuterium and tritium nuclei fuse to form helium nuclei and energetic neutrons. (Another approach, indirect-drive ICF[2], involves laser beams entering the target chamber from the top and bottom and irradiating an x-ray-producing target. These x-rays then "indirectly" drive the spherical fuel-containing target.) Targets used in current laser-based ICF experiments generally contain only deuterium, as tritium is radioactive and hard to work with.

Cryogenic targets are spherical plastic shells with thin layers of solid deuterium and tritium on the inner surface of the shell. By using solid fuel, cryogenic targets can store much more fuel than traditional, gas-filled targets, increasing the likelihood of a

chain reaction. The plastic shells are first filled with gaseous deuterium and tritium, which are transformed to solid when the shells are cooled down. The target is then slowly heated in a device called a layering sphere to generate a more even ice layer, which improves the fusion performance.

Unfortunately, the heating inside the layering sphere is not perfectly uniform. For example, the so-called "Saturn" targets[3] for polar direct drive at the National Ignition Facility have small plastic rings around the equators, which can cause uneven heat conduction in the layering sphere. This can introduce nonuniformities in the ice layer, reducing the fusion performance. As the "Saturn" target has only been proposed very recently, it is not clear how severe the ice nonuniformity would be and whether it would have a significant impact on fusion performance. A program has been written to model the evolution of the cryogenic ice layer during the layering process, including simulation of the thermal diffusion in the layering sphere as well as the sublimation and deposition of the deuterium. The program was initially intended to answer the "Saturn" ring target question, but it is also flexible enough to model other target designs. It is believed to be the first program of its type.

1.1 Cryogenic targets

Cryogenic targets currently being used on the OMEGA laser system[4] are about 900 μm in diameter and contain solid deuterium. A cryogenic target typically has a 3 μm-thick plastic shell, with a 100 μm-thick deuterium ice shell on the inner surface of the plastic shell. The center contains deuterium vapor (see figure 1).

1.2. Cryogenic target formation

The formation of the cryogenic target involves several steps. First, a spherical
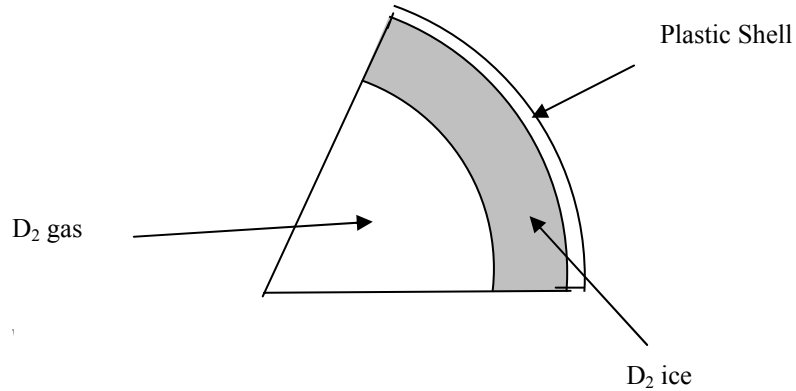
Figure 1: Cryogenic target cross section

plastic shell is filled, through diffusion, with deuterium gas to a pressure of about 1000

atm. The target is then cooled below the triple point of D_2, first entering the liquid phase,

then freezing into a layer of solid D_2. The D_2 layer is not uniform, as gravity pulls the D_2

to the bottom of the shell when it is in the liquid phase. Then, the target is

placed in a layering sphere (figure 2), a spherical cavity with reflective, gold-coated

walls[5]. An optical fiber is used to introduce low-power infrared light into the layering

sphere. The light reflects off the walls and is absorbed by the D_2 ice. The rough surface of

the wall ensures that the infrared light is scattered in all directions. In addition, the

infrared light may bounce back and forth several times before it hits the target.

Consequently, the target is heated uniformly in all directions. The thicker areas of the ice

absorb more light and become hotter than the thinner areas. The ice in the thicker areas

sublimes faster than the ice in the thinner, cooler areas, and the resulting gas
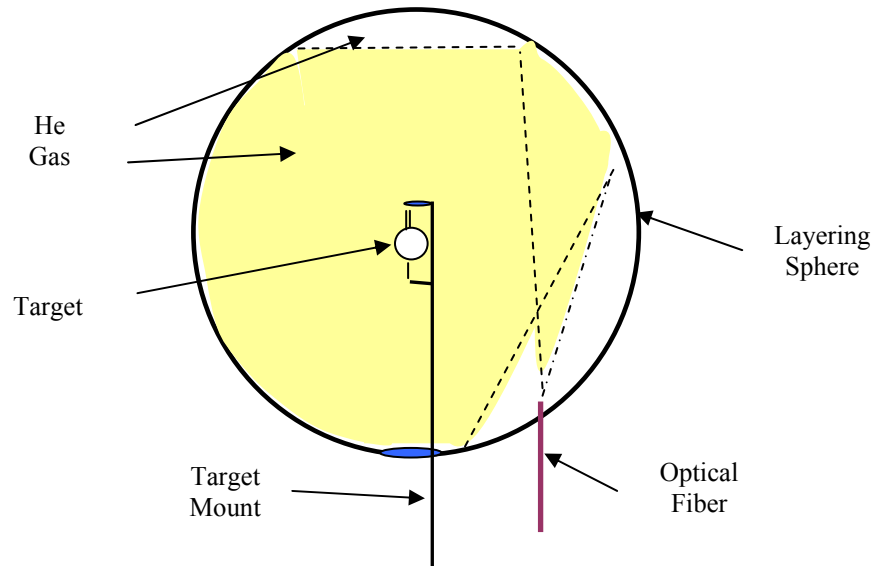
Figure 2: Layering sphere. The target is supported by a target mount. The optical fiber introduces the infrared light (yellow area), which is scattered from the wall and heats the target uniformly. The helium gas in the layering sphere conducts the heat from the target to the wall.

preferentially condenses on the cooler, thinner areas (figure 3). The heat is removed from the target by conduction through the helium gas to the wall of the layering sphere, which is kept at a constant temperature of 18.6 K. The layering process takes about 24 hours,

(a)   (b)
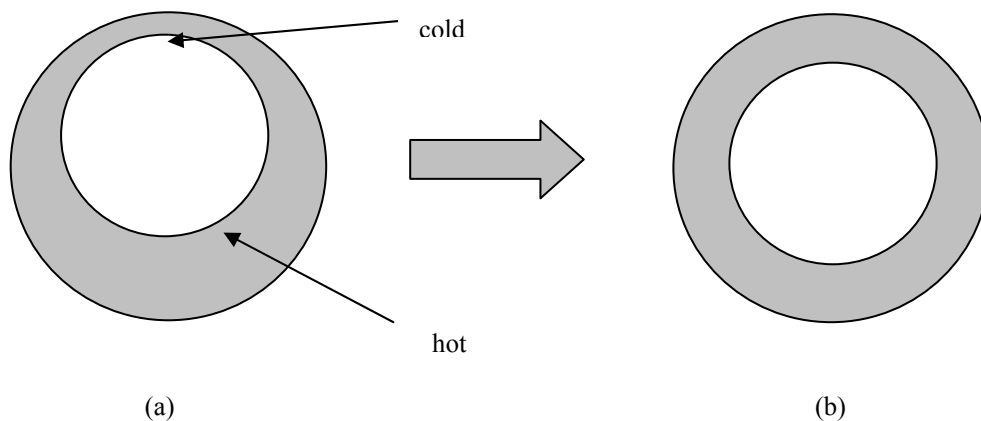
Figure 3: A cryogenic target (a) before and (b) after the layering process. The thicker portions become hotter due to heating by infrared light, so deuterium sublimes from the thick portions and deposits on the thin portions, resulting in a more even ice layer.

and results in an isotherm along the inner surface of the ice layer. An even ice layer is required because an uneven ice layer results in uneven compression and poor fusion performance. A nonuniformity of 1% can be tolerated in the ice layer. In a 100 μm ice layer, this translates to a nonuniformity of 1 μm.

1.3 Saturn Targets

The National Ignition Facility (NIF) is a facility for laser-based ICF research scheduled for completion in 2010. The new, 192-beam laser is designed to deposit 1.8 MJ of energy on a target 3 mm in diameter. The greater amount of fuel in the larger targets increases the probability of an energy gain, in which the fusion energy generated is greater than the input laser energy. However, the NIF is designed to perform indirect-drive laser-based ICF experiments and has no laser beams aimed at the equator of the target. To perform direct-drive experiments, a novel target design has been proposed.

(a) Top view.

(b) Side view.
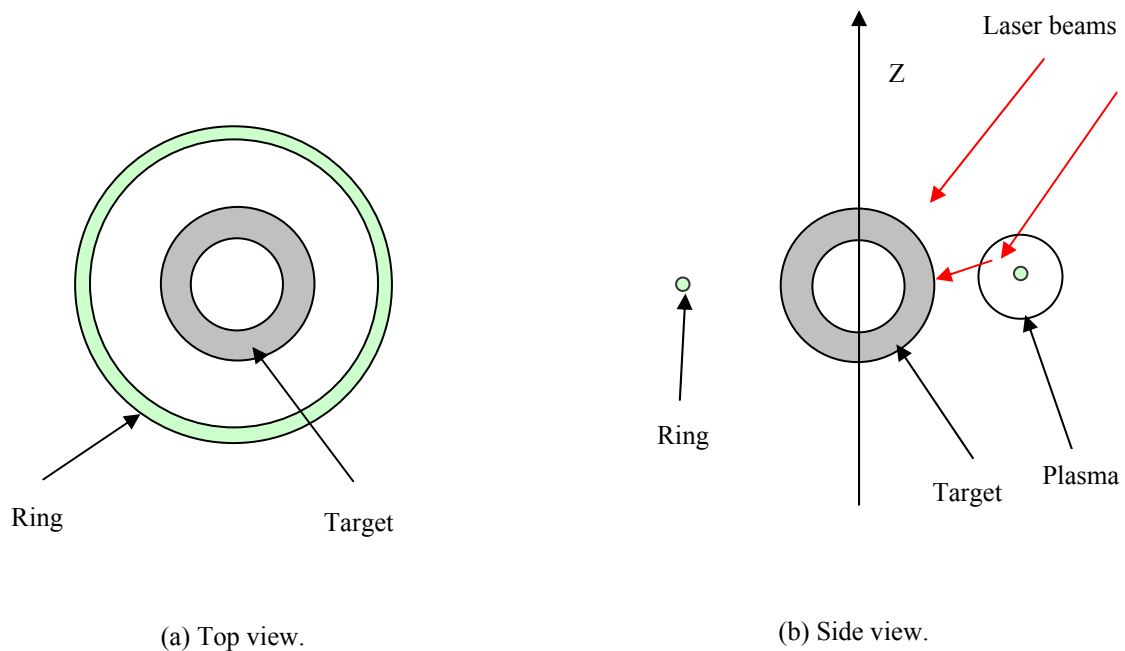
Figure 4: "Saturn" target.

The new target, the so-called "Saturn target," has a small plastic ring around the equator (figure 4)[3]. When the laser is fired, the plastic ring forms a plasma, which causes some of the laser beams to refract, striking the target at the equator.

The Saturn target raises uncertainty in layering. The ring has a higher thermal conductivity than the helium gas in the layering sphere. Hence, more heat is conducted from the equatorial regions of the target than from the polar regions. This causes the ice in the equatorial regions to be thicker than that in the polar regions. However, the degree to which the ring affects the ice thickness is not known.

The primary goal of this project is to ascertain the effect of the ring on the ice layer and, in particular, to determine the size of the ice perturbation.

2. The Program

The project entailed writing a program to model the formation of the ice layer in a cryogenic target. The user defines the target structure, an initial ice layer (specifically the radius of the inner ice surface for each direction (θ, φ) with respect to the vertical axis), and an initial temperature for each part of the system. The infrared heating of the target and the sublimation and condensation of the ice layer are simulated over a period of time defined by the user. The program displays the result with plots showing the new location of the ice layer, as well as the temperature contours inside the target.

The entire layering sphere, including the cryogenic target, is divided into three-dimensional (3-D) grid cells, of which 2-D cross sections are shown in figure 5. This is done in spherical geometry, along the r, θ, and φ dimensions. The grid is typically chosen to be denser in the ice layer, especially near the interface between the ice and gas.

(The fine zoning is expanded beyond the ice layer to accommodate simulations involving severe ice nonuniformities.)
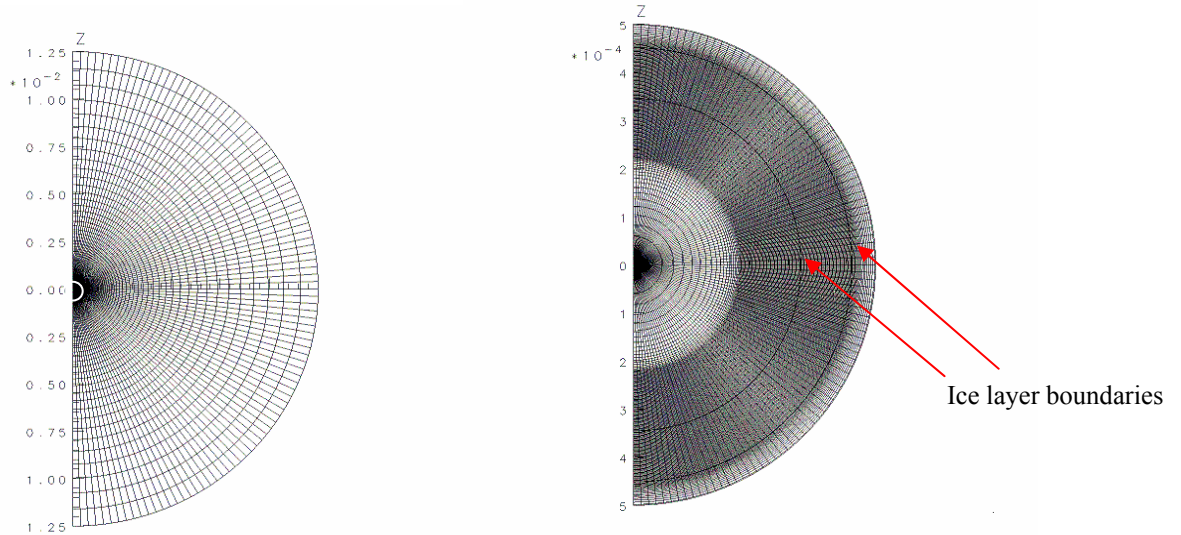
Figure 5: (a) The entire layering sphere divided into grid cells (outer radius=1.25 cm), and (b) the area outlined in white in greater detail (radius = 500 μm). Note the high density of grid cells in and near the ice layer, whose boundaries are shown with dark lines.

The temperature of each cell is stored in a 3-D array, as are the thermal conductivity, the specific heat, and the amount of heat each cell receives from the infrared laser. A two-dimensional array, indexed in the θ and φ directions, keeps track of the radius of the ice-gas interface. Although this particular problem (Saturn ring) is 2-D in nature due to the symmetry in φ, the program was written in 3-D to allow for more complex future applications. The program performs a large number of time steps, each of which is typically a small fraction of a second. During each time step, the new temperature of each cell is calculated, taking into account the infrared heating and thermal conduction. The amount of sublimation and condensation at each interface cell is also calculated, and the new radius of the interface is determined.

The rate of sublimation is a function of the temperature of the solid. Although it is not a linear function, we are working with a very small temperature range near equilibrium. Thus, $\frac{dN_s}{dt}$, the rate of sublimation per unit area in molecules/m^{2}s, is linearized as:

$$\frac{dN_s}{dt} = N_0 + \alpha(T_{solid} - T_{ref}),$$ (1)

where T_{ref} is the reference temperature of 18.6 K, T_{solid} is the temperature of the deuterium ice, N_0 is the rate of sublimation at the reference temperature, and α is a constant coefficient. (See the appendix for numerical values of α and other physical constants.)

Similarly, $\frac{dN_c}{dt}$, the rate of deposition is linearized as:

$$\frac{dN_c}{dt} = n_{gas}\left[\beta - \gamma(T_{gas} - T_{ref})\right],$$ (2)

where T_{gas} is the temperature of the gas, n_{gas} is the density of the gas in molecules per cubic meter, and β and γ are constant coefficients. Subtracting (1) from (2) gives the overall rate of deposition of molecules per unit area:

$$\frac{dN}{dt} = n_{gas}[\beta - \gamma(T_{gas} - T_{ref})] - N_0 - \alpha(T_{solid} - T_{ref}),$$ (3)

In addition, the thermodynamic activity is modeled by the following:

$$\frac{\partial}{\partial t}C_v T = \nabla \bullet \kappa \nabla T + Q_{IR} + Q_L,$$ (4)

where C_v is the specific heat, T is the temperature, κ is the conductivity, Q_{IR} is the infrared heat, and Q_L is the latent heat per unit volume, which is proportional to the rate of deposition of molecules per unit area. It seems reasonable to deposit the latent heat in

9

the solid (rather than the gas) as the slow molecules in the thermal distribution in the gas will excite lattice vibrations in the solid lattice when they are captured. Some of this energy may return to the gas through thermal conduction.

The latent heat is believed to be deposited over a very thin layer, but its distribution is difficult to determine. However, since the thermal conduction will rapidly remove the steep gradients, the exact distribution is not very important here. Numerically, we deposit all the latent heat in the first boundary cell that contains ice. This cell will have

$$Q_L = \frac{L}{\Delta x} \frac{dN}{dt} \ , \tag{5}$$

where L is the latent heat per molecule and Δx is the ice thickness in the cell.

The sublimation and heat transfer occur simultaneously. To calculate the temperature changes, the amount of sublimation that occurred and thus Q_L must be known. Also, the temperatures of the ice and gas at the interface must be known to determine the amount of sublimation that occurs. However, to solve the sublimation and heat transfer in one step would be difficult and computationally intensive, so it was decided to decompose them into two separate procedures. We have separated the problem into a linear equation (Equation (4)) and a few linear and nonlinear function evaluations (Equations (3) and (5)). The heat transfer equation has been well studied. Many mature algorithms exist that can efficiently solve this equation. Equations (3) and (5) can be evaluated in a straightforward manner. As the time step is small the error introduced due to the separation of heat transfer and sublimation/condensation is negligible.

The ice radii calculated after each time step typically do not fall on a cell border. As a result, the interface cell contains both ice and gas (see figure 6). The cells across the

ice-gas interface are modeled using a linear mixture of parameters from both ice and gas, according to the ice/gas ratio within the cell. Specifically, once the ice radii are evaluated, the cells are searched to determine which ones contain the interface. The gas and ice volumes within the interface cells are calculated. The specific heat and the conductivity of the cell are then computed as

$$C_v = pC_{vGas} + (1-p)C_{vSolid} \; , \tag{6}$$

and

$$\kappa = p\kappa_{Gas} + (1-p)\kappa_{Solid} \; , \tag{7}$$

where p and *(1-p)* are the proportions (in volume) of gas and solid contained in the cell, respectively.
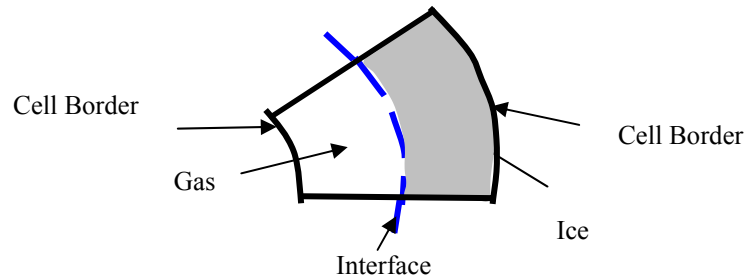
Figure 6: Cell containing the gas/ice interface. Both ice and gas are present in the cell.

A natural approach to predicting the ice shape at the end of the layering process is to set the initial condition to be as representative of the real situation as possible, and run the simulation for the same duration as the real process. As the software time step is typically a few hundred microseconds and the layering requires 24 hours, the number of time steps required is in the hundreds of millions. Two issues emerged with this huge number. First, it would take days to perform one simulation, even with a modern computer. Second, computation errors, such as rounding errors, accumulate during each

step of the calculation. The total error, which is proportional to the number of steps, may be large enough to make the calculation meaningless. The introduction of variable time step techniques, which will be discussed later, can reduce the number of time steps by a factor of about five. However, the resulting number of steps is still extremely large.

It was decided to try a different method. When the layering process approaches the end, the system typically enters a steady state, which means that each part of the system remains almost unchanged. In our application, steady state implies that the sublimation is balanced by condensation, and the temperature of each cell remains constant. The steady state is determined by the system configuration including boundary conditions, heat sources, etc. It is very insensitive to a wide range of initial conditions. Consequently, we may calculate the steady state solution with a small amount of steps if we can find an initial condition (including initial ice geometry and initial temperature) that is close to the steady state. It turns out that this is not a very difficult task. It is known that the steady state for the target without the Saturn ring is a uniform shell. The introduction of the ring does change the steady state. Nevertheless, the magnitude of the change is relatively small. As a result, it can be reasonably assumed that using a uniform shell as the starting point, the simulation may reach the steady state in a short period of time.

Another method of reducing the number of time steps involves applying variable time steps. Specifically, during the initial transition period when the system drastically changes, a smaller time step is applied. Afterwards, when the system is near the equilibrium temperature, we take relatively large time steps. This variable step size scheme was developed based on several observations. A large step size saves time steps,

but it may cause significant calculation error and even instability. The step-by-step

calculation of equations (3)-(5) assumes that within each time step the system variables

including ice radius and cell temperature do not change very much and thus can be

approximated as constants and linear functions. The above assumption could be violated

once a large time step is adopted. However, we noticed that the error in approximation

does not only depend on the time step size, but also on how quickly the system changes.

When the system remains steady, even a relatively large step does not introduce

noticeable error. As a result, the variable time step size approach serves both our goals:

fewer time steps and acceptable calculation error. The maximum ice thickness increment

is used as an indicator for the system change. The time step size is determined to be

inversely proportional to the indicator. A ceiling is imposed to prevent too large a step

size when the change on the previous step approaches zero. More specifically, the step

size for step i is determined as

$$\Delta t(i) = Min(\frac{\Delta r_d \Delta t(i-1)}{Max_{\theta\varphi} |\Delta r_{\theta\varphi}(i-1)|}, \Delta t_{max}) , \qquad (8)$$

where Δt_{max} is the maximum step size allowed, Δr_d is the desired radius change, typically

around 10 pm. $\Delta r_{\theta\varphi}(i\text{-}1)$ is the ice radius change in the direction of (θ, φ) that occurred in

the previous time step, $\Delta t(i\text{-}1)$ is the size of the previous time step, and the maximization

is over all directions. This variable step size approach results in a reduction of the number

of the steps by a factor of about five.

3. Results

      The ice shape of the layered "Saturn" target was determined using the program.

As discussed in Section 2, the initial condition was set with an ice layer of uniform

thickness. The heat absorption of the ice was set at about 46 kW/m^3, approximately the same as the heat produced through beta decay of deuterium-tritium ice[6,7]. The target has a diameter of 900 μm, an ice layer thickness of 100 μm, a ring cross section diameter of 300 μm, and a ring major radius (distance from the center of the ring to the origin) of 1100 μm. The results are summarized in Figures 7 through 9.

Figure 7 shows temperature contours for the target, (a) at time $t = 5$ seconds and (b) after an hour, plotted in polar coordinates. The lines in the contour maps are isotherms, representing locations with the same temperatures. The ice surface radii, which are not plotted, are about 347 μm in both figures (the deviations of the actual radii are too small in scale to be seen in figure 7). While the contours at 5 s reveal irregularities in the temperature distribution within the target, the final contours approximately follow the shape of the ice surface, suggesting an isothermal ice surface. This confirms that the system has entered the steady state at the end of the simulation.
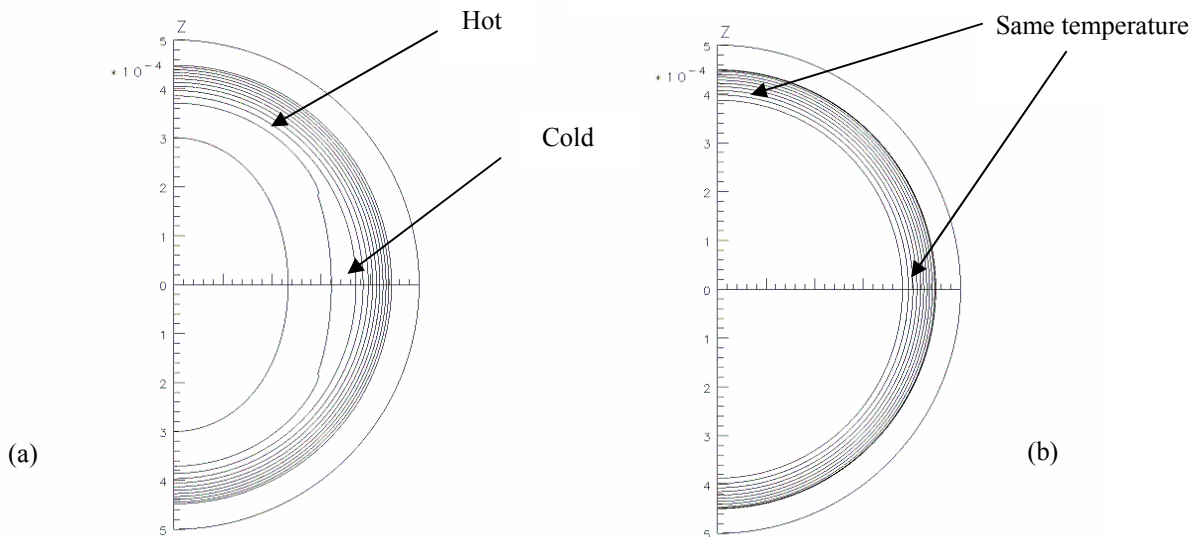
Figure 7: (a) Temperature contours in the target near the beginning of the layering process (t=5 s). The presence of the ring noticeably affects the contours near the equator. The distorted contour shows that the ice surface near the equator is colder than the surface near the poles. (b) Contours after the layering (t=1 h). The z axis is vertical and the outer radius is 500 μm. The outer radius of the target itself is 450 μm.

Figure 8 illustrates the temperature distribution as a function of radius at the

equator ($\theta = 90°$) and at the pole ($\theta = 0°$) in the vicinity of the ice layer, (a) after five

seconds and (b) after an hour. Near the beginning of the layering process, there is a small

but noticeable difference in temperature between the polar and equatorial regions. After

layering, the temperature at the D_2 ice/gas interface is uniform. Also, note the parabolic

temperature profile in the ice layer. The temperature gradient increases towards the outer

surface because the heat flux at each radius must equal the total IR heat deposited inside

that radius. Since the heat flux on either side of the outer ice surface is the same, the low

thermal conductivity of the helium gas causes a steep temperature gradient outside the

ice. There is also a small temperature gradient in the D_2 gas, because of the infrared

heating of the gas. The temperature difference across the ice is about 500 μK, and there
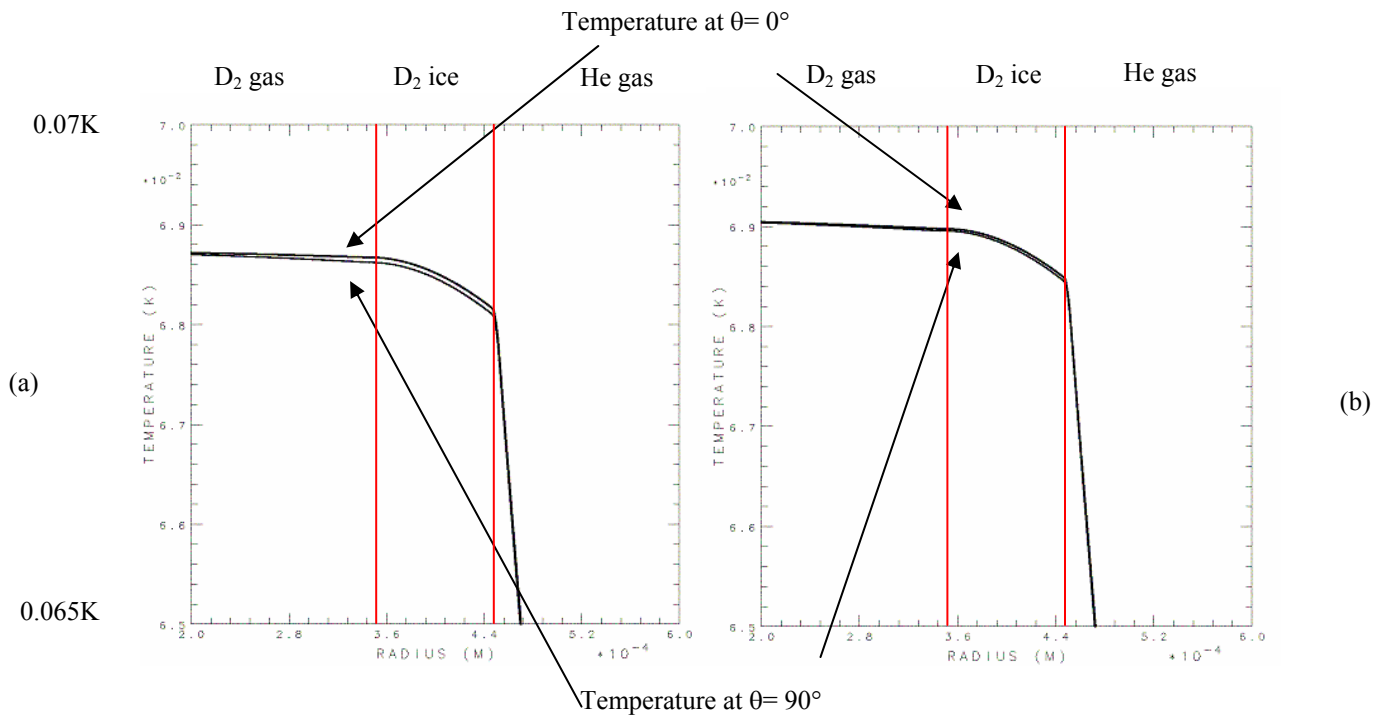
Figure 8: (a) Temperature profile as a function of radius from 200 μm to 600 μm near the beginning of the layering process (t=5 s). (b) Temperature profile after layering (t=1 h). The temperatures on the scale represent the temperature above the reference temperature of 18.6 K. The vertical red lines indicate the ice layer (from 347 μm to 447 μm).

15

is about 0.1 K of difference between the outside of the target and the edge of the layering sphere. The figure indicates that the ice surface temperature approaches uniformity with respect to θ during the layering process.

Figure 9 plots the ice thickness against θ. The red line represents the initial thickness, which is uniform, and the blue line indicates the result after layering. The ice is slightly thicker (the interface radius is smaller) in the equatorial region (θ=90°).

Figure 9 shows that the maximum interface radius after layering is 347.6 μm, which occurs at the poles (θ=0°or θ=180°). The minimum radius, reached at the equator (θ=90°), is 346.3 μm. The largest deviation from the mean radius, which happens at the equator, is about 0.7 μm. As the deviation is within the design tolerance of 1 μm, we may conclude that the ring does not pose a significant threat to ice uniformity.
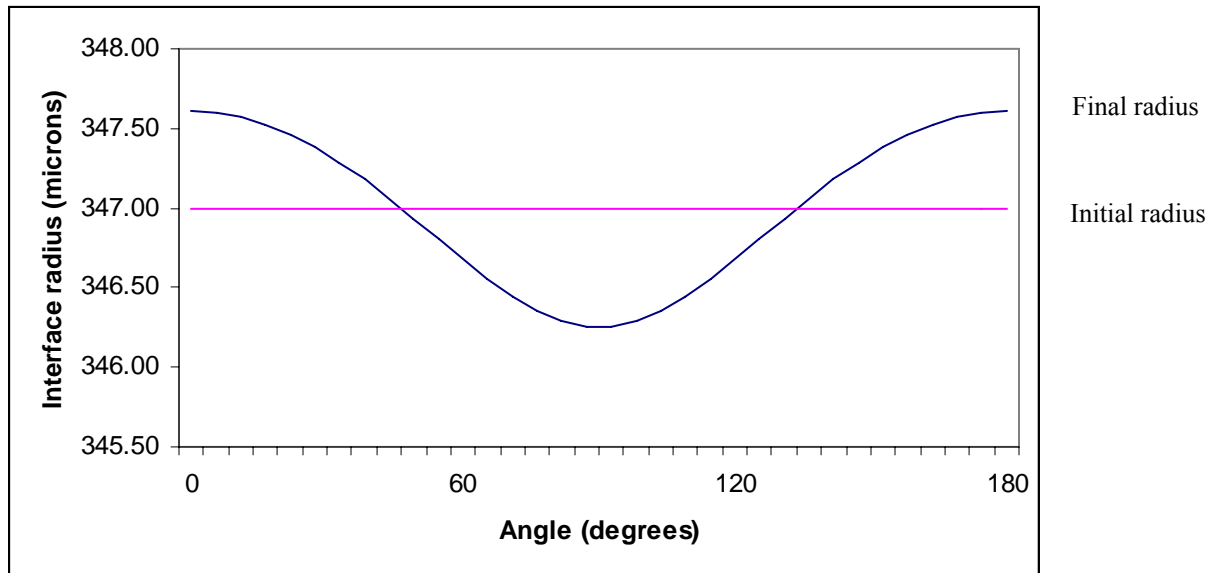
Figure 9: Ice-gas interface radius for different angles θ. The red and blue lines represent the initial and the final radii, respectively. The initial radius was set to be uniform as a function of θ. After layering, the ice becomes slightly thicker (the interface radius slightly smaller) near the equator (θ = 90°) and slightly thinner at the poles (θ = 0° and θ = 180°).

4. Conclusion

A new computer program has been developed to simulate the layering of a cryogenic target. A set of nonlinear partial differential equations was established to model the layering process. The equation set was decomposed into two parts, a linear partial differential equation set and a few linear and nonlinear functions. This significantly reduces computation complexity without noticeably sacrificing calculation accuracy. The interface cells are modeled as a linear mixture of gas and ice.

The program was applied to determine the ice shape after layering for "Saturn ring" targets. Two schemes were developed to reduce the number of time steps. First, the problem was cast into the framework of finding the steady state solution and the calculation was expedited by starting from an appropriate initial condition. Second, a variable time step size was implemented. A larger step size was adopted when the system is slowly varying to ensure computational efficiency, and a smaller time step is used when the system is rapidly changing to avoid large approximation errors.

The result showed that the nonuniformities caused by the plastic rings are small. The largest deviation from the mean radius is about 0.7 μm. This deviation is within the design tolerance of 1 μm, so its impact on fusion performance is acceptable.

5. Acknowledgements

References

[1] J. Nuckolls, et al., *Laser Compression of Matter to Super-High Densities: Thermonuclear (CTR) Applications,* **Nature** Vol. 239, p. 139 (1972).

[2] J. D. Lindl, *Development of the indirect-drive approach to inertial confinement fusion and the target physics basis for ignition and gain*, **Physics of Plasmas** Vol 2, p.3933 (1995).

[3] R. S. Craxton and D. W. Jacobs-Perkins, *The Saturn Target for Polar Direct Drive on the National Ignition Facility*, **Physics Review Letters** Vol 94, p. 095002 (2005).

[4] C. Stoeckl, et al., *First Results from Cryogenic Target Implosions on OMEGA*. **Physics of Plasmas** Vol. 9, p. 2195 (2002).

[5] D. N. Bittner, et al., *Forming Uniform HD Layers in Shells Using Infrared Radiation,* **Fusion Technology** Vol. 35, p. 244 (1999).

[6] E.L. Alfonso, *Modeling the Temperature and Ice-Thickness Profiles Within OMEGA Cryogenic Targets*. **LLE Review** Vol. 81, p.14 (2002).

[7] D. Harding, private communication (2005).

Appendix. List of Physical Constants Used[6,7]

	K (W/mK)	C_v (J/(m^{3}K))	Q_{IR} (W/m^3)	L (J/molecule)
Solid D$_2$	0.38	5.802×10^5	4.6×10^4	9.80×10^{-22}
Plastic	0.05	1.95×10^5		
Helium	0.0227	0.969		
D$_2$ gas	0.009	2155	4.6	

T_{ref}	18.6 K
N_0	4.89×10^{22} molecules/(m^{2}s)
α	2.43×10^{22} molecules/(m^{2}sK)
β	7.84×10^{-4} m/s
γ	-2.11×10^{-5} m/(sK)

Relative Quantum Efficiency Measurements of the ROSS Streak Camera Photocathode

Alex Grammar

Relative Quantum Efficiency Measurements of the ROSS Streak Camera Photocathode

Alex Grammar

Advised by Dr. Jaanimagi and Mr. Boni

Laboratory for Laser Energetics
University of Rochester
Rochester, New York 14623-1299

__Abstract__

Streak cameras are vital to the daily functioning of the LLE facility, providing the ability to time-resolve high-speed processes occurring in the fusion environment. Even with standardized cameras, such as the Rochester Optical Streak System (ROSS), readings on an identical source can vary over multi-year timescales. Many factors may contribute to these fluctuations, but the most likely cause is degradation of the photocathode. Measuring the absolute quantum efficiency of a streak tube's photocathode is a lengthy and expensive process. The goal of this project was to develop a simple method of determining a ROSS camera photocathode's relative quantum efficiency quickly in a lab setting. This would allow the photocathode response to be monitored on a yearly basis. Furthermore, a method of converting relative measurements into absolute measurements was investigated.

Background

The photocathode element inside the streak tube converts light intensity into an electron current density through the photoelectric effect. The streak tube then converts the electron signal into an image of light intensity vs. time. The photocathode itself is a thin (~100 nm) thick layer of photoemissive material. The two variants used in the ROSS cameras are S1 and S20 photocathodes. The S1 is a silver oxide compound, whereas the S20 is sodium/potassium/antimony; both are doped with cesium. Cesium is used because it has the lowest work function of all elements.

The signals these tubes produce will degrade over time even though the tubes are kept evacuated to increase the mean free path of the electrons to a few kilometers. The major source of degradation comes from ion feedback. A very small fraction of the electron beam generated by the photocathode will collide with the residual gas molecules in the tube, creating ions that are accelerated back to the photocathode, causing severe physical damage. This degradation occurs continuously due to the inherent dark current, thermally excited electrons emitted spontaneously from the photocathode. This dark current creates a noise level in all readings taken by the device and can easily drown out weak signals. Each photocathode type has a specific spectral response[1], (**Figure 1**). As the photocathode ages the quantum efficiency will decrease, predominantly at the longer wavelengths. Eventually the streak tube will be deemed non-responsive. The current solution to this problem is to replace the camera and to diagnose the detailed status of the tube through a lengthy and costly absolute quantum efficiency measurement. The goal of this project was to create an alternative method of diagnosing and evaluating this degradation.
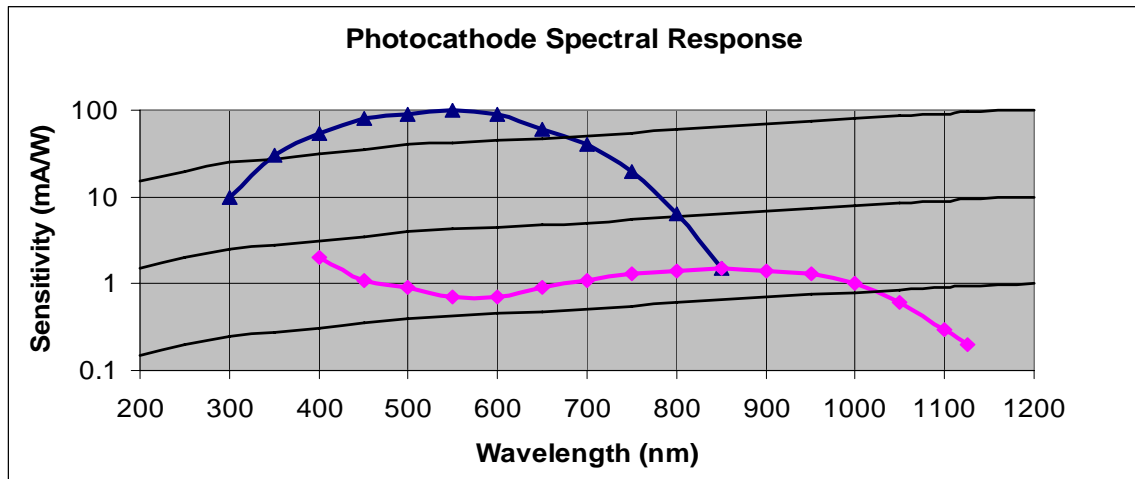
Figure 1: Spectral response of two common photocathodes. The S-20 variant is the upper line and S-1 is the lower line. The black curves are .1%, 1%, and 10% quantum efficiency lines from the bottom respectively. (2)

Experiment

The system to be designed, to provide relative quantum efficiency, had a few prerequisites. It was to be compatible with ROSS cameras and provide a stable illumination source. The source's intensity and wavelength had to be easily controlled by the user, and the device had to connect to the ROSS camera in a light-tight fashion. LEDs were chosen as the illumination source because they are cheap, stable, reliable and controllable. Also specific wavelengths can be easily selected for testing. An opal glass diffuser was placed in front of the LED to spatially homogenize the light output.

The method in which the relative measurements would be taken is dependent on the structure of the streak tube itself. The tube is normally operated with the photocathode at -15 kV and various other voltages on the other internal electrodes. The photocathode response can, however, be accurately measured at much lower voltage. A potential of -50V was applied to the photocathode to facilitate electron emission. All of the other internal electrodes were connected together to the common ground. This grounding allows us to measure the total output current as accurately and non-invasively

as possible. We measured the current to the photocathode with an ammeter in series. The output current was run thorough a 1 MΩ resistor in parallel with a voltmeter; essentially an ammeter. Both meters allowed for current readings with nanoampere precision. The LED intensity was adjusted with a simple voltage regulator circuit controllable at the millivolt level, (**Figure 2**).

The external shell was printed on a 3D-plastic printer and painted black to block all external light, (**Figure 3**). This setup gave us relative quantum efficiency measurements of the photocathode, but these relative measurements could be easily converted into absolute measurements. This was accomplished by measuring the light intensity output with a CCD camera at the exact distance from the LED as the photocathode. The typical quantum efficiency of a silicon CCD detector (which is stable over time) was used to estimate the absolute LED intensity. Knowing the LED intensity at certain voltage levels, we can convert the photocathode current readings to an absolute quantum efficiency.
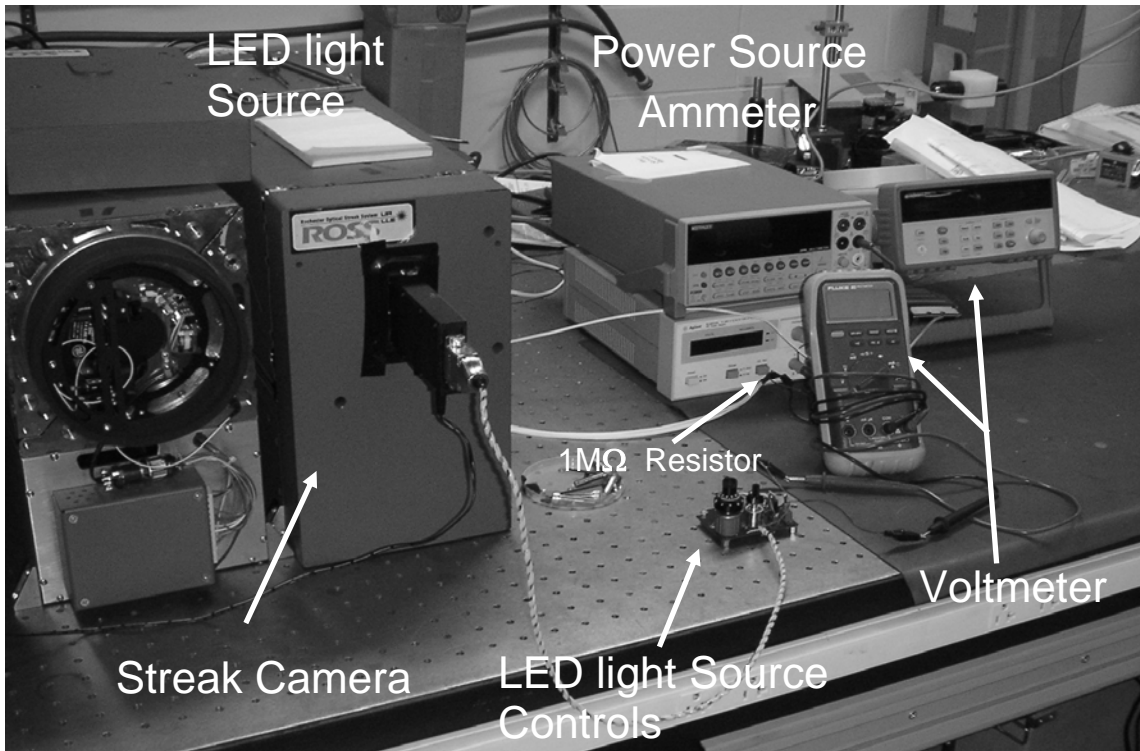
Figure 2: Experimental setup includes measurements of the input and output currents.
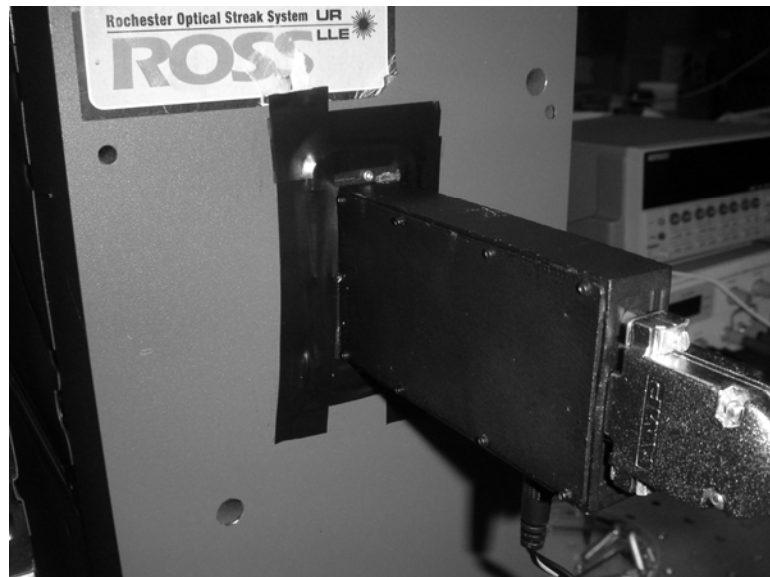
Figure 3: External LED housing with control and power cables, attached to a streak camera

Results

The photocurrent readings with the red/green/blue LED ranged from 0.1 to 100 nA. The angle of the LED with respect to the opal glass diffuser caused slight variations in the current readings. After modifying the LED mount, we were able to stabilize the readings and produce better data. Multiple readings of the same streak tube taken over a two week period were reproducible and show that the relative quantum efficiency measurements can be used to monitor photocathode sensitivity. Also, using the CCD camera to monitor the input light level, the relative measurements can be converted into absolute. The absolute measurements show some discrepancy with the manufacture's data sheet[2], (**Figure 4**). This can be due to an error in the estimated CCD quantum efficiency, and also a variation in the spatial uniformity of the photocathode sensitivity.
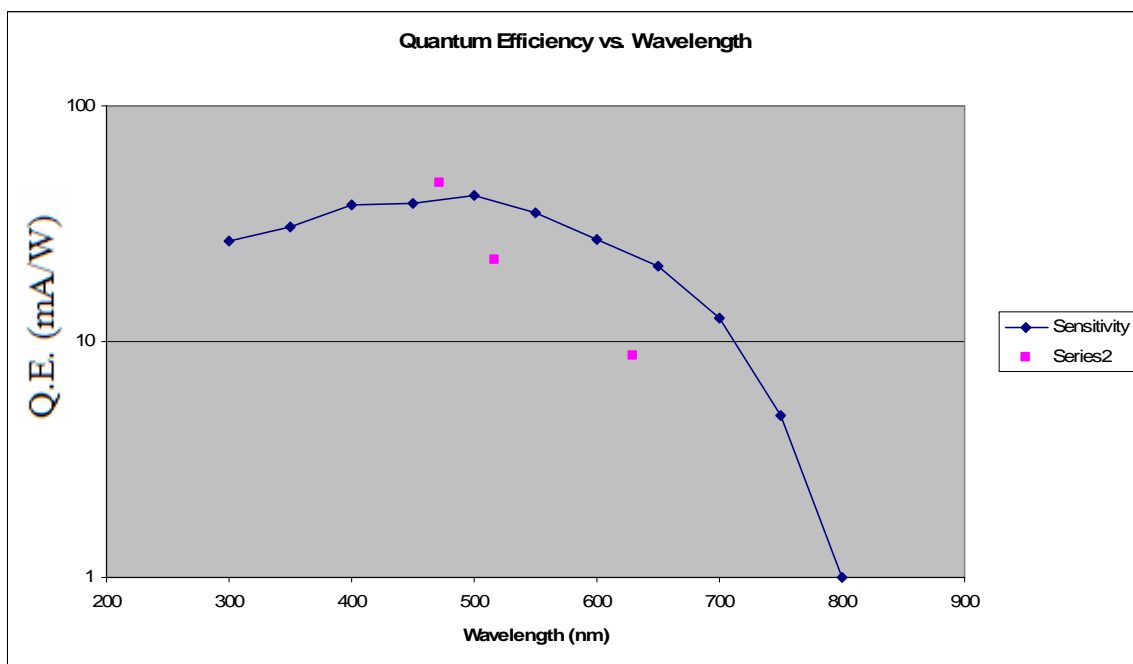
Figure 4: Referenced relative measurements: The readings that were taken at the three different wavelengths were referenced with intensity calculations derived from CCD camera readings. These crude absolute measurements were then overlaid on an average spectral response of a S-20 photocathode to estimate the accuracy of our relative to absolute conversion method.

Conclusion

The main purpose of this project was to demonstrate the effectiveness of using relative quantum efficiency measurements to diagnose streak camera photocathode degradation. The device was easily able to generate substantial readings well above the dark current noise floor with minimal illumination. Converting these relative measurements into absolute was also investigated and found to be equally promising. The five ROSS cameras that were evaluated for this project now have a baseline from which future quantum efficiency measurements can be referenced.

References

1. Philips, Photomultiplier tubes, principles & applications, (Brive, France 1994) Sec. 1.1

2. Photonis, Brive France. Photocathode spectral response specification sheets

Characterization of a High-Energy X-ray Compound Refractive Lens

Stewart Laird
Advisor: Dr. Jim Knauer

Traditionally, high energy x rays are notoriously hard to focus for imaging purposes due to an extremely low degree of refraction in solids. Using a device composed of many small adjacent lenses (a Compound Refractive Lens, or "CRL") it is possible to achieve images with much better resolution than current methods of high-energy x-ray imaging such as pinhole cameras. The literature shows potential resolutions of 1-2 μm for a CRL x-ray lens. An image resolution of smaller than 5 microns would allow accurate imaging of the 20-50 micron core of fusion implosions in the Omega laser system. A commercial compound refractive lens has been purchased and analyzed experimentally for image resolution and quality. Preliminary data has suggested that with proper alignment and focus, resolutions of 6.8 +/- 1.5 microns or better are possible. As long as no significant spherical or chromatic aberrations appear, this data would encourage future research into implementing CRL technology into existing Omega camera mounts.

The motivation for integrating compound refractive lenses (CRLs) into the LLE Omega system lies in the fact that CRLs can provide high resolution images of high energy x rays. During fusion implosions, there are three types of radiation emitted that are useful for imaging: neutrons, gamma rays, and X rays. Neutrons are emitted primarily in areas with high density and high temperature and therefore are a prime candidate for imaging regions where fusion is occurring. However, the highest resolution that has been achieved thus far with neutron imaging is greater than 50 microns. Gamma rays are emitted from the matter evaporated
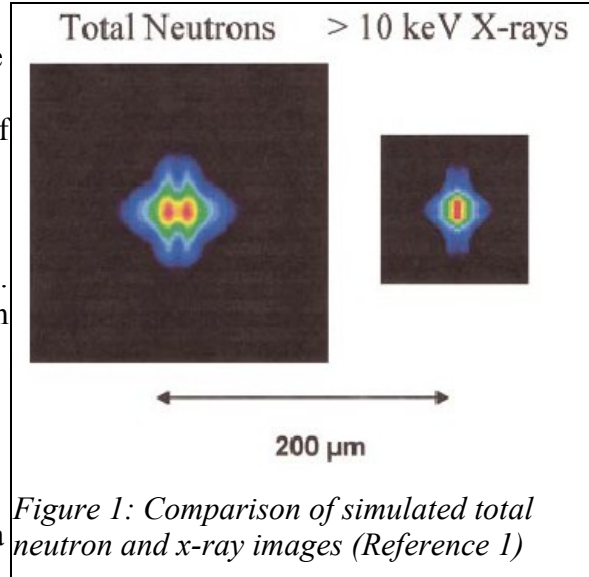
Figure 1: Comparison of simulated total neutron and x-ray images (Reference 1)

off the target, and therefore do not provide a useful image of the fusion core. High energy x rays, as shown in a simulation done at Los Alamos (Figure 1), are emitted from the same high interest areas of the implosion. High energy x rays are difficult to image due to high absorption and low refraction in solids. However, CRLs are capable of overcoming these obstacles and achieving very high resolutions. Although CRLs are designed to circumvent the difficulties of high-energy x-ray propagation, they introduce some other problems such as precision alignment and are not able to compensate for chromatic aberration, a factor that results in a large reduction in image quality when using a polychromatic source.

The low refraction and chromatic aberration result from high-energy X ray's abnormal behavior in solids. The complex index of refraction is given by the equation

$$n = 1 - \delta - i\beta$$

where n is the index of refraction, δ is the real refractive index decrement, and β is the imaginary absorption factor. The complex index of refraction can also be expressed by the equation

$$n = 1 - \frac{r_0}{2\pi} \lambda^2 \sum_q n_q f_q(0)$$

where n is the index of refraction, r_0 is the classical electron radius, λ is the wavelength of the interacting x ray, n_q is the number of atoms q per unit volume, and f_q is the atomic scattering factor of that atom, a complex number determined for each atom.

For most solids the refractive index n increases with n_q. However, for x rays n decreases as n_q increases. This is due to the fact that the high frequency of x rays causes them to interact with most solids as plasmas, interacting with the outer electrons. The consequence of this is that for a converging lens, a concave lens shape is necessary. δ is also very small for high energy x rays, generally between 10^{-5} and 10^{-7}. The consequence

of this is that x rays have only a very small degree of refraction through a single lens. Also, these equations show that δ and λ^2 are directly proportional, which will become relevant when looking at the effects of large wavelength bandwidth sources on the focal length. The equation (Reference 2)

$$f = \frac{r}{2N\delta}$$

where f is the focal length, r is the radius of a lens, N is the number of lenses and δ is the index of refractive decrement, relates the focal length to the decrement. From this information combined with the previous relationships, the fact that

$$f \propto \frac{1}{\lambda^2}$$

can be concluded. This means that the focal length is highly dependent on the wavelength of the x rays passing through the lens. Therefore, in order to achieve high resolutions, the beam of incoming x rays must be monochromatic.

CRLs are specifically designed to overcome the obstacles of high-energy x-ray imaging. They are comprised of many thin lenses, which serves to reduce the focal length of the lens to reasonable distances, as shown in the focal length equation above. The fact that each individual lens is extremely thin in comparison to its focal length allows the use of the thin lens formula

$$\frac{1}{f} = \frac{1}{d_i} + \frac{1}{d_o}$$

where f is the focal length, d_i is the image distance, and d_o is the object distance, to determine proper placement of the lens.

Bubble CRL lenses are constructed by filling a tiny glass capillary with a low-Z epoxy (for good transmission of x rays) and then blowing bubbles into it. As shown in Figure 2, the concave epoxy walls left between the bubbles form spherical lenses. The concave shape converges x rays as opposed to diverging visible light because the index of refraction of x

Figure 2: Photograph of a bubble CRL (Reference 3)

rays is less than one. By utilizing a large number of lenses, the focal length can be reduced enough to integrate a lens system onto an existing camera mount on the Omega laser.
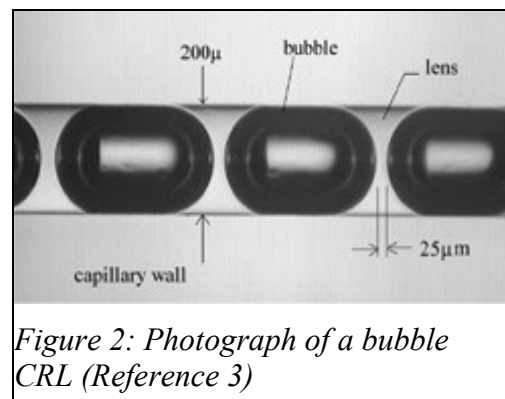
The CRL purchased for examination is a 267-lens bubble-style CRL (Figure 3). The diameter of each lens is 200 μm. The total thickness of the combined lenses is 4.47 mm. The exact chemical composition of the epoxy used was not provided by the manufacturer, but considering other epoxies produced by the same manufacturer, the chemical formula was estimated to be $C_{100}H_{200}O_{20}N$. The total lens length is 7.5 cm.
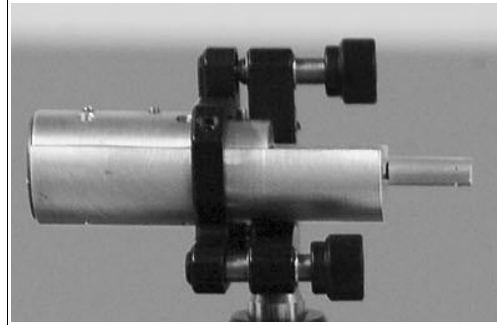

Figure 3: The CRL is held in the aluminum casing protruding from the right side of the V-groove mount

In order to determine the focal length of the lens, calculations were done to compare theoretical lengths versus the data sent from the lens's manufacturer, Adelphi. The values reported by Adelphi were focal lengths of 33 cm at 20.2 keV and 19 cm at 15.4 keV. The focal length was calculated to be 5.26 cm at 8.03 keV. Object and image distances were then

Table 1.	Object and Image Distances Calculated for Different Magnifications at 8.03 keV with a Cu X-ray source
Test Energy (keV)	8.03
Reference Energy (keV)	20.2
Ratio	0.4
Ref Focal Length (cm)	33.3
Test Focal Length (cm)	5.26
Magnification	15
Grid Distance (cm)	5.61
Film Distance (cm)	84.15
Total Distance (cm)	89.76
Magnification	10
Grid Distance (cm)	5.79
Film Distance (cm)	57.85
Total (cm)	63.64
Magnification	5
Grid Distance (cm)	6.31
Film Distance (cm)	31.56
Total (cm)	37.87

calculated for a variety of magnifications as show in Table 1.

At a magnification of 5x, the image needed to be placed 6.31 cm away from the center of the lens. This table was used to determine the placement of the target and the film during test exposures.

When using a bubble CRL, the field of view is very small due to the elongated shape of the lens. Using the formula (Reference 4),

$$D_{abs} = 2\sqrt{R^2 - (\frac{h_{abs} - h}{2})^2}$$

where R is the radius of the opening, *h* is the thickness of the lens, h_{abs} is the total distance between lenses, and D_{abs} is the absorption aperture radius, D_{abs} was determined to be 189.4 µm. Using the field of view formula,

$$\Phi = \frac{2\,D_{abs}\,a}{l}$$

where *a* is the distance from the lens to the object, D_{abs} is the absorption aperture radius, and *l* is the total length of the lens, a field of view of 318 µm at 5x magnification was calculated. This translates to approximately 4.9 milliradians. One consequence of such a small field of view is that the lens system must be placed very carefully in line with its target. This field of view is wide enough to image the fusion core by a large margin. If the claims made by Adelphi Technologies regarding the accuracy of their laser alignment system are correct, the laser sight should put the target within the field of view.

Figure 4: 400 mesh Au Grid, Image by Adelphi Tech.

For a preliminary measure of the spatial resolution of the lens, an image taken by Adelphi Technologies with our lens was analyzed (Figure 4). The bright squares correspond to the gaps in the Au grid. The image was taken by a 20.2 keV Rh source. The picture is of a 400 mesh Au grid under 2x magnification. The focal length was reported as 33 cm at that energy. Using an image analysis suite called PV-Wave, the image was rotated, and vertical slices crossing the mesh bars were selected along paths that were relatively clear of artifacts or irregularities. Figure 5 is a plot of one of these slices.
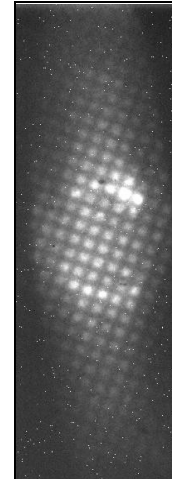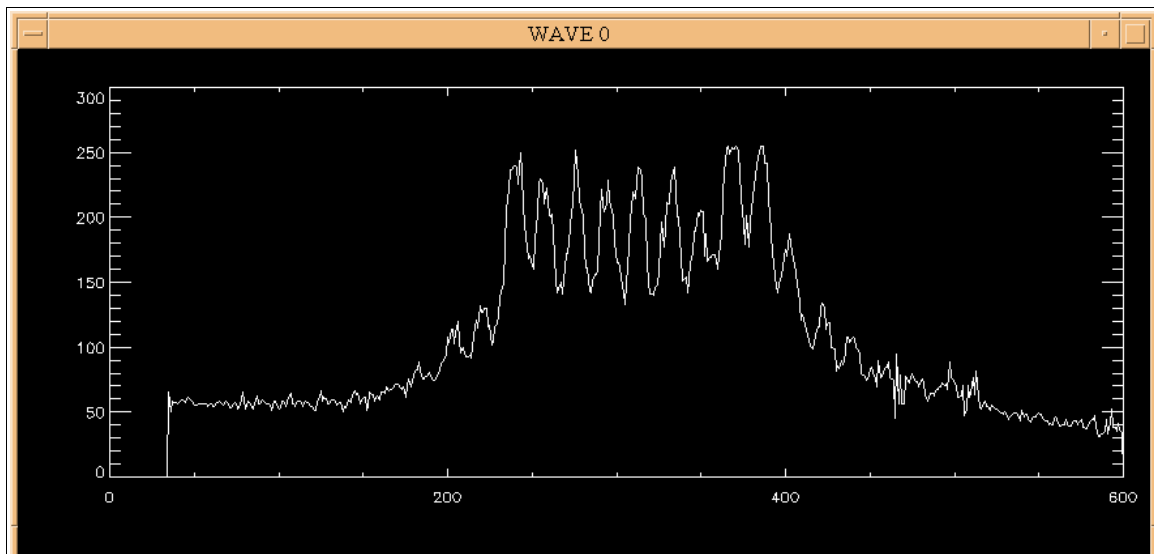

Figure 5: Shown is an example plot of pixel brightness on the vertical axis versus position on the horizontal axis. The peaks correspond to the bright patches in Figure 4, and the depressions correspond to the bars of the grid.

The curve was smoothed with a nearest neighbor method for a clearer result, and the derivative of the data was plotted. A perfect resolution would yield an infinite derivative at the boundary of grid bar and back light. To determine how far off infinity this image was, a Gaussian equation was fitted to the boundary areas on the plot and an average was recorded.

The Gaussian equation is

$$G(x) = Ae^{\frac{-1}{2}\left(\frac{x-x_0}{\sigma}\right)^2}$$

where A is the amplitude, x is the position, and σ is a representation of the width, or resolution. The value of σ was converted from pixels to μm and used as a representation of the resolution potential of the lens. Figure 6 shows the absolute value of the derivative graph along with Gaussian curves. By fitting curves to the graph of the derivative it is possible to quantify the width of blur at the edge of each grid bar in the image. Table 2 shows the collective sigma data with an average and standard deviation.
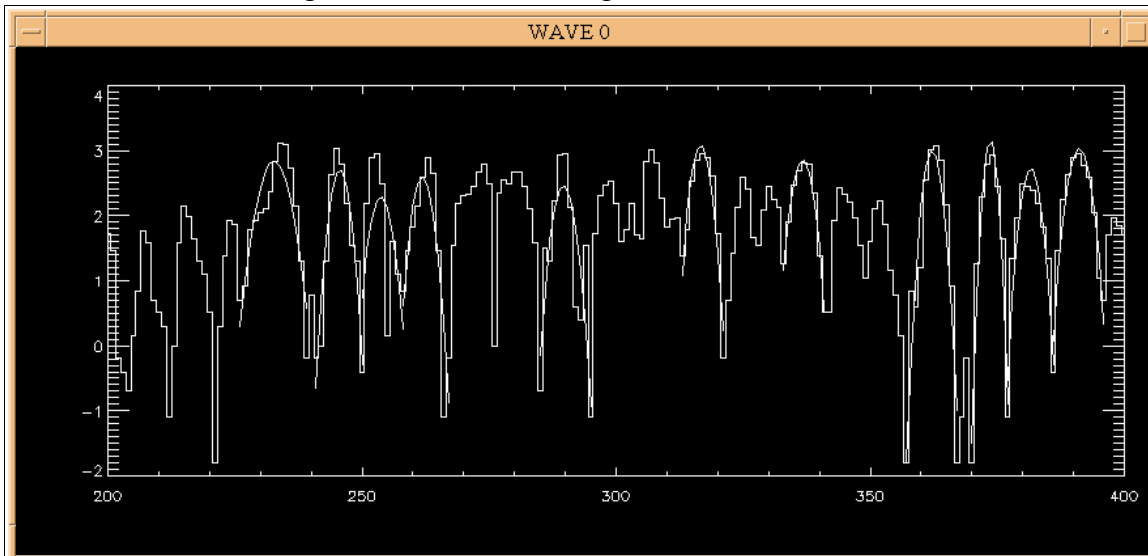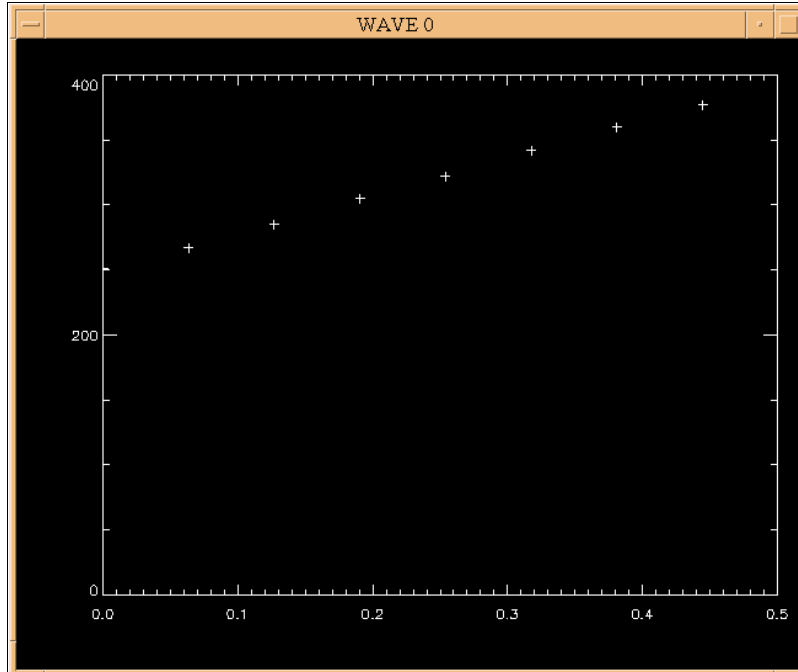

Figure 6: The vertical axis of this graph is the natural log of the brightness. The horizontal axis is pixel position. Gaussian curves are shown over the data.

Table 2   Average Gaussian Curve Fit Variables and Standard Deviations

	σ	X_0	ln A	A
Average:	1.95	312.3	2.8	17.04
STDEV:	0.43	58.31	0.28	4.46

Table 2: This table shows the average Gaussian variables calculated from the PV-Wave output variables along with their standard deviations. These values were used to calculate the spatial resolution and error range.

Because it was a known mesh (400 bars per inch), it was possible to determine the ratio of μm/pixel. To establish the value, the pixel peak i versus i/400 * 2.54×10^4 was

Figure 7: This graph has pixel peak i on the vertical axis versus i/400*2.54x10⁴. The linear slope of the graph is the ratio of μm/pixel

plotted for several consecutive points and the slope was determined (Figure 7). The ratio was determined to be 3.47 μm/pixel. 1.95 average pixels * 3.47 μm/pixel = 6.8 μm resolution. The following formula was used

$$\frac{\Delta\,\text{res}}{\text{res}} = \sqrt{(\frac{\Delta\,\text{pixel}}{\text{pixel}})^2 + (\frac{\Delta\,\text{u/pixel}}{\text{u/pixel}})^2}$$

with the values Δpixel = .43 (one standard deviation), pixel = 1.95, Δu/pixel = 6.619×10^{-6} (as reported by PV-Wave from the linear curve fit, see Figure 7), and u/pixel = 3.47 to determine the error range. The range was determined to be +/- 1.5 μm.

The high energy x-ray apparatus was used with a Cu source with an energy of 8.03 keV. The beam was relatively monochromatic, which is necessary for the best possible resolution. As a target, there were available rings of copper 400 mesh that needed to be placed in an optical mount. A plastic holder was designed to house the grid. The white lens mount can be seen in the left of Figure 8. The mount consisted of a rectangle capable of fitting on the stand, with two concentric holes drilled (one slightly deeper and of smaller radius) and a through-hole. The grid was placed in the smaller hole and held in by a rubber o-ring.
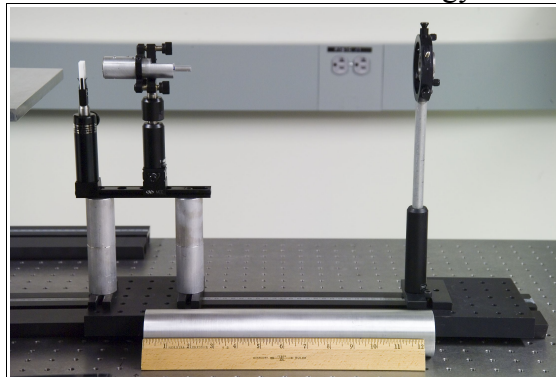
Figure 8: The "telescope" lens system, with (from left to right) grid mount, lens mount, and light-tight film pack containing Biomax x-ray film.

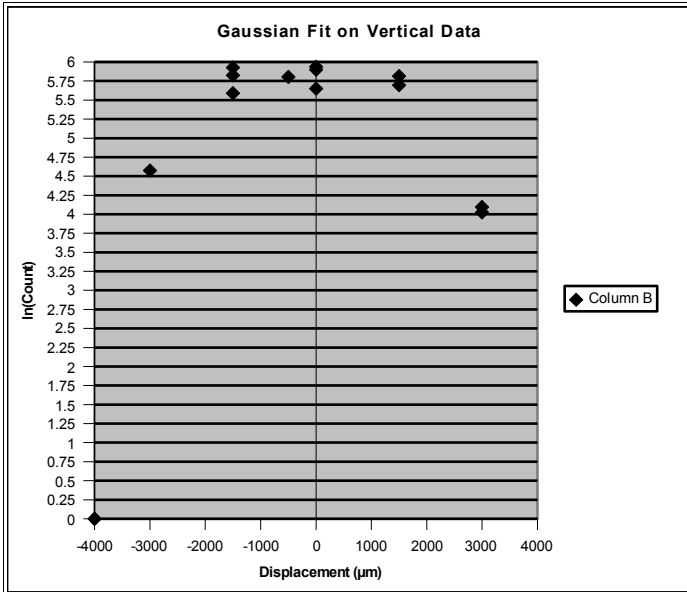**Gaussian Fit on Vertical Data**

Figure 9a: A vertical scan of the beam area showed peak photon counts very close to the initial placement of the diode. The x axis is displacement in µm, and the y axis is the ln of the photons detected in 1 minute
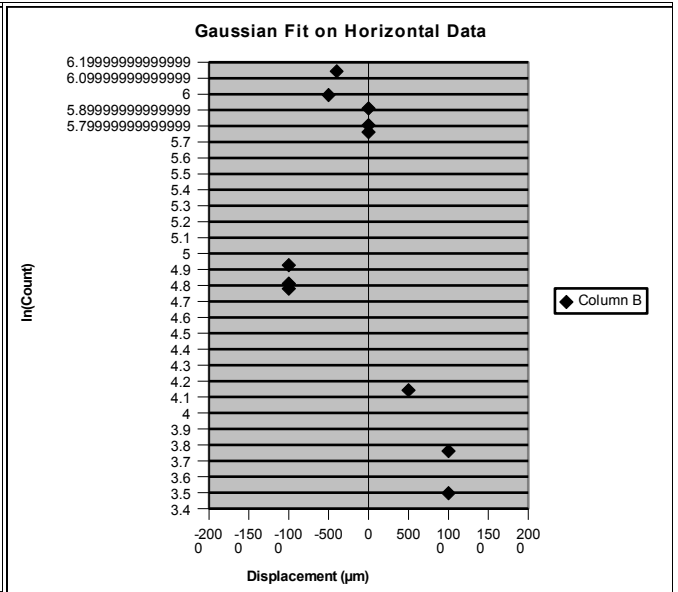

Gaussian Fit on Horizontal Data

Figure 9b: Horizontal scan data. This plot demonstrates the significantly thinner horizontal dimension of the x-ray beam. The peak output is located 500 µm to the left of the initial diode placement.

The lens system was constructed and placed in front of the x-ray beam line. It was necessary to pinpoint the exact beam location since the field of view of the CRL is so small. After using a transit to place the x-ray source in line with the exit slit in the source casing, a pin diode was placed on a set of micron-precision vertical and horizontal motors. The pin diode was used to attempt to locate the beam in both horizontal and vertical dimensions so that proper placement of the lens system would be as simple as possible.

The pin diode was calibrated using the Iron-55 Ka1 and Kb1. A scan across the estimated x-ray beam location was performed, and graphs produced of the photon counts. This allowed for the determination of the peak of the beam intensity, as well as the width of the beam, in order to achieve optimal placement of the lens system (Figure 9). In the vertical dimension, the σ, or graph width, was nearly 1300 µm. In the horizontal dimension, σ was 500 µm. Both were large enough that the beam should encompass the entire view of the lens, with some room for error.

After beam determination, the lens system was put into place. The lens and film pack were
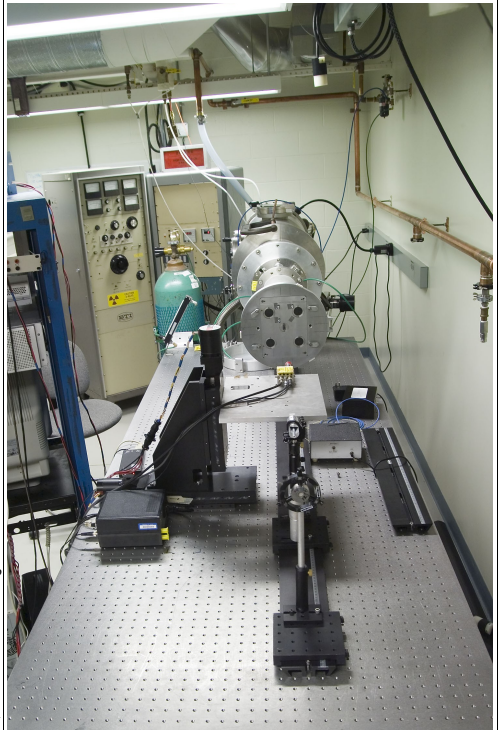

Figure 10: The laboratory apparatus, with lens system in the foreground, the pin diode in the middle of the table, and the x-ray source casing.

removed (lens v-groove mount remaining with the tungsten pinhole) and the system was adjusted for maximum transmission. The lens system had been previously aligned by using Adelphi Tech's provided laser alignment system, in which a glass capillary laser of the same diameter as the lens holder was used to aim the lens both at the grid and the film. The laser supposedly has the same field of view as the lens. The laser alignment system was also used to verify alignment with the x-ray source. This method of alignment could potentially cause problems in the future. This alignment procedure relies on the consistency of the placement of the capillary laser and CRL, as well as the stability of the mount. The repeatability of the lens alignment is low, due to the uncertainty of the x-ray beam optical axis itself, as well as the difficulty of placing the lens system's optical axis in line.

Image attempts were mostly unsuccessful. An image was taken through the tungsten pinhole without the lens in place, but even with 3 hour exposure times, no images with the lens in place were achieved. Though potentially a problem of alignment, it was also calculated that with the current x-ray source it was nearly impossible to get an exposure in any reasonable amount of time.

With a field of view of ~300 μm and a magnification of 5x, the total target area on the film is $4.4 \times 10^5 \, \mu m^2$. With the current x-ray source the count rate through the lens was approximately 10 photons per minute. Assuming that an image could be formed from 1 photon per μm^2, it would take 4.4×10^4 minute, or 730 hours. In order to reduce the time to a more reasonable 3 hours, the count rate would need to raise to 44 counts per second or more, a 250x increase.

There are multiple options for improving the count rate. Lowering the magnification to 2x would help, but will still result in unacceptable exposure times. The transmission through the 4470 μm of epoxy at 8.03 keV was determined to be approximately .08 (See Figure 11). A higher energy x-ray source could improve transmission. Improving the intensity of the x-ray source is another possible option. Currently there are no higher energy x-ray sources available at the LLE, and the source had already been optimized for maximum intensity. Very high energy x-rays are available at the medical center of the University of Rochester, but they are not

Figure 11: Transmission vs. photon energy through 4470 μm of epoxy (Reference 5)

monochromatic and therefore would result in a blurry image. A combination of a higher energy source, lower magnification, and time for a very long exposure might be able to generate images for analysis. Another possibility would be collaborating with Cornell University to use their x-ray source facilities, which would be an advantage because higher energies could be achieved. This would also possibly help with the difficult alignment and beam collimation.

The preliminary determination of the resolution to be 6.8 +/- 1.5 microns is good enough to warrant further investigation, whether it be at the LLE, or at Cornell
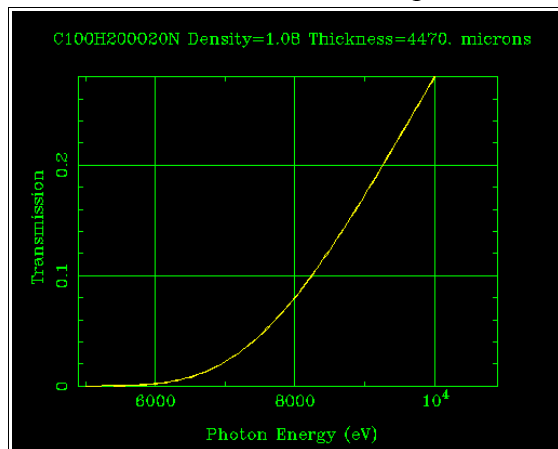
University. The resolution is good enough to image the fusion core with proper alignment. It will be necessary to image a monochromatic x-ray beam. Dopants in the fuel pellets or a monochromator will be necessary to achieve this excellent resolution that has been demonstrated. It was not possible to examine the possibility of distortion such as spherical aberration on an original image. However, there was no sign of distortion in Adelphi's image. For the actual integration on the OMEGA laser system, a single-piece system should be able to be constructed that would fit inside existing camera mounts and be aligned with the implosion location.

References

1. P.A. Bradley, D.C. Wilson, F.J. Swenson, G. L. Morgan, "ICF ignition capsule neutron, gamma ray, and high energy x-ray images," *Review of Scientific Instruments*, Volume 74, Number 3 (2003)

2. Jenkins, F A and White, H E , Fundamentals of Optics, 4E, McGraw-Hill, 1976.

3. Adelphi Technology Inc. http://adelphitech.com/ 8/22/05

4. C.K. Gary, Yu.I. Dudchik, S.A. Pikuzm T.A. Shelkovenko, K.M. Chandler, M.D. Mitchell, D.A. Hammer, "X-ray imaging of an X pinch plasma with a bubble compound refractive lens," *High Temp. Plasma Diagnostics Conf. 2004* – paper E07

5. Eric Gullikson. *X-Ray Interactions With Matter*, http://www-cxro.lbl.gov/optical_constants/filter2.html, 8/21/05

Acknowledgments

Dynamic Energy Grouping in Multigroup Radiation Transport Calculations

Brian Macpherson

Penfield High School

Advisor: Dr. Reuben Epstein

University of Rochester

Laboratory for Laser Energetics

2005 Summer High School Research Program

Abstract: Radiation is an important energy transport mechanism in laser-plasma interactions. In simulating radiation transport through a medium, the radiation spectrum is currently represented as being divided into photon energy intervals or "groups". The radiation emission and absorption rates are calculated and the equation of transfer is solved for each energy interval to obtain the radiation intensity spectrum. This radiation intensity is then used to calculate useful properties such as matter temperature and energy density. Since some photon energies are very important while other photon energies have little effect on the simulation, the intervals can be re-grouped into a smaller number of intervals to save processing time. The range of important photon energies changes over time, however, so it is desirable to change the groupings accordingly. It is possible to decrease the computation time by dynamically re-grouping the photon energies rather than uniformly resolving the entire spectrum. This reduces the number of groups while preserving much of the accuracy guaranteed by the larger number of energy groups currently used. A program has been written to solve the equation of transfer for a standard test problem. This program allows the user to visualize absorption and emission in space and spectral energy, and automatically chooses new, broader energy groupings at a specified time. The program continues with the new groupings for the rest of the simulation.

Introduction: Currently at the Laboratory for Laser Energetics, several one and two-dimensional hydrodynamic simulation codes such as LILAC and DRACO are used to simulate the conditions of a fusion implosion. These simulations are of paramount importance for scientists and engineers who must simulate nuclear fusion in order to study it. These programs can take hours or days to run, however, which hinders research and progress. Some of the main components of these programs are the energy transport mechanisms such as thermal and radiation transport, which calculate and describe how energy comes and goes within the medium. In my project, only radiation transport and its equation of transfer were dealt with. To evaluate the equation of transfer for radiation transport, opacity and emissivity must be evaluated at all relevant photon energies in order to determine the energy intensity. To accurately represent the integrated photon energies, the spectrum can be at first broken into many small groupings. This method ensures accurate results, but is very taxing on the computation time. A method was proposed to cut down on computation time by analyzing the radiation energy density and/or absorption and emission rates in the simulation at specified times to determine which photon energy ranges have the largest effect on the simulation at these times.[1] The program could then determine new groupings of photon energies which accurately represent the important photon energies with a smaller number of total groupings. This would ensure accurate results while reducing simulation time.

Radiation Transport: Calculating radiation transport is one of the most time-consuming aspects of hydrodynamic simulations at the Laboratory for Laser Energetics. The Equation of Transfer for radiation transport is used to describe the energy radiation intensity, $I_v(s)$, distributed within a medium.[2]

$$dI_v/ds = \varepsilon_v/4\pi - \kappa_v I_v(s)$$

This describes how energy from a blackbody source enters a medium and travels within it. This transfer of energy is heavily dependent on both emissivity and opacity, properties of the medium. Emissivity is a property which describes how much radiation a medium will emit while opacity describes how much radiation a medium will absorb. Radiation intensity is the rate of energy passing through a unit surface area in a particular direction per unit solid angle per frequency interval. The variable s is the distance traveled by the radiation as described by

$$ds = dx \, / \cos \theta \, ,$$

ε_v is the emissivity of the medium, κ_v is the opacity of the medium, and v is the frequency of radiation in Hz. The distance x represents the perpendicular distance from the outside edge of the slab to a point within the slab. The angle θ is oriented so that an angle perpendicular to the edge of the slab would be 0 degrees and an angle parallel to the outside edge would be 90 degrees. My program solved this equation of transfer implicitly for a specified sample problem described by Fleck and Cummings.[3] The simulation took into account all propagation directions and a range of photon energies. A 4 cm thick slab is represented by 10 material zones of 0.4 cm thickness. In Ref. 3, a different hypothetical opacity profile is specified for each of several sample problems. For the sample problem used in this project, the radiation source is a blackbody spectrum of 1 keV temperature incident on one side of the slab, and the initial matter temperature was set to 1 eV. The opacity was defined by

$$\kappa_v = 27(1 - e^{-h v / kT}) / v^3 \, cm^{-1} \, ,$$

where hv and kT are energy in keV, the emissivity is described as

$$\varepsilon_v = 4 \pi B_v \kappa_v \, ,$$

where B_v is the Planck Function, and the material specific heat was set to

$$b = 0.5917 \, a \, T_o^3 \, ,$$

where T_o is the initial temperature and a is the radiation energy density constant, which is used as a centering parameter between explicit and implicit for the specific heat equation.

The program then ran a simulation in time steps of 0.02 nanoseconds. Several quantities were given as output, including the absorption and emission rates, the radiation energy density per zone and photon energy, and the temperature in each zone.[4] This output was saved in a data file, then graphed by a plotting program for analysis. By using a looping structure, the simulation was usually run between 40 and 100 time steps, or until equilibrium was met.[5] The results of these simulations were saved as a model for an accurate, but potentially time-consuming process. The technique of re-grouping was then applied in order to create fewer and broader groups that would potentially save computation time in a program such as DRACO or LILAC.

Re-grouping: Determining new energy groupings that accurately represent the photon energy spectrum at a specific time is crucial for maintaining an accurate simulation of radiation transport. My program determines where the important section of the spectrum is by keeping track of radiation energy density per matter zone and photon energy. The radiation energy density is then analyzed at a specific time, depending on when re-grouping is desired. From Fig. 1 it can be seen that at 0.26 nanoseconds the radiation energy density
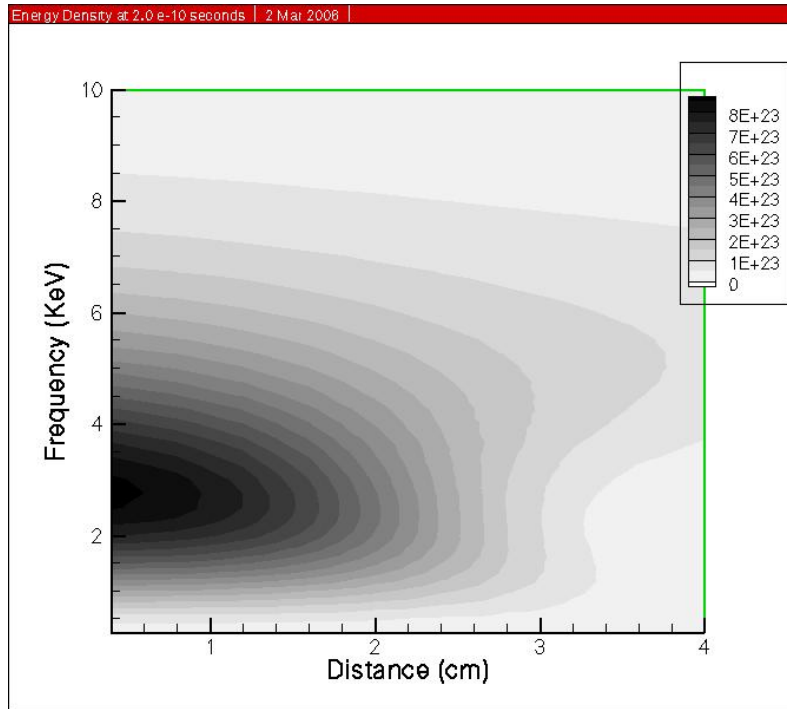
Fig 1: The Energy Density at 2.6 x 10^{-10} seconds as a function of distance into the slab.

is concentrated at roughly 2.5 keV. In order to divide the energy spectrum into a smaller number of groups, the program goes through a process to determine 5 new boundaries and subsequently 4 new groupings. First, the program finds the spectral density integrated over the whole slab, which gives a good representation of where the energy density is the highest. The program then finds the corresponding hν value at this peak energy density and uses this value as the middle boundary of four new energy groups. The program also determines the mean hν value between the peak energy density and the highest hν value of the spectrum, as well as the mean hν value between the peak energy and lowest hν value of the spectrum. These become two other boundaries of the four new energy groupings. For the last two boundaries of the new groupings, the highest and lowest hν values of the spectrum are used in order to maintain the total range of photon energy. The end result is 4 large groupings where there were once 40 fine groupings.

Results: The program was set up to re-group the photon energies from 40 groups to 4 at a simulation time of 0.3 nanoseconds. It ran in time steps of 0.02 nanoseconds, which was small enough to avoid oscillation in the results. By running the simulation with and without the re-grouping method, and then graphing the temperature of all zones, one can

5

see the results of re-grouping. At 0.1 ns after re-grouping (Fig. 2), the temperatures with and without re-grouping are very similar. However, at 0.4 ns after re-grouping (Fig. 3), the temperatures with and without grouping differ by a larger margin.
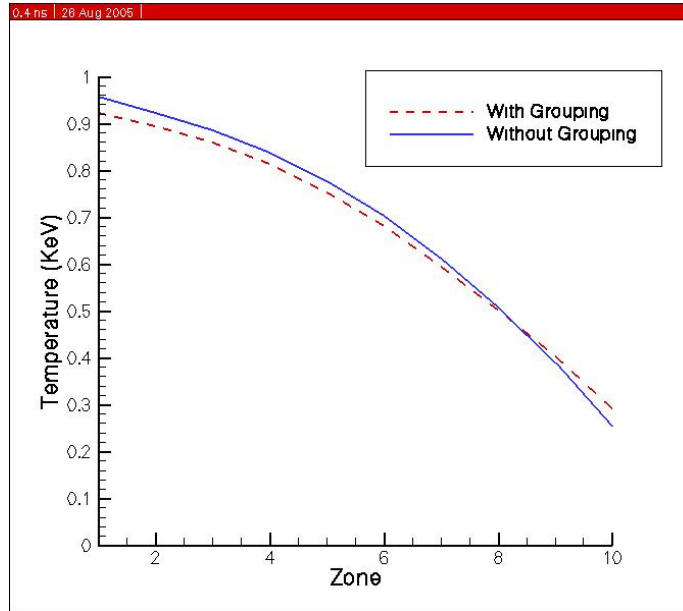

Fig. 2: Temperature profile 0.1 nanoseconds after re-grouping.
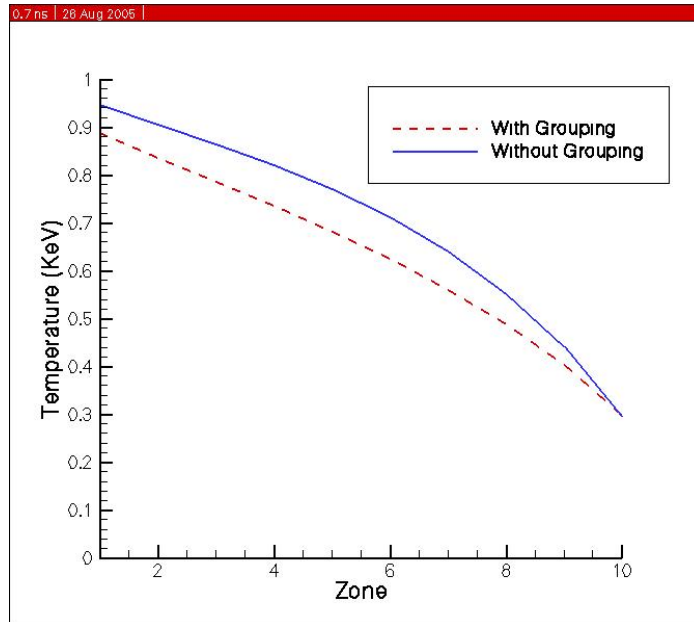

Fig. 3: Temperature profile 0.4 nanoseconds after re-grouping.

It can be seen from these graphs of temperature that as time increases after the re-grouping, the accuracy of the simulation decreases. By following the temperature of specific zones of the material over time (see Fig. 4), this correlation is easily seen. Zones 5 and 7 were chosen as representative zones in the simulation because of their deviation seen in Figure 3. The largest deviation between the temperatures with and without re-grouping appears in zone 5, making it a good illustration of the worst-case scenario. Zone 7 is very similar to the other zones, making it a good illustration of a normal deviation. There is a direct relationship between time and deviation between the simulations with and without energy re-grouping. As time increases, the accuracy of the simulation using fewer energy groupings decreases.
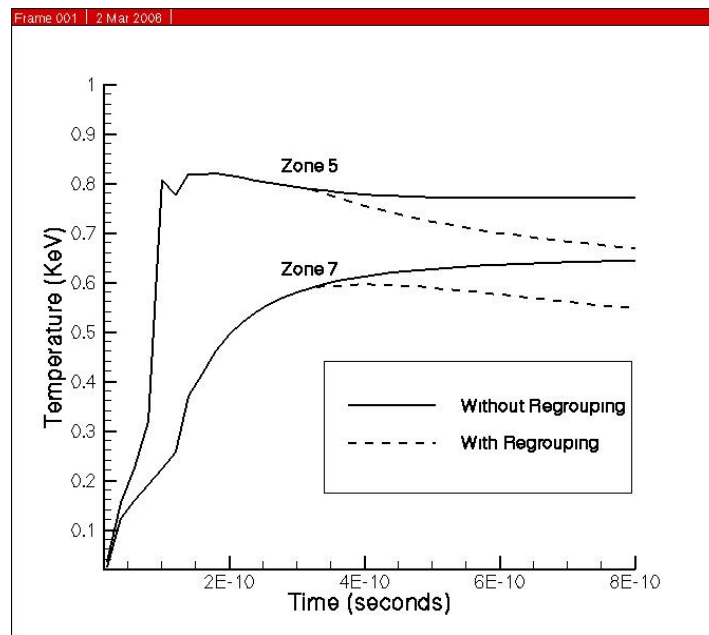

Fig. 4: Time dependence of the temperatures of zones 5 and 7 with and without re-grouping.

Conclusions: By looking at the results from the first test case used with this program, the process of re-grouping is very promising. The spectral resolution was reduced to 10% of its original groupings, yet the simulation remained fairly accurate. After 0.5 nanoseconds, the simulation with re-grouping remained within 15% of the simulation without re-grouping in the fifth and seventh zones of the material (see Fig. 4). Within the initial 0.5 nanoseconds after re-grouping occurs, the fifth zone is seen from Fig. 3 to be

one of the least accurate sections of the material. This means that other zones of the material would probably show better results than 15% agreement within the first 0.5 nanoseconds after re-grouping. While 15% accuracy may not be a desirable accuracy for all purposes, it still gives the user of the program a good idea of the temperature of the material. This result is encouraging considering a 10-fold spectral resolution decrease, which is dramatic. Altering the spectral resolution by a smaller amount would certainly give better results. It could be left to the user of the program to determine how accurate the results need to be. If only a mediocre estimate of the temperature is desired in a small amount of time, a large decrease in spectral resolution could be used. If a very good estimate is desired in less time than is required currently without dynamic re-grouping, a smaller decrease in spectral resolution could be utilized.

Future Work: The most useful conclusion drawn from running the program with photon energy re-grouping is that the accuracy, understandably, decreases by a small amount over time. In the first attempt at re-grouping, there was roughly 85% accuracy in the first 0.5 nanoseconds after re-grouping in one of the least accurate zones. This was accomplished with a ten-fold reduction in spectral resolution, however, which is a relatively large decrease. A decrease in accuracy comes as no surprise. It would be useful to determine the accuracy of re-grouping with a less dramatic decrease in spectral resolution, such as a 1/2 decrease. The results could potentially be much better than the 15% accuracy achieved currently 0.5 nanoseconds after re-grouping.

In a fully realized re-grouping strategy, the code would pick new groupings multiple times after pre-determined intervals instead of just once. This would be accomplished by running one time step with the original fine groupings for all re-groupings after the first for the purpose of re-adjusting the groups according to the energy density. The program could re-evaluate the energy density in this one time step, since it shifts over time, and pick new groupings depending on how the spectrum shifted. This method would be more accurate than the previous method of re-grouping because of how the spectrum shifts over time. This could be especially important in simulations where conditions change drastically, such as a more realistic laser-plasma interaction using data from the Laboratory for Laser Energetics. Eventually, the large groupings chosen for

cooler temperatures fail to accurately represent the photon energy spectrum of hotter material, so shifting the groups accordingly is desired when the material goes from one extreme of temperature to another.[1] The simulation would then run with the large groupings for another pre-determined length of time before re-grouping again. The length of time between re-groupings would have a large effect on simulation accuracy, so that would be adjusted as part of the re-grouping strategy. This method of dynamically re-grouping would slow down the speed of the program only slightly, but could be well worth it if the accuracy of the results improves because of it.

With all of these ideas, as well as the original method of re-grouping, it would be worthwhile to investigate a wider range of test cases in order to see the effects of re-grouping on a variety of situations. Different values of radiation temperature, emissivity, opacity and other values could be tested, which would give greater insight into the usefulness and reliability of this dynamic re-grouping method. There are several other test cases in Ref. 3 that could be utilized. If it is determined that the loss of accuracy is worth the time saved in the simulations, dynamic multi-grouping could then be implemented into simulation programs at the Laboratory for Laser Energetics.

References:

[1] R. Epstein, "private communication." Jul-Aug. 2005.

[2] Lloyd Motz and Anneta Duveen, *Essentials of Astronomy,* New York: Columbia University Press, 1966.

[3] J. A. Fleck, Jr. and J. D. Cummings, "An implicit Monte Carlo scheme for calculating time and frequency dependent nonlinear radiation transport," *Journal of Computational Physics*, vol. 8, pp. 313–342, 1971.

[4] Daniel D. McCracken, *FORTRAN With Engineering Applications,* New York: John Wiley & Sons, Inc. 1967.

[5] Daniel D. McCracken, *A Guide to FORTRAN IV Programming,* New York: John Wiley & Sons, Inc. 1972.

Micromechanics and Microstructure of WC Hard Metals

Karyn Muir

Honeoye Falls – Lima High School

Advisor: Professor John Lambropoulos

University of Rochester-Laboratory for Laser Energetics,

250 E. River Rd., Rochester NY 14623-1299

Abstract

Tungsten Carbide (WC), a composite material that contains ceramic grains of tungsten carbide within a binder of nickel or cobalt, combines the qualities of both metals and ceramics allowing it to be very strong. Several properties of these types of materials are typically measured, such as Young's modulus of elasticity (E), hardness (H) (Rockwell HRA or Vickers Hv), and fracture toughness (K_c). Both Young's modulus and hardness are relatively easy to measure but, because WC is so strong, K_c is difficult to measure. Therefore, it would be convenient to be able to estimate the fracture toughness of a material as a function of its hardness and modulus of elasticity. This project addresses the estimation of fracture toughness, the inverse determination of binder content (binder mass %), and the microstructure of WC composites. Two micromechanical models were used that allow the estimation of K_c based on the easily measurable properties E and H. The Laugier model proved to apply fairly well with some of the WC fracture data, though not all of the data. The model parameters were then optimized, and the correlation improved. The model created as part of this project apparently applies better for two published sets of fracture toughness data. The two models were then applied to the fracture toughness of novel non-magnetic WC samples (with Ni binder.) We have also developed a mass density model that allows the calculation of the density of WC as a function of the densities of the components (WC and binder) and the mass percent of the binder. Inversely, the model can predict the binder mass percent given the density of the WC composite. Parallel work addressed the measurement of important microstructural features of WC. In order to better understand these, five different samples including Fujilloy M10 and M45, Basic Carbide BC 12N, Kennametal K80, and Cerbide (a binderless WC) were analyzed. Surface roughness measurements were taken using the Zygo interferometer, optical images were taken using the Leica microscope, and SEM micrographs were taken in order to assess the grain structure, allowing the measurement of grain size, contiguity, and binder mean free path.

1. Introduction

Tungsten Carbide, or WC, is a compound that consists of hard grains of the ceramic Tungsten Carbide embedded in a sea of soft metal, which is usually Nickel or Cobalt (Figure 1), with Cobalt being the most common binder (Figure 1). This combination of substances allows WC to have qualities of both metals and ceramics, which is advantageous because the resulting substance is more resistant to fracture (stronger) than most ceramics and more resistant to permanent deformation (harder) than most metals. The unique characteristics of Tungsten Carbides that make them so desirable are the facts that they have a greater stiffness, hardness and higher density than steel, a greater compressive strength than most other engineering materials, and tensile strength comparable to alloy steels. [Budinski and Budinski, 1999]
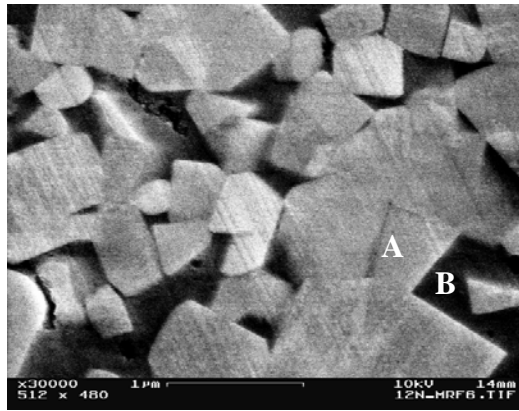
Figure 1: - An SEM micrograph of a sample of BC 12N. Tungsten Carbide consists of hard grains of Tungsten Carbide (A) surrounded by a sea of soft metal, which is usually Ni or Co. (B)

Commonly, WC is made by compaction, where Tungsten powder is milled with the binder to reduce the carbide particle size. Then a sintering process is used to melt and combine the materials. As a result of this process, the ceramic grains make the composite WC extremely hard, but instead of being brittle like other ceramics, the softer metal strongly holds the composite together. Other qualities include negligible porosity, and high hardness and compressive strength. This all results in excellent resistance to low stress abrasive wear, and among its many uses, WC has been used in precision molds for optics.

In order to best use WC, the understanding of the machinability of both magnetic and non-magnetic versions of this compound is necessary. To understand the machinability, the characteristics of Tungsten Carbide must be understood, such as density, binder and grain mass percent, hardness (Vickers and Rockwell A), Young's modulus (E), energy release rate (G_c), and fracture toughness (K_c). The microstructural features should be analyzed as well.

2. Terminology

To describe and measure the microstructure and mechanical properties of WC composites, several terms must be introduced.

- ❖ Density is the mass of a substance divided by the volume of a substance (Units kg/m^3).
- ❖ Mass percent is the mass of a component (usually the binder) divided by the total mass of the composite. For the purposes of this project it is either the mass of the binder or the grains, divided by the sum of the masses of the binder and the grains.
- ❖ Hardness can be measured in several ways, and in this project Vickers and Rockwell A hardness tests were used. The Rockwell A scale is dimensionless, but Vickers hardness uses units of GPa. To measure the hardness, both tests use the indentation method, where a diamond indenter is pushed into a material with a given force, and the resulting indent, or footprint "size" is used to determine the hardness. Though the process is the same for both tests, the differences are in the force extended on the indenter, and the size of the indenter. Vickers tests use a square pyramidal indenter with a 1g to 2000g

force, while Rockwell A tests use a spherical intenter with a 50kg force. The values obtained by these two tests are usually not comparable. [Callister, 1994]

❖ Young's modulus, or E, is the ratio of stress to strain of a given substance for small (or recoverable) amounts of strain. This value is used to give its elastic stiffness, and is measured in GPa. It is usually the elastic modulus for tension. To measure this value, uniaxial forces are applied to an elongated sample. The cross sectional areas of the sections on which the forces are applied are measured, as well as the gauge length between these areas. Then the stress, or the force divided by the area, is plotted versus the strain, or the change in length divided by the original length. This will produce a straight line (for small strains), and the slope of this line is Young's Modulus (Figure 2).

Figure 2: - A diagram of how Young's Modulus, or E, is measured.
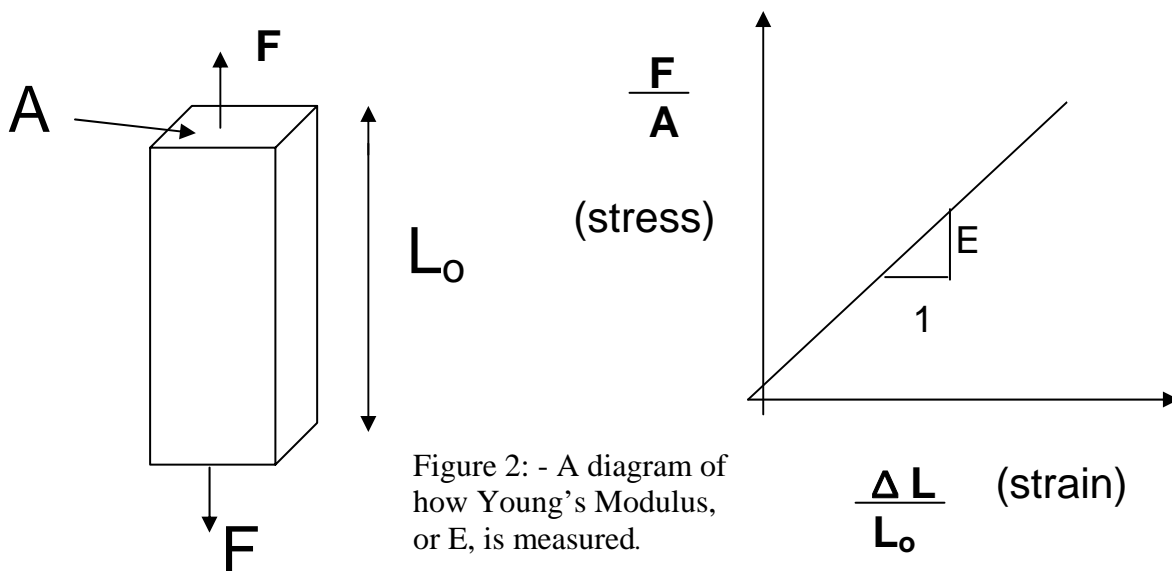
❖ Fracture Toughness, or K_c, is the most important material parameter used in fracture mechanics. [Callister, 1994]. Measured in $MPa*m^{1/2}$, it is most commonly used for failure analysis. To measure K_c, a crack is introduced in a sample and the system is loaded to propagate the crack. The tougher the sample is, the smaller the crack growth will be and the higher the K_c (Figure 3).
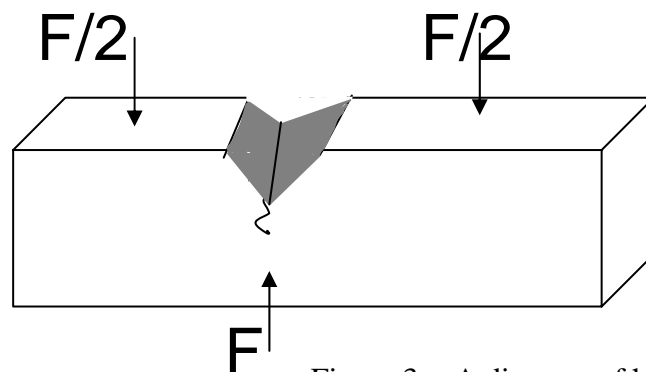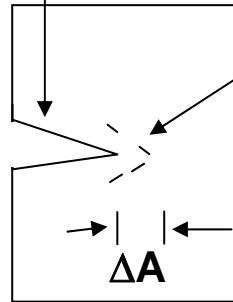
Figure 3: - A diagram of how to measure Fracture Toughness, or K_c.

❖ The Energy Release Rate, or G_c, is defined as $G_c = K_c^2/E$ (units of J/m^2). It provides the amount of total energy that must be expended to produce a unit increase in the crack surface area. (Figure 4).

Energy E

Energy E- ΔE

ΔA

$$G = \frac{\Delta E}{\Delta A} \quad (J/m2)$$

Figure 4: - A diagram of
how the energy release rate,
or G_c is measured.

❖ Mean binder free path is the distance between grains in a sample.

❖ Contiguity is the percentage of grains touching in a sample.

3. Mass Density Model

One of the initial steps in this project was to find a way to correlate the mass density and binder mass content of WC. In the mass density model I created, I used the separate densities of the binder, or "soft" phase, and the WC, or "hard" phase, along with the mass percent (%) of the binder. The mass density model leads to

$$\rho = \frac{\rho_1 * \rho_2}{\rho_1 + M\rho_2 - M\rho_1}$$

where $\qquad \rho_1 = \frac{m_1}{v_1} \qquad \rho_2 = \frac{m_2}{v_2} \qquad \rho = \frac{m_1 + m_2}{v_1 + v_2} \qquad$ and $\qquad M = \frac{m_1}{m_1 + m_2}$

with 1 being the binder (softer phase) and 2 being the WC (harder phase). The model has the advantages of not depending on phase shape, size or contiguity. Not only can it be used to predict M for given ρ, but it can also be used inversely to predict ρ for given M. A plot of the mass density model is shown in Figure 5.

Mass Density Model (LLE, 2005)

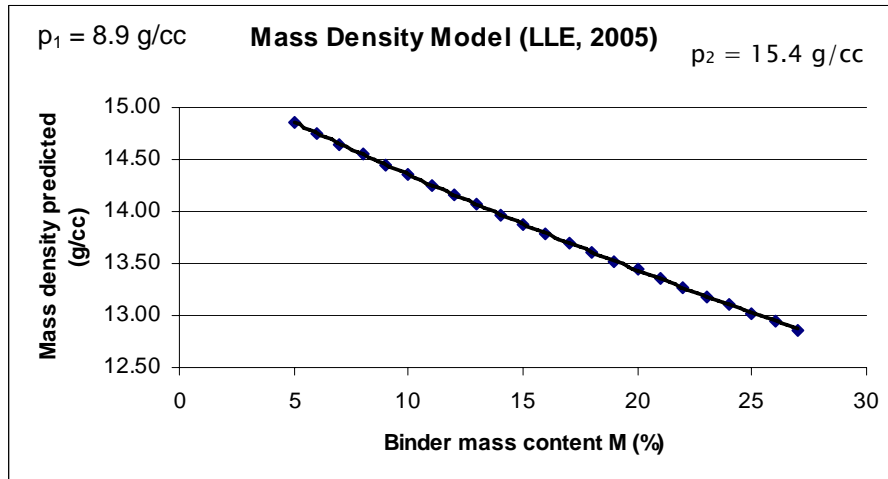$p_1 = 8.9$ g/cc $p_2 = 15.4$ g/cc

Figure 5: - A graph of the mass density
model, showing the mass density
predicted vs. binder mass content (%).
This graph can be used to also predict
binder mass content (%).

To test this model, two sets of data provided by companies that produce WC were used.
Using this data, the densities given by the company were plotted versus the densities that
were estimated using the mass density model. The first set of data was from Kennametal
[1]. The results shown on the graph in Figure 6 below show that the predicted and actual
densities are very close.

Kennametal Density Data, LLE Model (2005)

$y = 0.8601x + 1.9562$
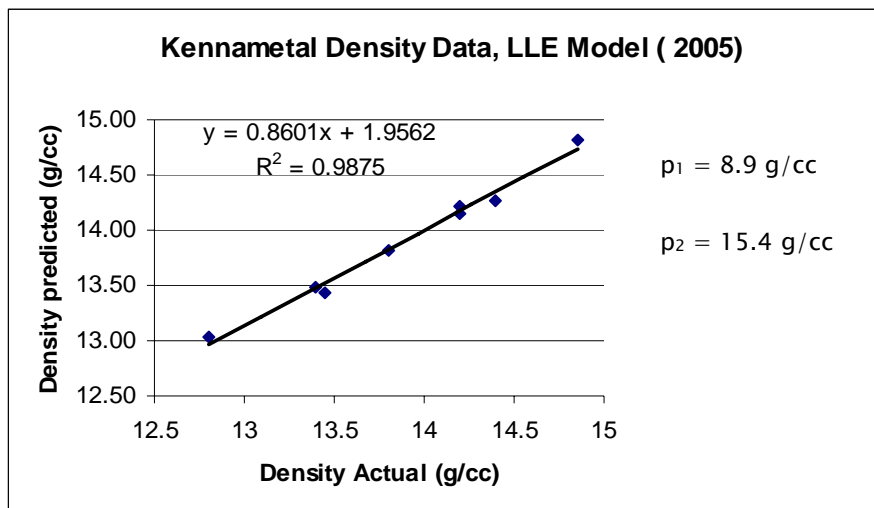$R^2 = 0.9875$

$p_1 = 8.9$ g/cc

$p_2 = 15.4$ g/cc

Figure 6: - A graph of the Kennametal
density data [1] showing the actual
density vs. the predicted density.

The second set of data is published by Basic Carbide [2]. The graph in Figure 7 shows even better agreement than the Kennametal data, verifying that the Mass Density Model is quite reliable.

Basic Carbide Density Data, LLE model (2005)
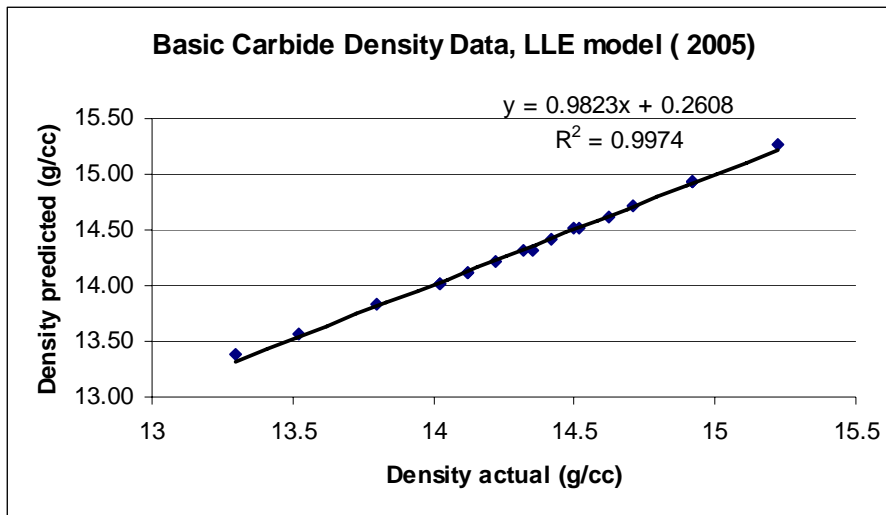
$y = 0.9823x + 0.2608$

$R^2 = 0.9974$

Figure 7: - A graph of the Basic Carbide density data [2] showing the actual density vs. the predicted density.

The results of the estimations of mass percent are shown in the chart below. The chart shows the mass densities of six different samples of Tungsten Carbide as well as their predicted binder mass percents. For the sample K801 where the actual binder mass percent was known, this is shown as well. The agreement for K801 between the published and predicted value is remarkable. This leads us to expect that the predicted values for the other samples are fairly close to their actual values as well. We conclude that this model is a reliable way to estimate the binder mass percent of samples of Tungsten Carbide when this microstructural feature is not given.

	Mass density (g/cc)	Binder Mass % predicted	Binder Mass % actual
Fuji M10	14.25	12.21	?
M45	14.4	10.69	?
M50	14.1	13.77	?
M70	13.8	16.98	?
Basic Carbide BC 12N	14.35	11.2	12
Kennametal K801	14.85	6.31	6.3

Figure 8: A chart showing the results of the binder mass percent prediction model.

4. Fracture Toughness Model

The next task was to look at fracture toughness, or K_c, models. As previously discussed, K_c is a very difficult property of WC to measure, due to the extreme strength of the material. Therefore, research has tried to create models that estimate K_c using other characteristics of WC that can more easily be measured.

The model I looked at was created by Laugier (1986). Laugier's correlation is:

$$K_c = 2.15 * 10^6 \left(\frac{E}{H} \right)^{0.6} \left[1 + 0.012 \left(\frac{E}{H} \right) \right]^{-0.6} \left(\frac{1}{H^{1.5}} \right)$$

where E and H are in units of MPa, and the resulting K_c is in units of MPa*m$^{1/2}$.

We tested the Laugier model using data from Kennametal [1] and Bhaghat [1999]. Both the Kennametal data and Bhaghat data give measured values of K_c, so I was able to plot the known (measured) data versus the estimated data using Laugier's model. After initially plotting this data, the plots showed a good correlation between the estimated and actual K_c of the samples. I then worked on optimizing the first numerical term ($2.15 * 10^6$) of Laugier's model to attempt to obtain the best possible correlation using the data we had. The optimal numerical coefficient turned out to be $2.05 * 10^6$. The results after optimizing this first term, or "A", are shown below in Figures 9 and 10.
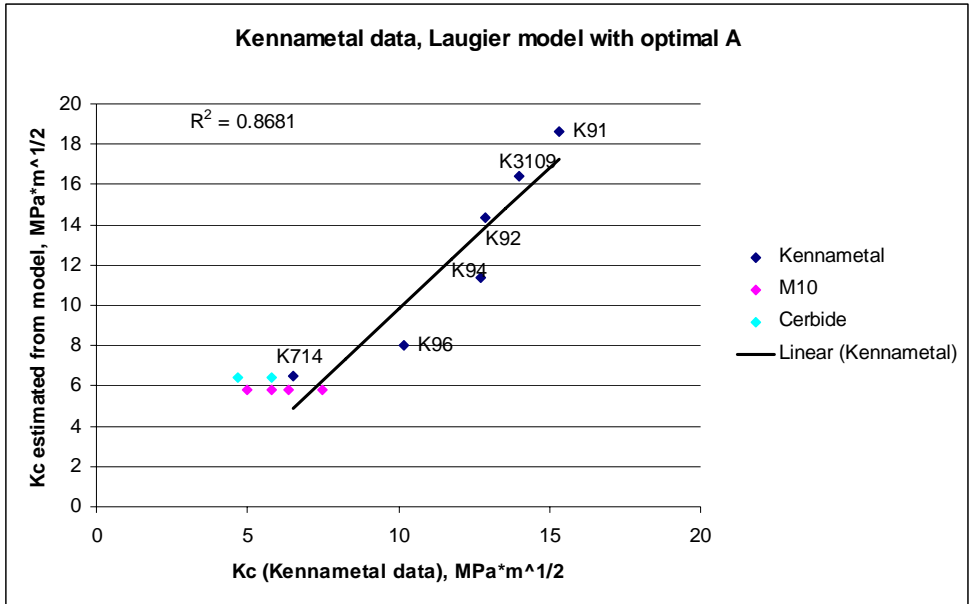
Figure 9: - A graph of the Kennametal data [1] when applied to the Laugier model with the optimal A, with FujiM10 and Cerbide in comparison as well.
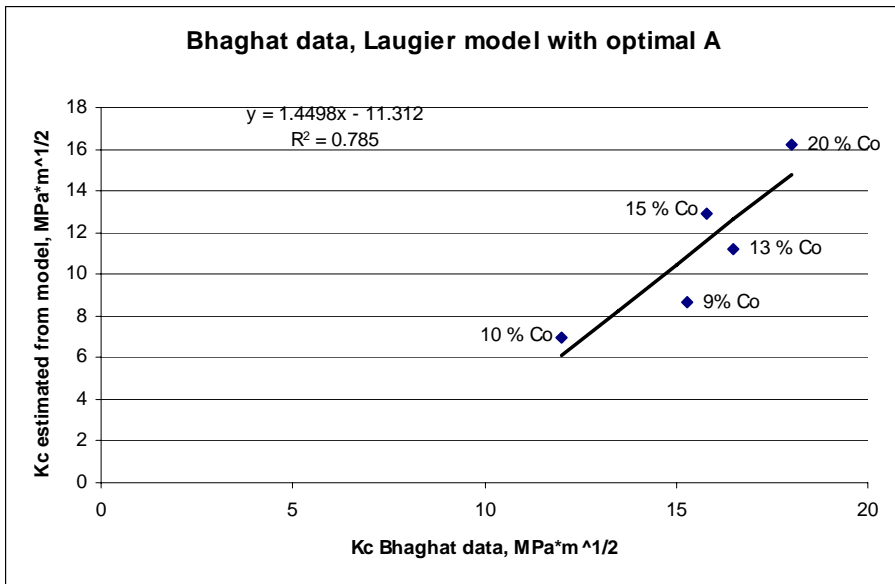

Figure 10: - A graph of the Bhaghat data [1999] when applied to the Laugier model with the optimal A.

These plots show that there is a fairly good correlation between actual and estimated K_c values using the Laugier model with optimal A, but there is definitely room for improvement.

More recent work on this topic is the energy release rate model, which was created at the LLE in summer 2005. In this model, G_c is a function of Vickers hardness, or Hv. It has been discovered that if G_c is plotted versus Hv for several WC samples, the points almost form a line, showing excellent correlation. This has the potential to be extremely useful, because if the Hv of a sample is known, then by using a graph of this correlation the K_c of a sample can be estimated if the Young's modulus is known. This is a relatively easy calculation. The plots of both the Kennametal data and the Bhaghat data energy release rate models are shown below in Figures 11 and 12.
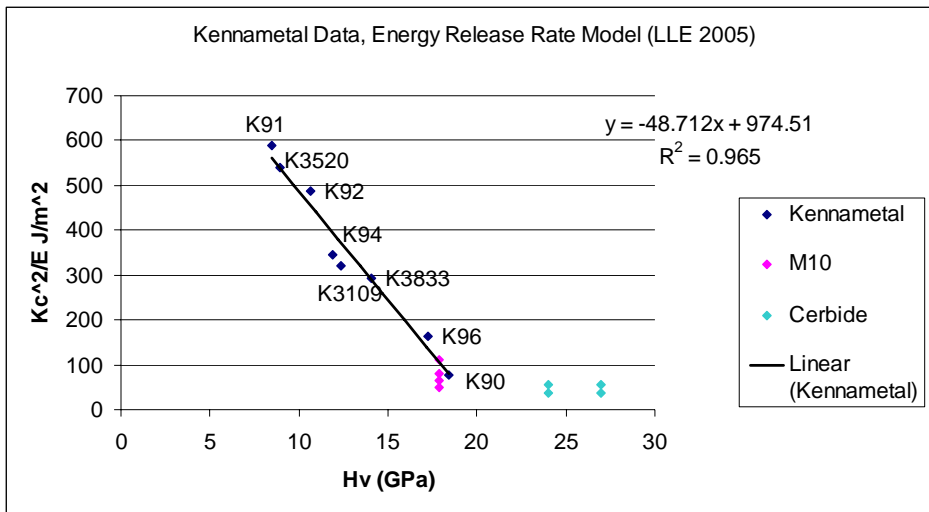

Figure 11: - A graph of the Kennametal Data when applied to the energy release rate model, with Fuji M10 [3] and Cerbide [4] for comparison.
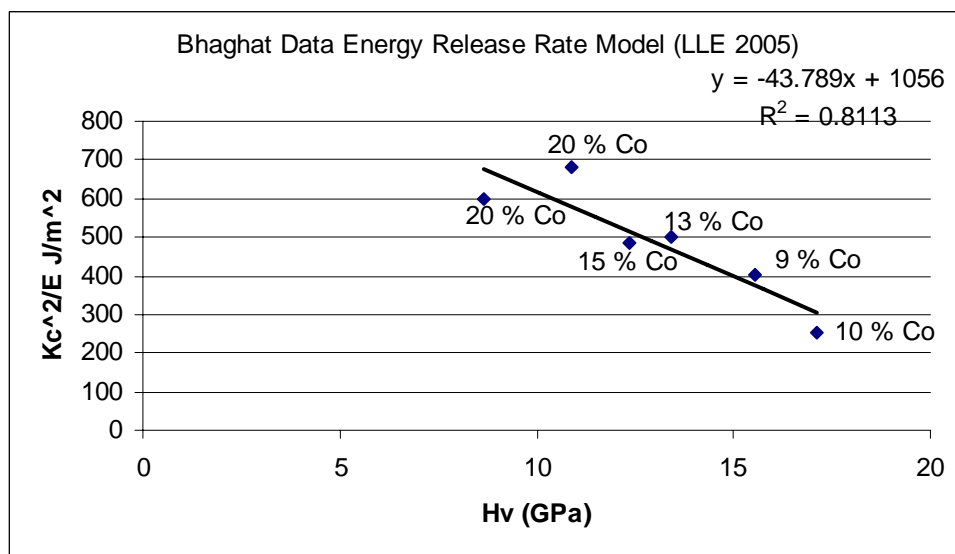

Figure 12: - A graph of the Bhaghat Data when applied to the energy release rate model.

Both of these plots show a much stronger correlation using the energy release rate model than with the Laugier model, even after optimizing the A.

To find the K_c of a sample using one of these graphs is simple. All that one would need to know would be the Vickers hardness (Hv) and the Young's modulus (E). For example, using either of the graphs, once the Hv was known, the G_c value could be found by looking at the point on the line corresponding to the given Hv. Because G_c is simply K_c^2/E, this can be solved for $K_c = (G_c * E)^{1/2}$. Some of the results of the estimated K_c values are shown in the chart in Figure 13, as well as the measured values when available.

	K_c Measured	K_c Predicted Laugier Model	K_c Predicted LLE model
Fuji M10	**6.4-6.7**	**5.8**	**7.21**
M45	**?**	**9.15**	**10.76**
Basic Carbide BC 12N	**?**	**12.63**	**15.27**
Kennametal K801	**?**	**10.27**	**10.76**
Cerbide	**5.8-6.4**	**3.2**	***negative**

Figure 13: - a chart of the fracture toughness vs. E and H results.

5. Microstructural Features

While examining various ways to estimate the K_c value of Tungsten Carbide, research was also done to investigate the microstructural features of WC. The density (ρ), mean grain size ($\bar{d}$), binder mean free path (λ), contiguity (C), binder mass fraction (M), and binder volume fraction (CV) were determined in a variety of samples. Density is measured in g/cm^3, mean grain size and mean binder free path are in μm, and contiguity, mass fraction of binder, and volume fraction of binder are dimensionless.

When measuring the mean grain size as well as the other microstructural factors, the mean linear intercept method was used. To use this method, an SEM micrograph of a sample of Tungsten Carbide was taken. On a copy of this picture I drew twenty lines horizontally and twenty lines vertically. I then used these lines to estimate the mean grain size by measuring the size of the grains that each line crosses and then averaging these values.

To calculate contiguity I focused on the number of grains touching versus the number of grains not touching each drawn line. The number of touching grain borders is multiplied by two, and then divided by the sum of this number and the number of non-touching grain borders. This number is given as a fraction between 0 and 1.

The volume fraction of the binder is the volume of the binder divided by the total volume of the substance. The mass fraction of the binder is the mass of the binder divided by the total mass of the substance. To obtain these values, information about the mass and densities of samples and the materials that make up these samples is used. This information is easily available and does not need to be calculated, and obviously the mean linear intercept method is not used to measure these aspects of WC.

To measure the binder mean free path of Tungsten Carbide, the mean grain size, the volume fraction of binder, and the contiguity of the sample must be known. These values are then used in the equation:

$$\lambda = \overline{d}\left(\frac{V_B}{(1-V_B)(1-C)}\right)$$

where V_B is the volume fraction of binder, C is contiguity, and $\overline{d}$ is mean grain size. The mean grain size $\overline{d}$ and contiguity C are measured by the linear intercept method. The volume fraction of binder is found from the binder mass fraction.
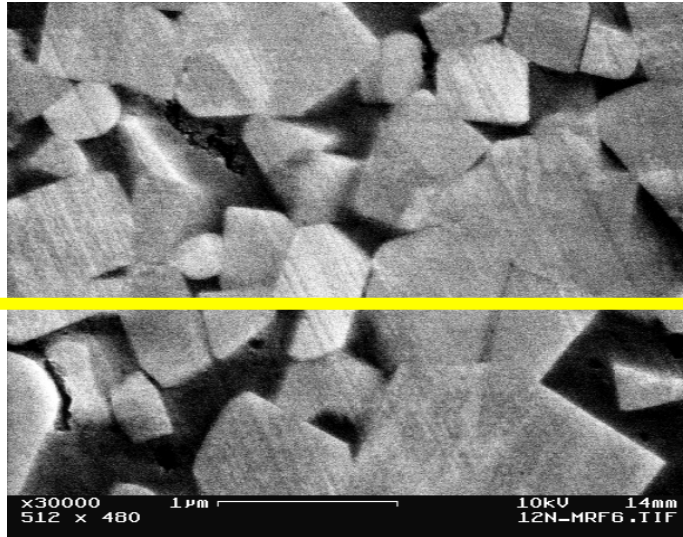

Figure 14: - An example of a SEM Micrograph with a line drawn, used for the linear intercept method to determine mean grain size, continuity, and binder mean free path.

All of these methods were used to analyze the microstructure of a variety of samples. The samples included Fuji M10, M45, M50, and M70, Basic Carbide's BC 12N, Kennametal's K801, and the Cerbide which is a binderless Tungsten Carbide. The results of this microstructure analysis appear in the chart in Figure 15.

	Grain Size (µm)	Contiguity	Binder Mean Free Path (µm)	M (%)	Cv (%)
M10	0.24± 0.17 Range 0.04-0.84	0.38	0.09	11.84	19.56
M45	0.495± 0.17 Range 0.1-1.5	0.38	0.24	10.31	17.3
BC 12N	0.488± 0.261 Range 0.06-1.2	0.26	0.15	12	21.81
K801	1.2± 0.22 Range 0.06-3.4	0.56± 0.013	0.34	TBD	TBD
Cerbide	0.38± 0.18 Range 0.12-0.89	———	———	———	———

Figure 15: - Chart showing the microstructure of several samples. M is binder mass percent, and Cv is binder volume percent.

Because the Cerbide does not have a binder, there are no values entered for its microstructure other than the grain size. The investigation of the microstructural features of Tungsten Carbide may be used to correlate microstructure and other factors such as K_c.

6. Conclusions

Through the investigation of various characteristics of WC I have created a density model that correlates mass density and binder mass content, optimized and created equations that estimate K_c, and analyzed the microstructural properties of a diverse set of WC samples.

The density model can be used not only for density, but also inversely to estimate the binder mass content of a sample as well. It is advantageous because it does not rely on phase shape, size or contiguity, which allows a much easier and more applicable way to estimate density and binder mass content of WC.

By optimizing the Laugier model, which uses Young's modulus and hardness to estimate fracture toughness, we have a more accurate estimator of K_c values of Tungsten Carbide. Through the energy release rate model another step has been taken to better estimate the K_c of WC. The values found through this model are more accurate than through Laugier's model, even after optimization.

Analyzing the microstructural characteristics of WC helps to better identify the features that may correlate to factors such as strength and durability of WC. All of these observations will prove useful as WC is used in more technical applications.

In the future, more work can be done to better understand the qualities of WC. To accomplish this, more microstructure and SEM images will be needed of more samples, as well as more known K_c data. Improved models for K_c and G_c will also help improve understanding of any correlations between properties. It would also be beneficial to have physics based models to help determine how microstructure may affect processing performance, such as with grinding and polishing. Improved knowledge of Tungsten Carbide will continue to be needed in order to understand how to best use this impressive material.

7. References

Basic Carbide Corporation, 900 Main Street, P.O. Box 228, Lowber, PA 15660, USA.

Cerbide, Inc., 5720 Ellis Road, Orchard Park, NY 14127, USA. Materials tested were commercially available on January 2005.

Fuji Die, 2-17-10 Shimomaruko, OTA-ku, Tokyo, Japan.

Kennametal Inc., Cambridge Beltway Park, 8910 Lenox Point Drive – Suite F, Charlotte, NC, 28273, USA.

K. G. Budinski and M. K. Budinski, Engineering Materials, Properties and Selection, Chapters 1, 2, 6, 6th edition (Prentice Hall, Columbus, Ohio, 1999).

M. T. Laugier, "Comparison of toughness in WC-Co determined by a compact tensile technique with model predictions," Journal of Materials Science Letters **6**, 779-780 (1987).

R. B. Bhagat, J.C. Conway, M.F. Amateau, and R. A. Brezler, Tribological performance of WC-based cermets and development of a fracture mechanics wear model, Wear 201, 233-243 (1996).

W.D. Callister, Jr., Materials Science and Engineering – an Introduction, 3rd edition, chapters 6 and 8 (Wiley, New York, 1994).

Improving the Illumination Uniformity of a Cryogenic Target with a Layering Sphere

Brian Way Pan
Penfield High School
Penfield, NY 14526

Advisor: Dr. Wolf Seka
Laboratory for Laser Energetics
University of Rochester
250 East River Road
Rochester, NY 14623

August 24, 2005*

Abstract

One of the considerations in creating a precisely layered cryogenic target requires uniform heating due to uniform illumination of the target by an infrared (IR) laser shined within the layering sphere, which has an inner, gold-coated rough metal surface. The layering sphere was originally thought to have Lambertian scattering characteristics that result in uniform heating. However, measurements have shown that the surface scattering characteristics of the layering sphere are far from Lambertian. Using a periscope setup at the location of the cryogenic target at the center of the layering sphere, the illumination uniformity (or lack thereof) was evaluated. A wide-angle diffuser configuration placed at the input of the heating laser demonstrates a significant improvement of the illumination uniformity that closely resembles the illumination uniformity achieved in a perfect integrating sphere. Finally, the periscope results were analyzed to determine the effect of the keyhole and four viewing windows of the layering sphere on the illumination uniformity of the target.

1. Introduction

In the direct-drive inertial confinement fusion (ICF)[1] concept, a cryogenic spherical capsule containing thermonuclear fuel is imploded by 60 laser beams, which are directed on the surface of the capsule in a nearly uniform pattern. Much of the current ICF research uses the 60-beam, 30-kJ UV OMEGA laser system[2] at the Laboratory of Laser Energetics (LLE) of the University of Rochester. The research is performed to understand the requirements and determine the conditions for a high energy yield from fusion reactions so that ignition of deuterium-tritium fuel may be demonstrated at the National Ignition Facility (NIF) at Lawrence Livermore National Laboratory (LLNL) in the near future.

1.1 Cryogenic Target

The OMEGA cryogenic target design (Fig. 1) is a 0.9-mm spherical plastic shell with a 5-μm plastic shell (CH). This target is filled with D_2 at 1500 atm, cooled to cryogenic temperatures, and located at the center of a 2.5-cm diameter layering sphere[3] (Fig. 2b). This gas density equates to a frozen deuterium wall thickness of approximately 100 μm, thereby delivering a high concentration of fusion fuel.

1.2 Layering Sphere and Process

One of the processes for creating a deuterium solid layer starts with the target below the triple point (18.72 °K) and with a frozen lump of deuterium ice in the bottom of the target[3]. Deuterium is then layered by uniformly bathing and heating the target in infrared (IR) radiation. This process causes the deuterium ice to become warmer than the plastic shell's surface. The solid deuterium sublimes from where it is thickest and re-condenses where it is thinnest because the IR light (wavelength, $\lambda = 3.16\mu m^3$) is preferentially absorbed by the deuterium ice. With appropriate controls on the temperature of the layering sphere and the heating laser, the thickness

of the ice wall is expected to become uniform. In practice, however, the resulting ice layer is not uniform. Three-dimensional (3-D) characterization of the ice layer using optical shadowgraphy[3,4] has shown peak-to-valley variations of ≤ 20 μm (Fig. 2a) in the ice layer thickness.[3,5] The ice layer thickness variation and other layer imperfections[6] such as craters and cracks typically result in significant degradation of fusion yield in implosion experiments.

Currently, the layering sphere has obvious imperfections that may affect the IR illumination uniformity on the target. The inner surface of the layering sphere is roughened, gold-coated metal. In reflecting an incoming light beam off the inner surface and about the surface normal, a specular lobe in the specular direction is produced. The first and second reflections are more significant. Later, they will be referred to as "bright spots." Other imperfections of the layering sphere are due to the "windows" and "keyhole" (Fig. 2b). It is important to assess the effect of these unavoidable holes in the layering sphere for viewing target and target insertion.

1.3 Project Goal

It is important that LLE produces targets with uniform ice layer. A uniform cryogenically frozen deuterium ice layer within a 1-mm sized plastic capsule should be created inside a layering sphere. The layering sphere has provisions to inject a heating laser through an optical fiber that causes unevenly frozen deuterium to redeposit the D_2 ice uniformly. Uniform illumination of the target by the heating laser is expected to generate even deposition of deuterium all around the plastic capsule. The scattering characteristics of the heating laser light, within the layering sphere, were not known. So, the goal is to first determine the heating illumination uniformity (or lack thereof) at the center of the layering sphere. Then, comparing the uniformity of that sphere to the uniformity of a perfect integrating sphere, we were to analyze

root causes of non-uniform illumination. Finally, we wanted to propose a solution for creating more uniform heating illumination in the sphere to attain uniform D_2 targets.

The motivation for improving the scattering characteristics of the layering sphere is the possibility of generating more uniform targets, which could, in turn, lead to more effective target implosions and more net energy gain in the fusion reactions. Such improvements would also benefit other facilities such as NIF at LLNL.

2. Experimental

To establish the illumination pattern of the center of the layering sphere and to compare it with the illumination pattern within a perfect integrating sphere, an apparatus, as shown in Fig. 3, was set up using a visible light emitting diode (LED) around 630 nm to replace the IR heating laser. This "periscope" would mimic what the cryogenic target experiences in one plane at a time. The periscope consisted of a 0.5 mm optical fiber with a small glass prism optically coupled to the end of the fiber; the periscope was then rotated within the layering sphere using a computer controlled motor. The optical fiber piped the light collected by the prism to a photodiode whose output was displayed on an oscilloscope and subsequently, on a computer.

Because reproducibility in a wide variety of setups was essential, computer-controlled rotation and data acquisition was implemented. Reproducibility of the data was assured by taking at least 3 scans for each experimental setup. Data were then displayed in either polar or rectangular coordinates as oscilloscope readings *versus* angle of rotation (motor position).

Illumination uniformity data were acquired for equatorial views of a perfect integrating sphere and an actual layering sphere, along with a tilted-plane view of the layering sphere. The equatorial views included views of the windows (partial views in some cases). The tilted-plane

view included a significant part of the keyhole area. Then, equatorial and tilted-plane views of the proposed solution were taken.

3. Results and Discussion

The layering sphere is designed to work with the LLE's Cryogenic Target Handling System[7], so only absolutely necessary modifications to the sphere can be carried out. Additionally, it is important to note that the sphere's inner surface itself is roughened gold, which can tolerate the cold temperatures and high acceleration, which the surface, just prior to a laser fusion shot, is exposed to. The sphere also reflects the 3.16 μm heating IR laser better than most other surface treatments.

3.1 Current Illumination Uniformity Level

Using the periscope we can quantify the current illumination non-uniformity inside the layering sphere in two planes, the equatorial view and a tilted plane. We also compared these data with data collected from a "perfect" integrating sphere whose surface was a known Lambertian[9] scatterer.

Typical plots of equatorial scan data for the layering sphere are shown in Fig. 4 in which the scope readings (mV) were normalized to the maximum reading and plotted *vs.* angle of periscope rotation (degree). Figure 4a is a polar plot of the data while Fig. 4b is the equivalent Cartesian plot. The polar plot depicts the angular non-uniformities in a more qualitative way while the Cartesian plot is more convenient for quantitative interpretation.

The layering sphere with all windows closed shows two maxima and two minima in Fig. 4 (red curves). The intensity fluctuation between maximum and minimum is >2. Further observation of the data in Fig. 4 suggests that the maxima can be attributed to the first and

second bounces of the semi-specular reflections. These "bright spots," would be even brighter if the equatorial scan were to view the entire area of the first or second bounces.

3.2 Uniformity Goal: Lambertian Integrating Sphere

In order to establish an illumination standard for comparison with the data obtained from the layering sphere, an integrating sphere with "Lambertian" scattering[8] characteristics was investigated using the same periscope arrangement. The inner surface of the sphere is a white, powdery surface whose scattering characteristics were measured using a witness piece and was found to closely follow the Lambert's cosine law (Fig. 5).

Plots of equatorial scan data for the perfect integrating sphere are shown in blue curves in Fig. 4. The illumination uniformity at the center of this sphere was significantly better than the results obtained from the layering sphere. There are no noticeable bright spots and the overall fluctuations in trace do not exceed ±10%. It should be noted that integrating spheres are usually used as uniform sources for light exiting through a small hole in the sphere. Uniformity of illumination at the center of the integrating sphere is a non-standard application that does not necessarily lead to perfect uniformity. Thus this experiment by itself demonstrated an important point, i.e. that a good integrating sphere indeed leads to quite tolerable illumination uniformity at the center of the sphere.

3.3 Scattering Characteristics of the Inner Layering Sphere Surface

Figure 4 clearly demonstrates the difference in the illumination uniformity between the layering sphere and the perfect Lambertian integrating sphere. This difference mainly results from the non-Lambertian, semi-specular characteristics of the inner surface of the layering sphere. The detailed scattering characteristics of the inner surface of the layering sphere have been measured separately and are shown in Fig.5.

The scattering characteristics of a gold-coated rough metal witness plate, which is similar to that of the inner surface of the layering sphere, was determined by M. Alexander et al.[9] The reflected intensity was measured as a function of detection angle by shining an incident laser beam at 135° incident angle. The measured reflected intensity was normalized to the maximum intensity value and plotted as a function of viewing angle (red triangles) in Fig. 5. The normalized reflected intensity distribution was also calculated[4] using the equation (1) and displayed (red dash curve) in Fig. 5:

$$R = k\, R_L \cos^n(\theta-\theta_0) \qquad\qquad (1)$$

In this equation, θ = viewing angle, θ_0 = specular reflection angle (=45°), n=9 (best fit the data[4)], k is the normalization constant such that maximum R is equal to 1, and R_L in equation (1) is the Lambertian intensity distribution[8]:

$$R_L = \cos(90^\circ - \theta) \qqquad\qquad (2)$$

This is also shown (green solid curve) in Fig. 5. The measured results (green squares) are in agreement with the Lambert's cosine law. The data in Fig.5 point out the non-ideal scattering properties of the gold-coated rough surface of the layering sphere as one of the root causes to the non-uniform illumination problem.

3.4 Uniformity Improvement by a Wide-Angle Diffuser Configuration

There are two obvious solutions to increase the illumination uniformity of the layering sphere at its center: (1) placing diffusers into the laser beam that spread the area of the first bounce, and (2) making the surface Lambertian-like. Solution 2 is difficult to implement because of absorption problems in the 3-μm wavelength range, the cold temperatures and the high acceleration (5 to 7g) that the sphere experiences just prior to the laser shot. Solution 1 was therefore pursued further.

The layering sphere was insignificantly modified to incorporate the use of a very small, eighty-degree wide-angle diffuser, as shown schematically in Fig. 6. The diffuser is an "engineered" diffuser that scatters the light in the forward direction into an 80-degree cone with over 90% efficiency. The diffuser was mounted such that its plane went "through" the center of the target and thus minimized any light scattered directly by the diffuser from reaching the target. Any other arrangements appear to lead to less desirable illumination uniformities at the center of the sphere.

Direct illumination of the target by the diffuser was further minimized by placing another small diffuser on top of the primary diffuser as shown in Fig. 6. The first bounce area on the layering sphere was thus significantly enlarged and the illumination non-uniformity at the center of the sphere was significantly improved and approached that of the perfect integrating sphere.

Equatorial scans of the modified layering sphere are shown in red curves (dash) in Fig. 7 along with corresponding data obtained with the unmodified layering sphere (red, solid) and the perfect integrating sphere (blue, dash-dot). The improved illumination uniformity obtained with the modified layering sphere is obvious and compares favorably with the data obtained for the perfect integrating sphere.

The ratio of peak-to-valley variations in intensity can be used to quantify the illumination uniformity (1 = perfect uniformity). The intensity ratio for the original layering sphere, the modified layering sphere, and the perfect integrating sphere are 2.78, 1.52, and 1.32, respectively. A vast improvement thus resulted from the implementation of a wide-angle diffuser. Of course, these data were taken for equatorial views with all windows closed and keyhole outside the scan.

3.5 Effect of Open Windows

The layering sphere has two pairs of opposing sapphire windows (~6-mm diameter) oriented along axes corresponding to the viewing axes in the OMEGA target chamber. The windows corresponding to the X- and Y-axis views are positioned 26.6^{o} and 12° above and below the equator, respectively, and 110° apart. Thus it is possible to detect the impact of opening the windows on illumination uniformity by the equatorial scan.

Figure 8 shows the effect on intensities that demonstrates the lack of scattered light from the regions of the open windows. We note that the intensity curves are nearly identical for open and closed windows except for one significant valley area at about 120°. A secondary dip near 20° is less pronounced. The difference in the perturbations caused supposedly by the two sets of two windows is due to the angular offset of the windows (12° and 26.6^{o}). It is believed that the 12° windows are almost completely covered by the equatorial view while the 26.6^{o} windows are only partially seen. In principle, two large perturbations due to the 12° windows and two small perturbations due to the 26.6^{o} windows should be observed. On the contrary, only one large perturbation and one small perturbation were notable in Fig. 8. The 100° separation between the intensity valleys is very close to the actual azimuthal angular offset of the 26.6^{o} and 12° window locations. No significant perturbations due to the other 26.6^{o} and 12° windows were observed in Fig. 8. One of the possible explanations for this discrepancy is that the periscope was not properly positioned and the "equatorial" scan was actually biased in one direction. In light of this, we feel that this conclusion is still valid: windows cause perturbations on the illumination uniformity.

3.6 Effect of Keyhole

In order to investigate the effect of the keyhole on the illumination uniformity at the center of the sphere, a tilted-plane scan of the layering sphere was established. The periscope is

inserted through one of the windows of the layering sphere (Fig. 9). This scan permits a partial view of the keyhole, a complete view of the window through which the periscope was positioned, and a small view of the opposite window with angular offset of approximately 24°.

Figure 10 shows the effect of the keyhole on the uniformity perturbation in the tilted-plane view with all windows open. The dash and solid curves were acquired from the original and the modified layering sphere. There are two significant intensity valleys in both cases. One at about 160° is attributed to the keyhole and the other at about $30\text{-}40^o$ is due to one of the open window through which the periscope was positioned. The keyhole causes much more significant perturbation of intensity on the target over a wider range of angle than any other factors.

Although the area of the entry keyhole is 2% to 3% of the total area, the results (Fig. 10) indicate that it is the single, most profound feature affecting illumination uniformity. The only way to ameliorate the conditions is to simply reduce its size. In addition, the tilted view does not see the complete effect of the keyhole—the perturbation is expected to be even worse.

3.7 Illumination Uniformity Factor

The illumination uniformity factor, ε is defined as the ratio of peak (maximum) to valley (minimum) intensity, as described in Section 3.4. The ε value of perfect illumination uniformity is equal to one (unity); the higher the ratio value, the greater the deviation of peak. Table I summarizes the illumination uniformity factor versus various experimental settings (column 2-6).

Table I. Illumination uniformity factor quantifying the improvement due to the optimal wide-angle diffuser configuration and various effects.

	Main setting	Modifications	Windows	Scan type	Feature scanned	Uniformity Factor, ε
Goal	Perfect integrating sphere	None	None	Equatorial	None	1.32
1	Original layering sphere	Initial design	Closed	Equatorial	None	2.78
2	Original layering sphere	Initial design	Open	Equatorial	Windows	4.08
3	Original layering sphere	Initial design	Open	Tilted	Keyhole	6.25
4	Modified layering sphere	Wide-angle diffuser	Closed	Equatorial	None	1.52
5	Modified layering sphere	Wide-angle diffuser	Open	Equatorial	Windows	1.89
6	Modified layering sphere	Wide-angle diffuser	Open	Tilted	Keyhole	4.17

The illumination uniformity factor is also plotted in Fig. 11 to better illustrate that the layering sphere modified with a wide-angle diffuser improves the illumination uniformity in all cases, as compared to the original layering sphere under the same experimental settings.

4. Summary and Recommended Future Work

The results in Table I and Fig. 11 have already demonstrated a significant improvement in illumination uniformity from the layering sphere with a wide-angle diffuser configuration, but future work using a computer-controlled movement of the periscope (or a miniature CCD/IR camera) along the axis perpendicular to the equatorial plane and to the tilted plane for the collection of views over almost the entire layering sphere is suggested. The data can be stitched together to provide a 3-D illumination map. This map can then be quantitatively correlated region by region with an ice layer thickness variation map. The quantitative contribution of the keyhole, blind spot[4] and other imperfections in the layering sphere to the ice layer thickness variation can be evaluated. Furthermore, the upper limit of the illumination factor can then be set.

Other future work is also recommended to better understand the effect of the diffuser on the thermal environment of the target since a temperature gradient of a few hundredths of a degree in the layering sphere can cause a significant variation in the ice layer thickness.[10] The engineered diffuser used in the modified layering sphere needs to have very low absorption at 3.16 μm, which we have not measured in these experiments. Another solution would have to be found to spread the input beam if the absorption were significant. The experiment using the diffusers should also be performed using the real fiber-coupled heating IR laser instead of the surrogate LED red light.

New problems may be posed by all these tasks. However, the prospects and principles of better uniformity due to wide-angle light distribution remain highly promising.

5. Conclusion

The original layering sphere was found to have poor illumination uniformity due to scattering properties of the inner surface. The first two bounces of the heating laser cause significant bright spots. We have improved the target illumination uniformity inside the layering sphere due to the first and second bounce bright spots of the heating laser. In contrast, a perfect integrating sphere does not show these bright spots. The bright spots were identified to be due to the non-Lambertian scattering characteristics of the layering sphere. Insertion of a wide-angle engineered diffuser improved the illumination uniformity almost to the level of the perfect integrating sphere, because the first bounce illumination area was greatly increased. Unfortunately it was confirmed that the presence of the large keyhole and four windows in the layering sphere cause very significant illumination non-uniformities.

6. Acknowledgements

First and foremost, I would like to thank my advisor, Dr. Wolf Seka, for his time and effort in helping me with this project. I am also grateful to Dr. R. Stephen Craxton for giving me the opportunity to be a part of the 2005 Summer High School Research Program. I would like to thank my fellow comrades at the LLE who were in the program with me, for their continual support. Also, I need to thank both Michelle and Josh for their help with the MATLAB programs and professional yet friendly presence in the lab. The photos Eugene Kowaluk took that are used in this presentation were astounding, thank you for your help as well. Lastly, I would like to thank my family for their support and help, all along the way.

7. References

*   This report is based on the work at the LLE Summer High School Student Research Program, July 5 - August 29, 2005.
1.   J. Nuckolls et al., Nature, 239, 139 (1972).
2.   T.R.Boehly, D.L. Brown, R.S. Craxton, R.L. Keck, J.P. Knauer, J.H. Kelly, T.J. Kessler, S.A. Kumpan, S.J. Loucks, S.J. Letzring, F.J. Marshall, R.L. McCrory, S.F. B. Morse, W. Seka, J.M. Sources and C.P. Verdon, Opt. Commun., 133, 495 (1997).
3.   LLE Review, "Formation of Deuterium-Ice layers in OMEGA Targets", 99, 160 (2003)
4.   D.E. Edgell, "Three-Dimension Characterization of Ice Layers for Cryogenic Targets at LLE", Presented at the 46th Annual Meeting of the American Physical Society, Division of Plasma Physics, Savannah, GA, November 15-19, 2004.
5.   D.R. Harding, M.D. Wittman, L.M. Elasky, S. Verbridge, L.D. Lund, D. Jacobs-Perkins, W. Seka, D.H. Edgell, and D.D. Meyerhofer, "OMEGA Direct-Drive Cryogenic Deuterium Targets," Presented at the 46th Annual Meeting of the American Physical Society, Division of Plasma Physics, Savannah, GA, November 15-10, 2004.
6.   L. Weiss, "Categorization and Analysis of Defects in Cryogenic Targets", Presented at the 2005 Summer High School Student Research Program Symposium, Laboratory for Laser Energetics Coliseum, August 24, 2005.
7.   LLE Review, "Initial Performance of the High Pressure DT-Filling Portion of the Cryogenic Target Handling System", 81, 6 (1999).

8. A Lambertian surface is a surface of perfectly matte properties, which means that it adheres to *Lamberts cosine law*. Lamberts cosine law states that the reflected or transmitted *luminous intensity* in any direction from an element of a perfectly diffusing surface varies as the cosine of the angle between that direction and the *normal vector* of the surface. As a consequence, the *luminance* of that surface is the same regardless of the viewing angle.

9. M. Alexander et al., Reflected luminous intensity data taken from a typical gold-coated rough surface, LLE, August 2004.

10. D.R. Harding, "Forming Smooth Cryogenic Targets for OMEGA Direct-Drive ICF Implosions and Prospects for Direct-Drive Targets for the NIF, Presented at the 47th Annual Meeting of the American Physical Society Division of Plasma Physics, Denver, CO, October 24-28, 2005.
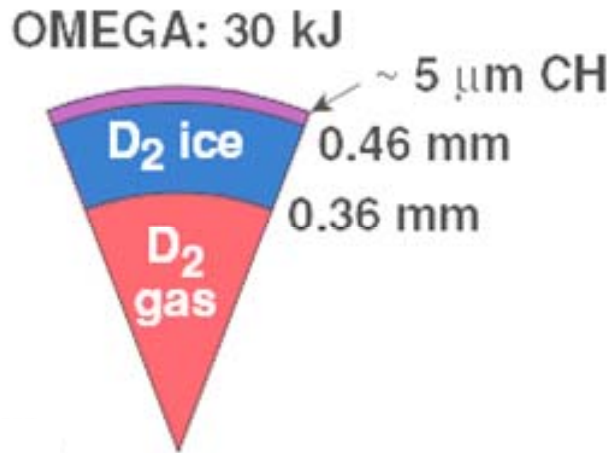
Fig. 1   Cross sections of OMEGA direct-drive targets, showing target component layers and their dimensions. Purple: CH for a thin plastic shell. Blue: cryogenically frozen D_2 layer.

(a)   (b)
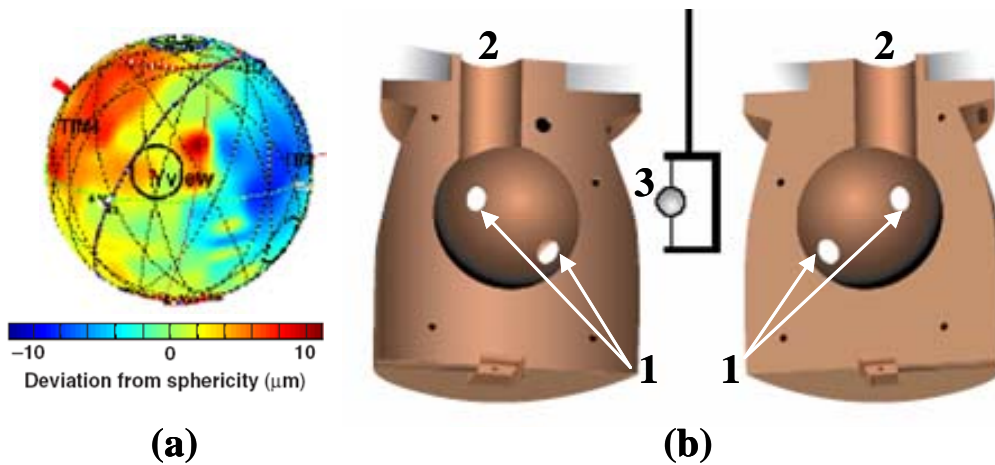
Fig. 2   (a) A 3-D plot of deuterium ice layer thickness using optical shadowgraphy shows ice layer thickness deviation.[5]   (b) The layering sphere, shown in two hemispheres side by side, has (1) two pairs of opposing windows. The (2) "keyhole" opening at the base of the layering sphere is where the (3) target, mounted on four web of spider silks supported by a hook, is inserted and removed.
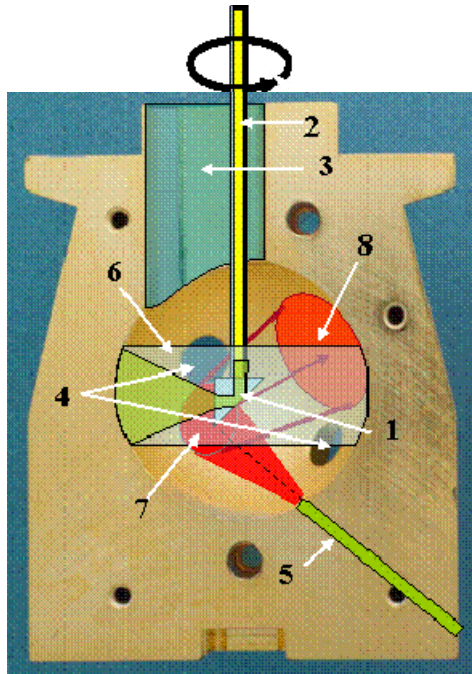
Fig. 3 Experimental setup of the periscope inside the layering sphere. 1: Periscope prism coupled to a 0.5mm optical fiber. 2: 0.5mm optical fiber through a rigid tube. 3: Keyhole. 4: Target viewing windows. 5: Fiber-coupled surrogate LED. 6: Schematic of the equatorial region "seen" by periscope. 7: First-bounce bright spot. 8: Second-bounce bright spot.

(a)   (b)
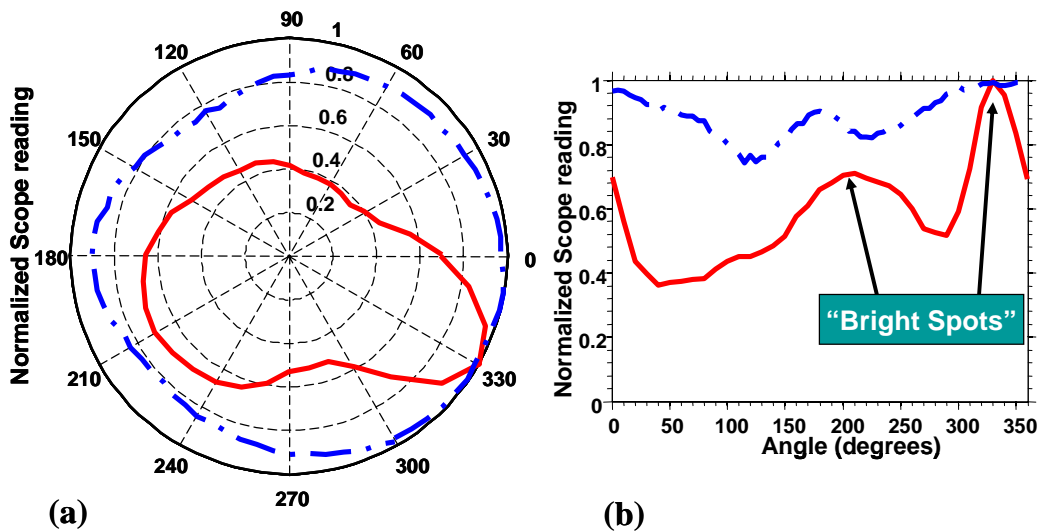
Fig. 4 Normalized intensity *versus* angle of periscope rotation in (a) polar and (b) Cartesian plot. Red curves (solid): the layering sphere with all windows closed. Blue curves (dash-dot): a perfect integrating sphere.
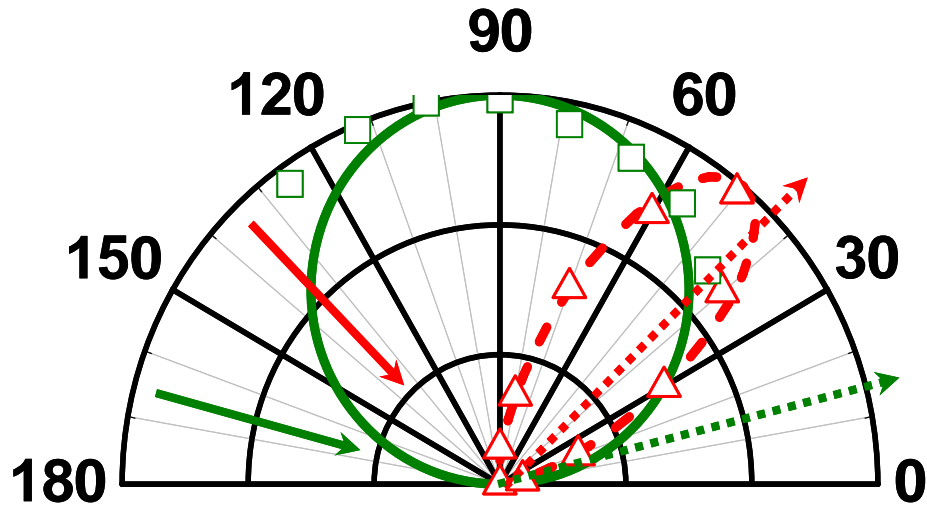
Fig. 5 Normalized reflected intensity *versus* angle (degree) in polar plot. Typical roughened, gold-coated surface - red arrow (solid): incident ray at 135°; red arrow (dotted): specular reflection at 45°; red (triangles): measured intensity distribution[9]; red curve (dash): calculated intensity distribution using $\cos^{9}(\theta-\theta_0)$ dependence[4]. Ideal surface of the witness piece to a perfect integrating sphere - green arrow (solid): incident green light (530nm) at 165°; green arrow (dotted): specular reflection at 15°; green (squares): measured intensity distribution; green curve (solid): calculated distribution using Lambert's cosine law.
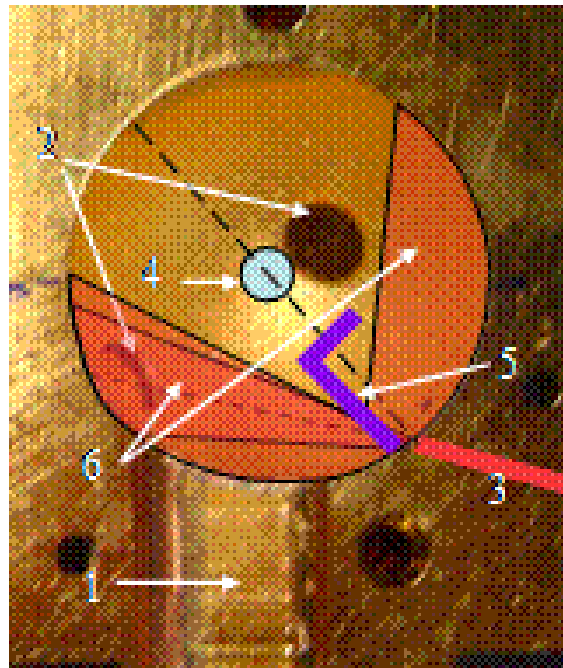
Fig. 6 Modified layering sphere with engineered diffuser mounted for optimal illumination uniformity at the center of the sphere. The components are 1: keyhole, 2: windows, 3: LED beam, 4: target location, 5: wide-angle diffuser configuration and 6: light spread by diffuser.
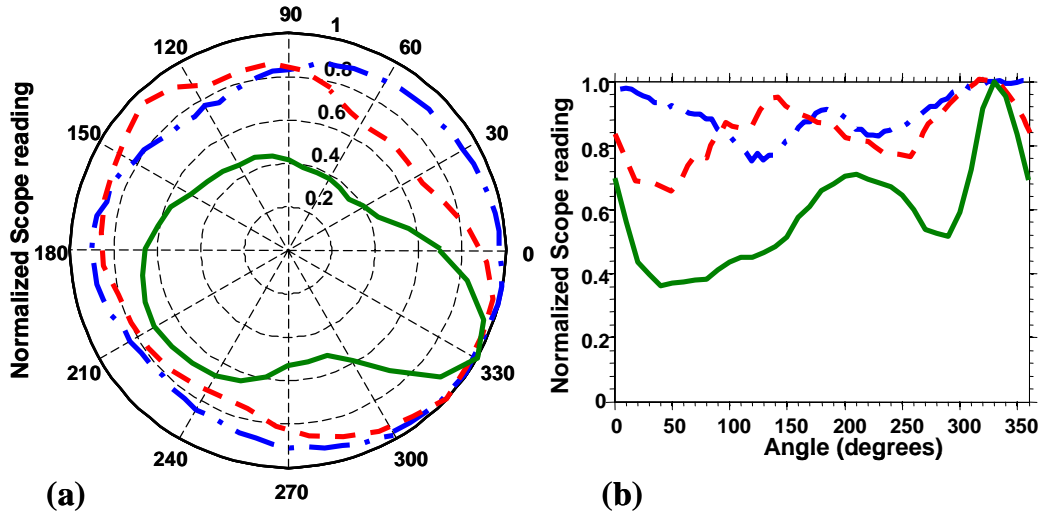
Fig. 7   Normalized intensity *versus* angle of periscope rotation in (a) polar plot and (b) Cartesian plot. Red curves (dash): layering sphere with the current best diffuser configuration. Green curves (solid): original layering sphere. Blue curves (dash-dot): a perfect integrating sphere.
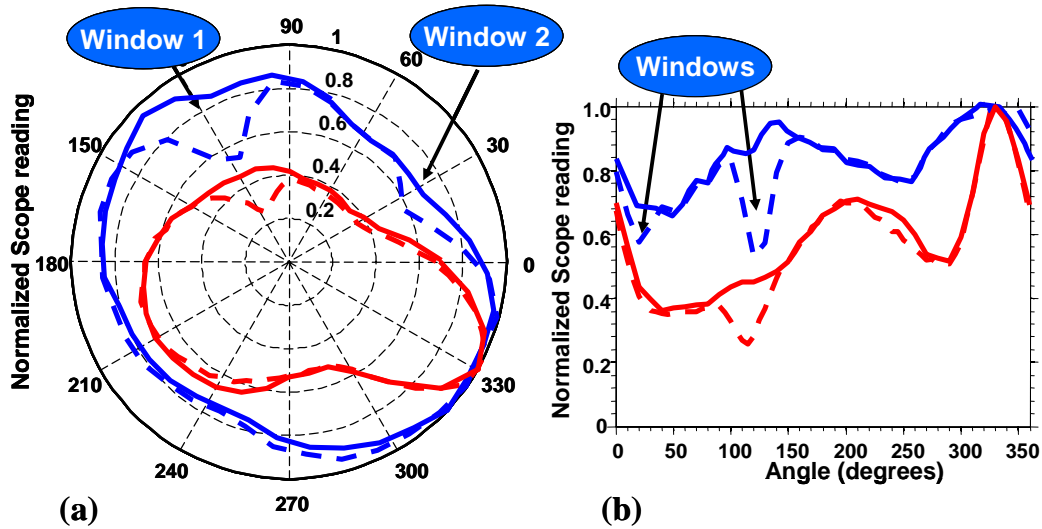

Fig. 8   Normalized intensity *versus* angle of periscope rotation in (a) polar plot and (b) Cartesian plot. Red curves: original layering sphere. Blue curves: modified layering sphere with the current best diffuser configuration. Solid curves: windows closed. Dash curves: windows open.
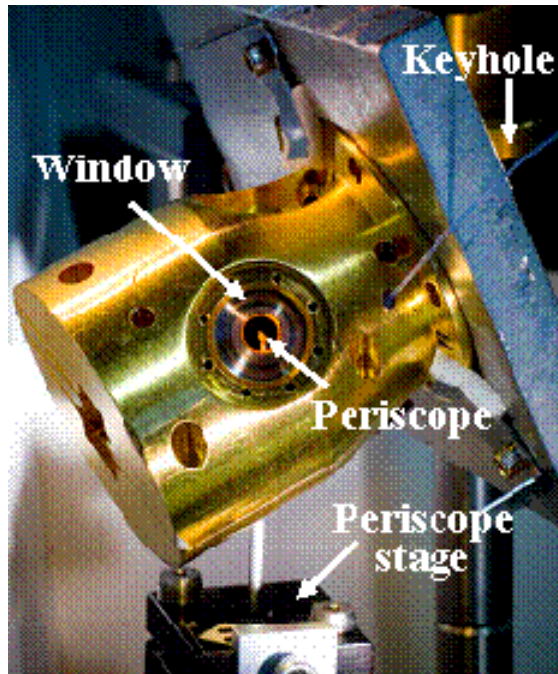
Fig. 9   Photograph of the tilted-view setup. The layering sphere is tilted and the periscope is inserted through a window.
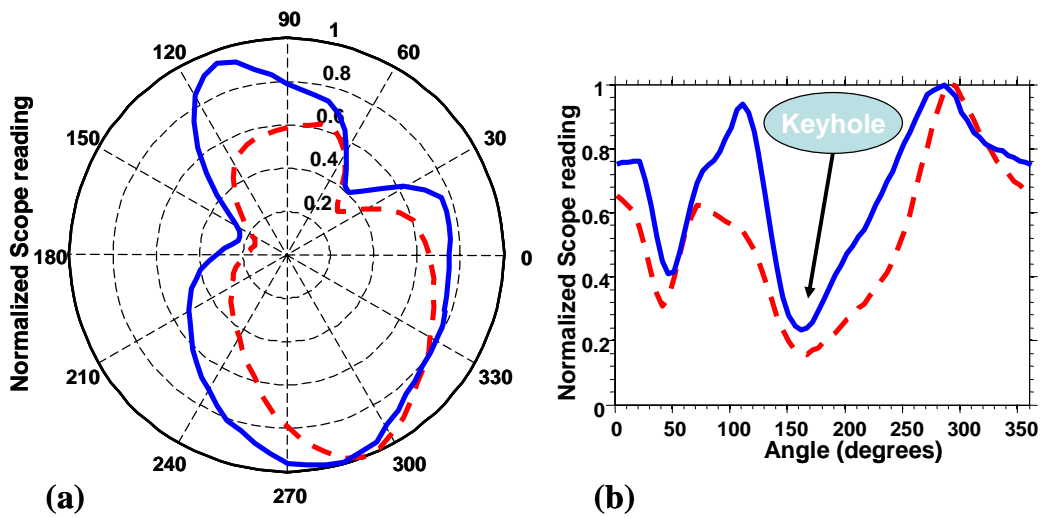

(a)

(b)

Fig. 10 Normalized intensity *versus* angle of periscope rotation in (a) polar plot and (b) Cartesian plot using the tilted-plan view. Blue curves (solid): the layering sphere modified with the current best diffuser configuration. Red curves (dash): the original layering sphere. Both with windows open.
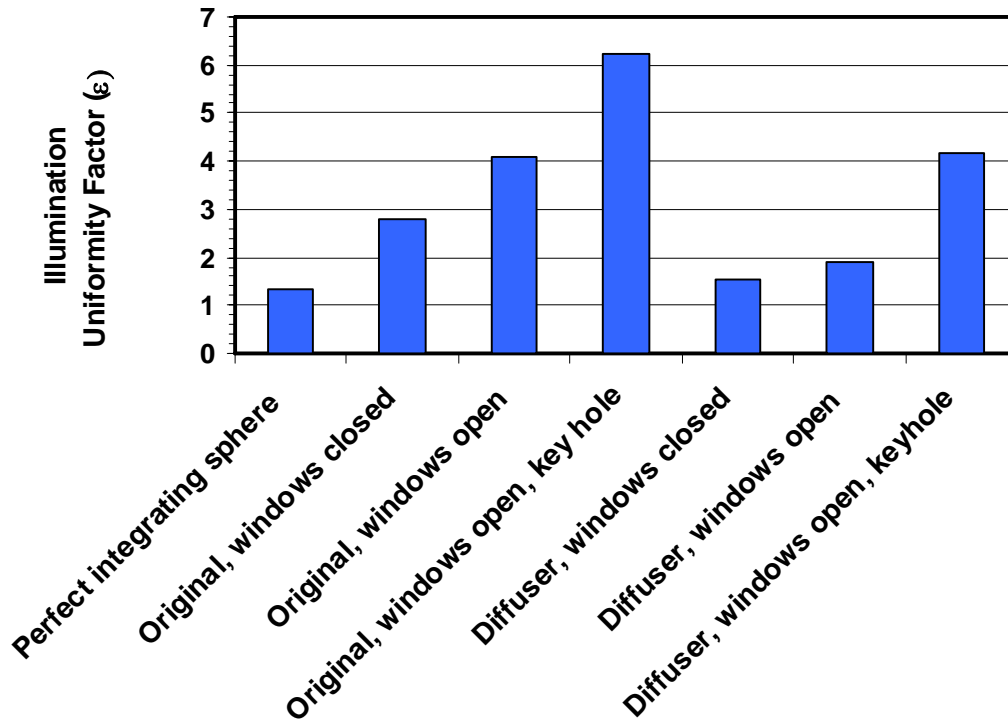
Fig. 11 Illumination uniformity factor *versus* different experimental settings.

X-Ray Framing Camera Characterization Automation

2005 Summer Research Program
By: Nicholas Ramos
Advisor: Shawn Mott
2nd Advisor: D. Lonobile

The 60-Beam OMEGA laser system employs a number of x-ray framing cameras (fig. 1). The function of these cameras is to generate digital images of the target implosion using a backlight which silhouettes the target in x-rays. The x-ray framing camera, hereafter referred to as the XRFC, then registers the silhouette and records the data. The cameras are used to measure the implosion density and uniformity, and several other critical factors of the target implosion.

This is a standard x-ray framing camera that is used by the URLLE.

X-ray framing cameras take images by backlighting the target with

x-rays, and looking at the degree at which the x-rays penetrate the

target.

Figure 1

All of the XRFC's in current use are several years old, and are still characterized according to their factory settings. Perceptibly, the original settings can degrade over time, and without proper maintenance and preservation, the settings can deteriorate to such a point that the image quality and accuracy is severely corrupted. But the cameras are difficult to calibrate, and accuracy can be affected by this. The reason for this is the considerable amount of time it takes to characterize an XRFC. It can take up to eight hours to completely characterize a single camera. A series of reading must be taken, 126

readings total, for each voltage setting and each bias setting. And with a high demand for the camera to be used for target shots, the cameras are rarely available for more than a few hours, let alone the eight needed to properly characterize a camera. The main reason for the tight schedule is the fact that for each individual target shot, the cameras themselves need to be adjusted and choreographed with the other cameras used in the target shot. This alone can take from one hour well up to four hours. Moreover, these cameras are being fine tuned according to the base settings which are more than five years old.

As is evident from the current situation, a faster and more efficient way of characterizing the XRFC's is needed. The proposal made was to design, construct, and test a fully automated module that can take all of the necessary measurements for the complete characterization of the XRFC. The past summer was spent designing the appropriate circuitry, and constructing the actual module. What will also need to be designed and constructed is a program to interpret this information, and put it into a Microsoft Excel file.

The benefits of this project will be that XRFC's will now be able to be characterized, and calibrated for higher image quality. It will take only ten minutes to take all of the readings, contrasting to the eight hours currently necessary. This module will also eliminate the problem of human error in the characterization process. A single mal-recorded setting could throw off the entire characterization of the XRFC. This would effectively cancel out eight hours worth of work, and forfeit an entire day's worth of possible use of the XRFC.

*   *   *   *   *   *   *   *   *   *   *   *   *

A module for the XRFC needed to be designed, refined, and constructed. The majority of the program was spent on the design and on refining the design. A program called *ORCAD Captu*re was used to create a draft schematic of the module. This program uses a series of symbols, all of which represent a circuit part in real life, to model the schematic. The overall schematic took roughly 2 weeks to complete and refine. It comprised a PIC Microcontroller, several bidirectional buses, and two RS232 converters. There was also a secondary board, the high-voltage (HV) relay board, made to function simultaneously with the main board. The secondary board would handle the flow of the high voltages put out by the XRFC. Voltage levels could reach in excess of 4000 volts. Several safety precautions were taken in the designing of the module in which the circuitry was to be placed.

The actual enclosure in which the circuitry was going to be put was an aluminum flanged inclusion. This would allow the box to be grounded in case of any shorts or any surges. Also, the HV relay board was coated in a non-conductive material in order to isolate the current. Extra wide traces were etched into the board for added safety. Lastly, the HV relay board and the main board were kept a distance away form each other in the enclosure. All of this had to be taken into account when designing the circuitry.

The enclosure itself is approximately 8" x 4". This can put some restraints on the spacing of the circuitry. The boards needed to be fairly compact, although the density of the components was not too tight.

We were able to plan all of this out using a sister program called *ORCAD Layout*. This program allowed us to import an *ORCAD Capture* file and have the Layout program actually draw out the connections and give us a 1:1 scale of what the finished product

would look like. About 3 weeks was spent on the layout. Part of the reason this process takes so long is the many errors that occur when drawing a part. Every single variable is checked by the computer and matched up with factory standards. If something is not up to spec, then the program will identify the error and where it is located.

After the boards were completed in Layout, the files were converted to a factory file. A machine can interpret the information in these files and generate the boards. The boards were produced off site because of the need for high efficiency and quality. There was not the necessary time to allow a board to be produced at the lab. The files were emailed out and the board was manufactured and sent back about three days later.

Upon receiving the board, the process of populating the board started. The board comes bare, with only the traces etched in and the holes and vias drilled. It is the customer's job to solder in all of the components which are to be placed on the board. This is a relatively quick process, depending on board size. Populating the board took about one afternoon to do. After populating the board, it was tested and measured under low voltage. The HV relay board was also constructed and populated, and was not tested for safety reasons. It was simple enough that testing was not required.

Several problems occurred with the main board. All were easily remedied within a few days. After the problems were solved, the board was put into the aluminum enclosure with the HV relay board and was attached to the power supply. A final test was performed, and everything checked out.

At the very start of the program, all that had been accomplished was a list of the needed parts, a basic part requisition, and a general schematic of the boards that were to

be produced. The schematic lacked RS232 converters; completed wiring for the PIC

Micro controller, resonators, and the design of the HV relay board still needed to be

completed. All of this needed to be designed and refined before any prototyping could be

completed. There was also a considerable amount of time taken in order to double check

all of the components and placements. The schematic was completed within a few weeks.

Many capacitors were also put in place. The capacitors would smooth out the electrical

path and keep many of the electronic components in the circuit safe.
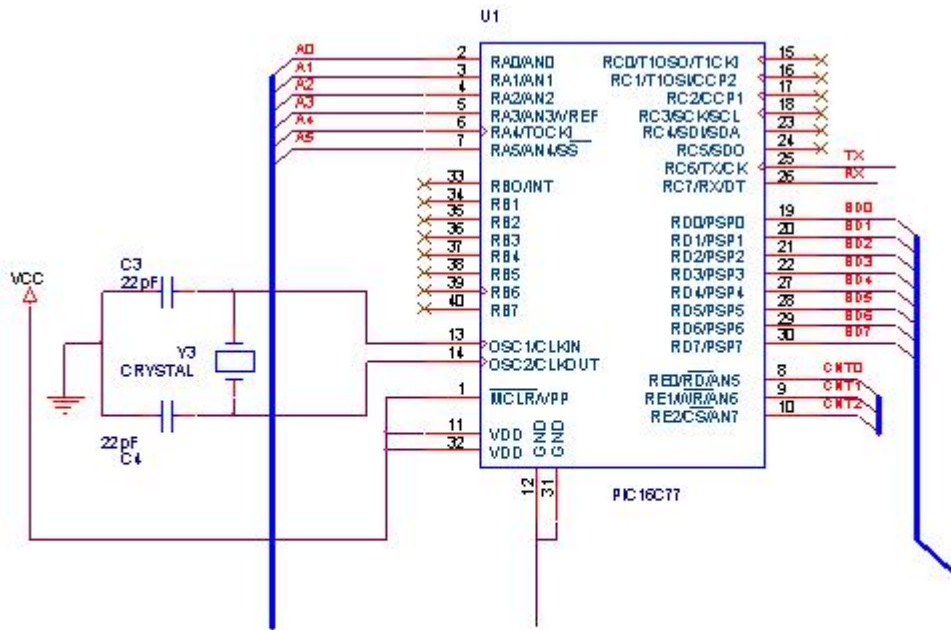
This is the PIC Microcontroller in ORCAD Capture. It has a

resonator wired to it externally, as well as several busses leading

away to the HV Relay Board, twin 6850 chips, and the RS232

converters.

Figure 2

The PIC Micro controller (fig. 2) was the main focus of the board, and virtually

everything was connected to it. The final wiring of the PIC required careful planning and

understanding of each of the output areas on the controller. Also, resistor packs were needed to control the amount of current and voltage that was being passed into the busses. The correct resistors needed to be found and placed in proper conjunction with the traces in the diagram. Finally, the connectors and HV relay board needed to be designed. For connectors, simple six-prong connectors were used. Instead of having the RS232 9-PIN connectors on the board, we lead wires between the RS232 db9-PIN and the db6-PIN connectors on the board. This allowed easier construction and the ability to replace the boards without replacing the entire network of db9-PIN connectors.

The 4000 V HV relay board was fairly easy to design on the *ORCAD* program. Consisting simply of five HV relays and a single six pin connector, the board took very little time relative to the main board. But careful consideration would need to be taken in order to ensure safety during construction.

One final step of the design of the two boards was the gathering of the "footprints" for each individual part. A resistor has a different footprint than a capacitor, and two capacitors may even have different footprints from each other (fig. 3).
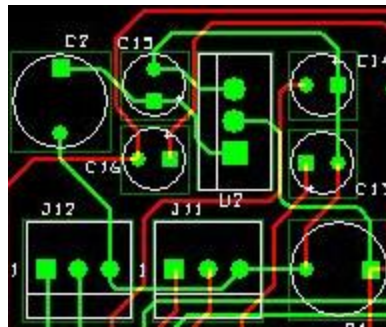
There are several different capacitors in this image named (C2, C13, C14, and C15). Each has a different footprint than the next.

Figure 3

There were several minor footprint errors associated with the layout we had designed. We discovered this upon uploading the design files into *ORCAD Layout*. The program proceeded to give several PCB footprint errors. It appeared that there were errors in the footprint files. The footprint files appeared to be incapable of converting to *ORCAD Layout* files. These footprint problems consumed much of our time while we located the source of the problem. There appeared to be a faulty piece of data in the footprint files we had provided the program with. After the problem was resolved, transfer of the *ORCAD Capture* files was carried out, and then the design in *ORCAD Layout* commenced.

The *ORCAD Layout* program allows a designer to place traces on the bottom or top of the board, making it possible to wire up very complex circuits. Silk screen layers are also applicable, along with many other features. We used *Layout* to finish up the final wiring of the main board and the HV relay board. The main board wiring went on without a problem, but careful consideration of the HV relay board's high voltage traces needed to be taken into consideration during its final design. Extra wide traces were put in place, along with the consideration of isolating the high voltage traces. Each trace was placed a minimum distance form any other trace. Also, traces were kept as far away as possibly from any of the high voltage pins on the relays.

There were several problems that needed to be corrected. One problem was the two 6850 IC chips had been manufactured with the wrong footprint. This problem was easily corrected. We constructed a small daughter board that had the correct footprint for the 6850 chips. This entire process took no more than a couple of days. And as a final safety precaution with the relay board, an insulating gel was coated over the traces to further isolate them from any arcs that might occur during operation.

The final step in the completion of this phase of the project was the manufacturing of the aluminum enclosure for the HV relay board and the main board. We had come to the conclusion that the relay board was going to be in a separate enclosure from the main board. This would isolate the high voltage from the main board, and would allow proper grounding of the relay board. Also, the second enclosure for the HV relay board needed to be taller in order to provide adequate clearance for the HV relay board. The board needed to be a considerable distance away from any metal surfaces as a safety precaution. Both enclosures, the main board enclosure and the high voltage enclosure, were joined by an insulated six pin connector. The enclosure was sealed, and completed within a week, and the boards were secured inside along with the power supply. This completed my phase of the project. The programming of the code, a GUI, and the PIC coding still will need to be carried out.

Contaminant Resistant Sol-Gel Coatings

Valerie Rapson
Greece Olympia High School

Advisor: Kenneth L. Marshall

University of Rochester
Laboratory for Laser Energetics
Summer High School Research Program 2005

1. Abstract

Sol-gel coatings are used on the OMEGA laser optics as anti-reflection (AR) coatings to maximize their transmittance. Over time, trace organic compounds in the laser bay contaminate these sol-gel coatings, reducing their efficiency as AR coatings. Consequently, the optics must be removed, cleaned and re-coated with the sol-gel AR approximately every three months. In April of 2005 Y. Xu *et al* [1] demonstrated that changing the chemical composition of the sol-gel would reduce its susceptibility to contamination. In the work reported here, dimethyldiethoxysilane (DDS) and methyltriethoxysilane (MTES) were used to modify standard sol-gel solutions based on tetraethylorthosilicate (TEOS) in order to increase its resistance to contamination by volatile and semi-volatile contaminants. The methyl groups in the added components reduce the number of active OH groups available for hydrogen bond formation with contaminants in the air. The resulting coatings show improved contamination resistance, can be applied to OMEGA optics with only minimal changes to the current spin-deposition process, and show equivalent or superior laser damage resistance to current sol-gel AR coatings used on OMEGA.

2. Introduction

Originally created 60 years ago, sol-gel coatings are deposited on optics to form an anti-reflective (AR) coating, which maximizes their transmittance. Sol-gel coatings are used on a substantial number of the optics that make up the OMEGA laser. Each optical element has a potential optical loss associated with it, and the sol-gel AR film helps to reduce surface reflective loss. The sol-gel process involves the evolution of inorganic networks through the formation of a colloidal suspension (sol) and gelation of the sol to form a network in a continuous liquid phase (gel). Sol-gel formation occurs when a metal alkoxide such as tetraethylorthosilicate (TEOS) is combined with an alcohol (ethanol) in the presence of either an aqueous acid or an aqueous base. The resulting hydrolysis reaction replaces the alkoxide groups (OR) with hydroxyl groups (OH). Condensation reactions involving the resulting silanol groups (Si-OH) produce siloxane bonds (Si-O-Si), with water and the alcohol (ROH) as by-products.
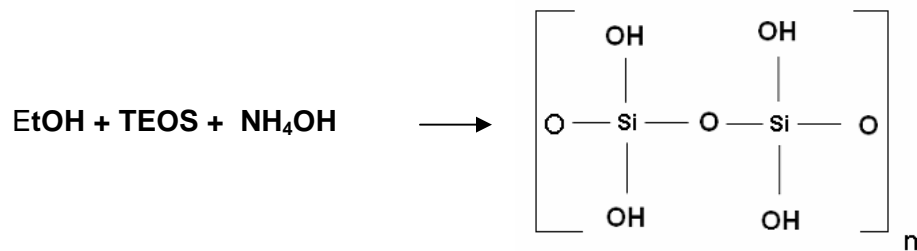
Figure 1: structure of sol-gel molecules

When the sol particles inter-twine into a network, a gel is formed. As the gel continues to dry, condensation reactions continue to occur. Water and alcohol are driven off and the network continually becomes smaller, forming what is called a "xerogel".

2

The characteristics and properties of the sol-gel network are determined by a number of factors that can affect the rate of both the hydrolysis and condensation reactions. These factors include pH, solution age, temperature, and drying rate or time. By controlling these factors, it is possible to vary the structure and properties of the sol-gel.

Recently, Y. Xu *et al*[1] have reported that sol-gel coatings can be made more contamination-resistant by modifying standard silica sol-gel solutions through co-hydrolysis with other organosiloxane additives. In the co-hydrolysis method, either methyltriethoxysilane (MTES) or dimethyldiethoxysilane (DDS) was added to a standard TEOS-based sol-gel solution at various molar percentages of X, where $X = M_x/(M_x + M_{TEOS})$. M_{TEOS} is the number of moles of TEOS and M_x is the number of moles of the organosiloxane additive (in this case, either MTES or DSS). Xu *et al* [1] prepared and evaluated solutions with molar percentages ranging between 10% and 50%. Their work showed that the sol-gels modified with DDS at 30 mole percent were the most contamination resistant. Based on their method, TEOS-based sol-gel coating solutions used at LLE were modified with MTES and DDS and the effectiveness of the resulting co-hydrolyzed sol-gel solutions were tested for their resistance to contamination by both moisture and volatile organic compounds. The project goal was to develop contamination-resistant AR sol-gel formulations that could be applied to OMEGA optics with minimal changes in the deposition process while at the same time maintaining or exceeding the high laser damage threshold of the standard TEOS-based sol-gel coatings currently deployed on OMEGA.

3. Experimental Data

The standard sol-gel solution used by the LLE Optical Manufacturing Group (OMAN) consists of a mixture of 22.0425 L of ethanol, 2.320 L of TEOS, and 717.5 ml of ammonium hydroxide (NH_4OH). This production batch size was scaled down to smaller amounts for the co-hydrolysis experiments. The ethanol and TEOS were added first and stirred for approximately 3 hours. Ammonium hydroxide was then added and the solution was stirred for another 2 hours. Once this was completed, the sol-gel solution was placed in a closed container and allowed to stand for 3 days. This standard TEOS-based sol-gel solution was used as the starting stock solution for preparation of the modified, co-hydrolyzed sol-gel mixtures. Six 100 ml portions of the standard sol gel stock solution were combined with solutions of 10%, 20% or 30% of either MTES or DDS in ethanol to create the co-hydrolysis mixtures. To determine the amount of each solute to use, the formula

$$X = M_x/(M_x + M_{TEOS}).$$

is solved for M_x, where X is either 0.1, 0.2 or 0.3. To simplify the calculation, M_{TEOS} was set equal to one mole and the resulting amount for M_x was scaled down according to the actual amount of TEOS used to make each solution. To calculate how many grams of MTES or DDS are needed, the number of moles that corresponds to the weight percentage of the solute of interest was multiplied by the gram molecular weight of either MTES or DDS. The amounts of TEOS needed were scaled down from 2.320 liters to 9.2ml for a 100ml solution.

Once the co-hydrolyzed sol-gel solutions had aged for 3 days, they were spin coated onto substrates in the Optical Materials laboratory clean room. During spin

coating, the substrate is first flooded with the sol-gel and then spun at a certain rpm for a designated length of time. The thickness of the coating is affected by both the spinning speed and the time the substrate is spun for. The thickness in turn determines to a certain extent the wavelength at which the anti-reflective (AR) properties of the coating are the most efficient. The standard TEOS-based sol-gel coating was spun at 4000 rpm for 40 seconds, while all of the co-hydrolyzed sol-gel solutions were spun at approximately 4.8 rpm for 20 seconds. This same process was repeated after the coating solutions had aged for 6 days. The percent transmittance of each sol-gel coated substrate approximately one day after spin deposition was measured using a Perkin Elmer Lambda 900 UV-VIS-NIR spectrophotometer. An uncoated substrate was placed in the reference beam of the spectrophotometer to subtract the absorbance characteristics of the substrate from the data. The samples were scanned over a wavelength range between 300 nm and 1500 nm. The wavelength of maximum AR efficiency of the coating was taken as the point of highest transmission on the transmission vs. wavelength curves. After 5 days exposure to laboratory air, the transmittance of each sample was measured again and compared to the original data. Table 1 summarizes these results.

Sol-Gel Composition	Amount prepared (ml)	Spin Speed (rpm)	Spin Time (sec)	% Transmittance @AR λ_{max}		Δ %T (Δλ)
				1 day exposure*	5 days exposure*	
TEOS stock soln.	250	4000	40	95% (533 nm)	94.1% (567 nm)	0.9% (34 nm)
MTES 10%	100	4800	20	94.8% (592 nm)	94.6% (627 nm)	0.2% (35 nm)
DDS 10%	100	4800	20	94.2% (573 nm)	94.2% (667 nm)	0.0% (94 nm)
MTES 20%	100	4800	20	94.8% (613nm)	93.3% (601 nm)	1.5% (12 nm)
DDS 20%	100	4800	20	94.7% (607 nm)	93.5% (670 nm)	1.2% (63 nm)
MTES 30%	100	4800	20	92.4% (530 nm)	94.3% (493 nm)	1.9% (37 nm)
DDS 30%	100	4800	20	91% (540 nm)	91.3% (601 nm)	0.3% (61 nm)

*Same sample evaluated 1 day after spin-coating and 5 days after exposure to laboratory air

Table 1: *Summary of sol-gel spin coating and transmittance data. λ_{max} = maximum AR wavelength; Δ%T=change in transmission between samples 1 and 2; (Δλ) = change in wavelength between samples1 and2*

Six different substrates each containing a standard TEOS-based sol-gel layer were exposed to decahydronaphthalene, isooctane, hexane, machine oil, deionized water, and ethanol in sealed containers at room temperature (as shown in Fig. 2) for 24 hours to produce a saturate environment of the contaminant. The change in the transmission characteristics of the coatings before and after exposure was determined. The same test procedure was followed for the co-hydrolyzed sol-gel samples employing MTES and DDS.

Figure 2*: Sealed containers where various coated substrates were exposed to contaminants.*
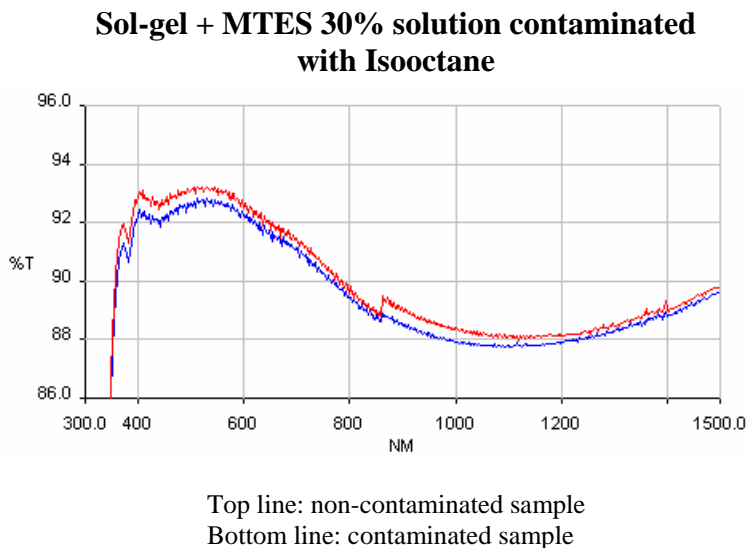
A majority of the results are shown in Fig. 3, and the general trend indicates that solutions with a higher percentage of DDS or MTES were more contaminant resistant. It is unclear why some samples had an *increase* in transmittance after exposure. More testing will be conducted to determine whether these results are valid.

Sol-gel Contaminated with Isooctane

Top line: non-contaminated sample
Bottom line: contaminated sample

Sol-gel + MTES 30% solution contaminated with Isooctane

Top line: non-contaminated sample
Bottom line: contaminated sample
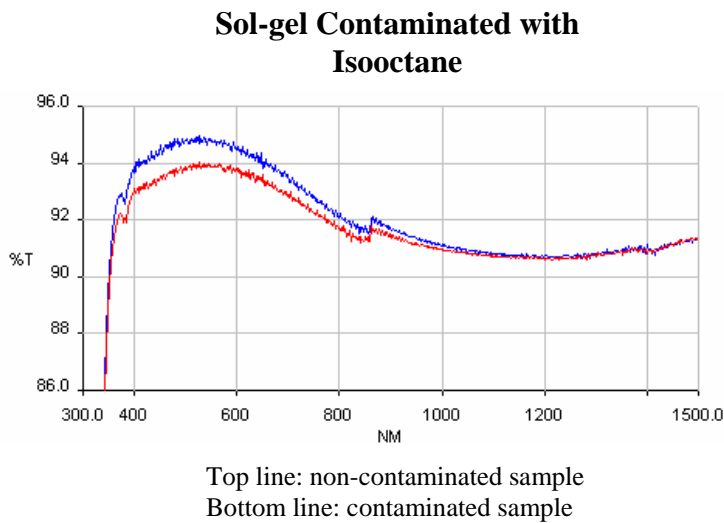
type	change in transmittance
Isooctane	
DDS10	no change
MTES20	<0.1% decrease
MTES30	0.1% decrease
MTES10	0.3% decrease
DDS30	0.5% decrease
DDS20	0.5% decrease
sol-gel	1% decrease
Ethanol	
DDS20	0.5% increase
DDS30	0.2% increase
MTES30	0.1% increase
sol-gel	0.1% increase
MTES20	<0.1% increase
MTES10	0.1% decrease
DDS10	.04% decrease
Decahyronaphthalene	
MTES30	0.4% increase
DDS20	<0.1% increase
MTES10	no change
MTES20	0.1% decrease
sol-gel	0.1% decrease
DDS10	0.1% decrease
DDS30	0.7% decrease
Hexane	
DDS30	0.5% increase
sol-gel	shift right ~50nm
MTES30	0.6% decrease
DDS20	1% decrease
MTES20	1.2% decrease
MTES10	1.5% decrease
DDS10	2% decrease

Error: $\pm$ 0.05% T

Figure 3: Contamination test results and corresponding visible-near IR spectra.

Because the samples coated with the DDS 30% and MTES 30% sol-gel solutions gave the best overall results in these experiment, these two compositions were selected for further testing in the Optical Maufactuing (OMAN) facility. The MTES 30% and

DDS 30% sol-gels were dip coated rather than spin coated onto the next set of test substrates because dip coating produces a more even and accurately coated sol-gel AR layer. A third set of susbstrates were dip-coated with the standard sol-gel stock solution as a control. The transmission profile was measured for each coated substrate. Because of coating adhesion problems encountered in the experiments, all three of the sol-gel solutions were diluted in a 1:1 ratio with ethanol and then filtered through a 0.2 μm membrane filter to eliminate particulate contamination.

More samples were dip coated with the newly filtered solutions. The MTES 30% coating showed slight spottiness, while the DDS 30% coating uniformity was good in the center of the substrate but poor around the edges. This was concluded to be a substrate-cleaning problem, so the substrates used in further experiments were cleaned very thoroughly. These samples were then used for contamination testing and were compared to the contamination test results from optics coated with sol-gel created by OMAN staff. The results were very similar in that the sol-gel coated optics with MTES or DDS in it were more contaminant resistant than those coated with the standard sol-gel.

Each of the three sol-gel solutions (standard TEOS-based, DDS 30%, and MTES 30%) were coated on 2" fused silica substrates. These samples were subjected to a 1-on-1 laser induced damage test. In this test the optic is irradiated at separate sites with increasing energy. The results are shown below in Table 2.

Sample	%T	%R	%T + %R	Laser Damage Threshold (J/cm^2, 1-on-1)
DDS 30*	99.91	0.03	99.94	18.97 $\pm$ 0.66
MTES 30*	99.33	0.58	99.91	19.93 $\pm$ 0.46
Std. Sol-Gel	99.65	0.31	99.96	19.43 $\pm$ 1.16

* Used as is- no purification

Table 2: Laser induced damage results on co-hydrolyzed sol-gel coatings (351 nm, 0.5 ns pulse).

There was very little discrepancy between the results of the three samples. The original sol-gel showed maximum Transmittance + Reflectance at 99.96%, yet the MTES and DDS samples were less than 0.05% away from that of the sol-gel. The MTES and DDS co-hydrolyzed sol-gels show equivalent damage thresholds to the standard TEOS-based sol gel even though the MTES and DDS were used as-supplied from the vendor with no special additional purification. Even higher damage thresholds may be possible if the MTES and DDS went through additional purification.

4. Conclusion

Test results showed that overall, MTES 30% and DDS 30% fared just as well or better in contamination tests and laser damage testing as the original sol-gel. Further research may be conducted to develop a coating that would provide a universal protection against any contaminants in the laser bay. Over time, the contaminants in the laser bay may change, so complete protection against all contaminants is more beneficial than protection against a select few. Different concentrations of MTES and DDS will be experimented with, along with purification techniques of these two chemicals before they are added to the sol-gel solution. If this experiment continues to be successful, it will

ultimately reduce or eliminate the need for frequent changing of the laser systems optics to achieve maximum system performance.

References:

(1)   Y. Xu *et a*l 1, L. Zhang, D. Wu, Y. H. Sun, Z. X. Huang, X. D. Jiang, X. F. Wei, Z. H. Li, B. Z. Dong, and Z. H. Wu, "Durable Sol-Gel Antireflective Films with High Laser–Induced Damage Thresholds for Inertial Confinement Fusion", J. Opt. Soc. Am. B, Vol. 22, No. 4, April 2005, pp. 905-912.

Superconducting Electronics for the ICF Environment

Martin Wegman

Advisor: Dr. William Donaldson

Abstract

This project addresses the steps necessary to validate the performance of
superconducting circuits in an ICF environment. Output signals from diagnostics are
often acquired with an oscilloscope. For collecting data on OMEGA a computer program
was created to design a circuit board for coupling high-frequency signals into a 5-mm-
square Nb superconducting device. Then a superconducting frequency-dividing chip,
obtained from HYPRES Inc., was attached to the board with wire bonds. The device was
inserted into a cryostat and cooled to 4.2 K. The correct electrical biasing for stable chip
operation was determined. A computer program was designed to facilitate
communication between the OMEGA Intercommunication Protocol (OIP) Server,
Labview, the hardware timing system (HTS) and the Tektronics oscilloscope. All of these
pieces were integrated to do on-shot acquisition. Further research will involve testing the
level of irradiation hardness of the circuit in the OMEGA Target Bay.

I. Introduction

In inertial confinement fusion (ICF), deuterium and tritium nuclei fuse to produce
helium nuclei and energetic neutrons. The OMEGA laser is capable of producing up to

10^{14} neutrons in 250 ps on a single shot.[1] Each neutron has a kinetic energy of 14.1 MeV. Even though they are weakly interacting, at these levels the irradiation from these neutrons can cause severe background noise or damage in semiconducting devices.[2-3]

It is difficult to shield electronic circuits from these neutrons; a concrete wall several feet thick is needed to reduce the flux by about a factor of 1000. Other standard solutions have failed to alleviate the problem. Shielding with hydrogen-rich material leads to spatial and weight concerns. Also, the alternative acquisition medium, conventional film results in a slow cycle time and a poor signal to noise ratio. Hardened
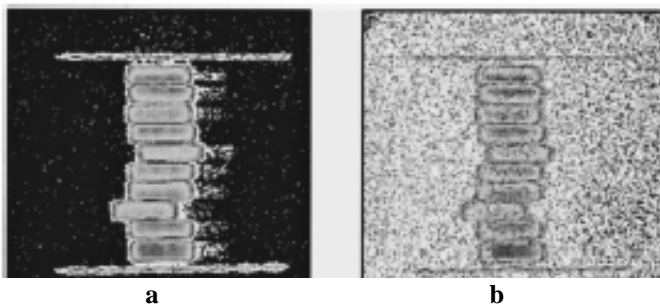
a   **b**
Figure 1- Images from a CCD camera located in the OMEGA Target Chamber; (a) a low yield shot, (b) a high yield shot[1]

semiconductors are expensive and in addition are prone to data loss. The result is that high-yield shots on OMEGA and other ICF systems may either require the devices to be turned off or the collected data may be severely compromised (see Figure 1).

A promising solution is to employ superconducting circuits, which are naturally radiation hard. Radiation-generated, free electrons become additional carriers in superconducting circuits, but, in contrast to semiconductors, do not add to the conductivity. The question remains how neutrons will affect Cooper pairs.

A Cooper pair has a very fast recovery (18 ps) should a neutron break it apart. If the neutron were to deposit its energy into the superconducting material then there would be a possibility that the material may become non-superconducting.

This project addresses the steps necessary to validate the performance of superconducting circuits in an ICF environment. This project is the first known test of a Niobium superconducting circuit in an environment with a onetime, instantaneous flux of neutrons exceeding 10^{10} within 250ps.

II. Experiment

A superconducting frequency dividing chip was obtained from HYPRES Inc.[4] The chip divides the input frequency by 2^{13}. The circuit is made of Nb with Mo Josephson junctions and a SiO_2 insulator. The pads are Ag with Ti and Pt beneath in a silicon substrate. The chip was measured to be 5,070 microns square. There are two rows of pads on all four sides. The inner square is made of 5 pads

Figure 2- A diagram of the Nb circuit to be tested.

and functions as the ground while the outer row of 6 pads functions as input/output and bias lines. The ground pads are separated by 200 microns each while the outside pads are separated by 275 microns each (see Figure 2). There are two identically functioning sides to the chip.

A circuit board with coplanar waveguides was designed to match the 50 ohm impedance of high frequency data acquisition systems and to couple high frequency

signals. A coplanar waveguide has a middle, signal-carrying conductor surrounded by two ground strips. The thicknesses of the board and of the strips were 0.06 inches and 0.001 inches, respectively. A PV wave program was created to calculate the impedance using three variables: the size of the middle strip, the size of the two side strips, and the distance separating the strips. The program finds the best size (closest impedance to 50

a

b
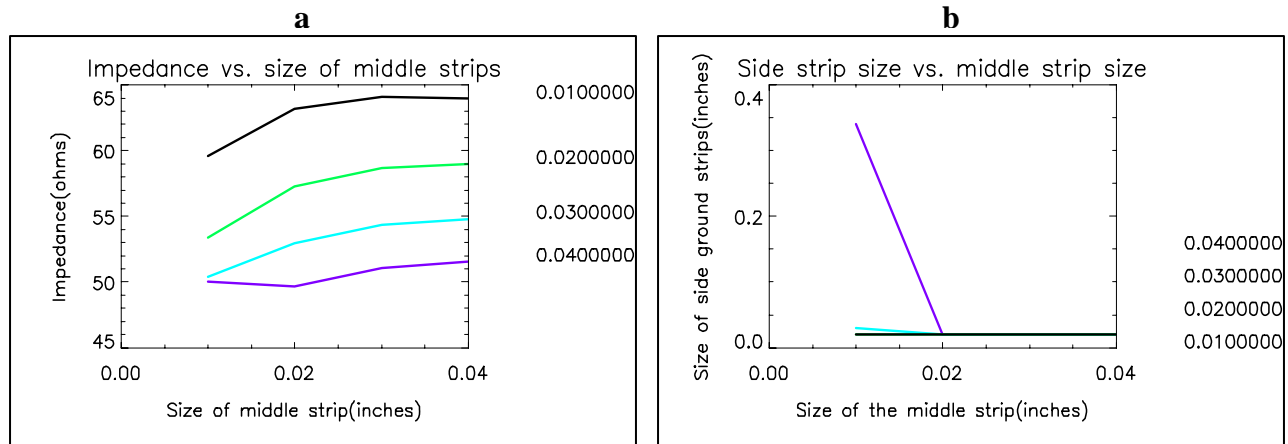
Figure 3- The impedance of the waveguide is a function of the geometry. The impedance will increase with the width of the line (a). The width of the outside lines decreased as the center line increased (b).

ohms) for the side (ground) wires based on the given gap and the size of middle wire. The data is displayed in the two plots of Figure 3. In Figure 3a, the impedance is plotted as a function of the width of the middle wire for four different gap sizes. In Figure 3b, the width of the side ground strips is plotted as a function of the width of the middle wire with impedances as shown in Figure 3a for the four different gap sizes. From Figure 3, the widths of the high and medium frequency strips were determined. The size of the middle (ground) strip was 0.02 or 0.03 inches when the size of the side frequency strips was 0.05 and 0.03 inches respectively, with a gap of 0.05 inches. With a gap of 0.06 inches, the size of the middle strip could be expanded to 0.04 inches with side strips of

4

0.05 inches. The ground lines and bias lines were made to be 0.03 inches wide each.

Using IsoPro, a circuit board was mapped and milled (see Figure 4).
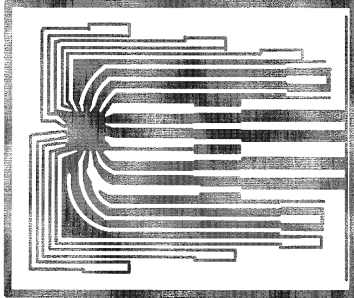
Figure 4- Circuit board design for connecting the Nb superconducting chip.

Using a West Bond wire-bonder, bonds were made with Al wire between the respective leads and pads. The machine used was located in the Advanced Integrated Circuits Laboratory in the Computer Science Building at the University of Rochester. The settings for bonding to the copper board were Power: 2.9 grams and Time: 4.5 ms and the setting for the Au pad was Power: 3.7 grams and Time: 4.1 ms.

The correct electrical biasing for stable chip operation was determined. To achieve an input bias of 5 mA, a 9V power source was placed in series with an 1800 ohm resistor. For the correct output bias with 1.4 mA, a different 9V power source was placed in series with a 430 ohm resistor. Finally, for a 21mA counter bias, a 9V source was placed in series with a 6,000 ohm resistor. The input wave from a Coherent 7600 Mode Locker 38 MHz frequency generator was modified (25 mV offset) using a bias tee with a DC power supply to produce an Rf input with a bias of 0 – 1 mA (side A). A series of attenuators 20dB, 10dB, 8dB, 6dB and 3dB were used in series to reduce the voltage of the 38 MHz signal.

To determine the correct output setup, the output was run first through a frequency filter and then through a quad amplifier into a Tektronics TDS 6604 fast

oscilloscope. The OMEGA hardware timing system was then attached to the oscilloscope. A laptop was attached to the oscilloscope via a GPIB connection.

A Labview/ Visual Basic computer program was designed to communicate with the OMEGA Intercommunication Protocol (OIP) Server, Labview, the hardware timing system (HTS) and the Tektronics oscilloscope. Calling a previously written Visual Basic program which waits for events from the OIP Server, the Labview program can trigger and acquire waveform data from the oscilloscope and store the data on the PC during the OMEGA shot. The program can handle all OMEGA events and has a WatchDog timer. It was tested using the OIP imitation program and with the actual OIP server.

All of these pieces were integrated to do on-shot acquisition. The circuit board was mounted in a brass, cylindrical cryostat one foot in diameter and approximately 3 feet tall. The bottom can be removed for mounting the board and connecting the bias, input and output lines. A conductive grease was spread beneath the board and all wires attaching to the board were heat sunk or attached to the inside of the cryostat before being attached to the board.

A vacuum reduces the pressure inside the cryostat to 20 mTorr. Then the outer chamber is cooled to ~70 K with liquid nitrogen. A half cup full of nitrogen is added to the inner chamber to help clear out water vapor. After this boils, liquid helium is added so that the circuit is at its superconducting temperature, 4.2 K.

Precautions were taken to shield all exposed wires from EMI with reflective aluminum wire wrap. Several ground wires were run from the cryostat itself.

The experimental setup includes placing the cryostat in the Target Bay on a pedestal (~one meter above the floor) in the direct line (not behind other sensory equipment) of the target chamber center (TCC). The laptop and scope will be placed in La Cave, below the Target Bay.

III. Analysis

Several issues are involved in planning the experimental setup. First and very important, data acquisition must occur on shot. Second, correct trigger timing must occur for the oscilloscope with the HTS. Finally, there can be no disruption of the principal OMEGA experiments.

The goal is to analyze the period of the counter output recorded during the neutron flux (OMEGA firing). The 38 MHz frequency should be divided by 2^{13} to produce an output of ~4638 Hz. This converts to an output with a peak every 216 us. The acquired waveform will be in the 4000 us range, enough to capture 16 full periods and analyze the output's wavelengths during the shot. If a neutron were to interrupt the circuit, the period would decrease thereby resulting in a higher frequency than expected.

Several control tests will validate the above results. First, a bit error rate (BER) test will be performed. This involves testing the circuit in a non-neutron/low-neutron environment to determine random error. The circuit will be placed 180 cm from TCC or

in La Cave. It will be given a test pattern to read during OMEGA firing. Analyzing the data, the number of misread bits will characterize the probability of error. After the high neutron yield shot another BER test will be performed to assess whether any permanent damage occurs from neutron degradation. This cycle will then be repeated several times.

Theoretical calculations were performed to assess the viability of superconducting circuits. In one calculation, it was determined that to raise the temperature (from 4.3 K) of all the Nb (3.23E-10 g) in the circuit to its non-superconducting temperature (9.2 K) would require 200 (18 MeV) neutrons. So for a circuit temperature to be raised equal to T_c a yield of 1.68E+10 neutrons from a DT shot is required when the device is located 10 cm from TCC. At 280 cm from TCC (experimental location on the pedestal), 3.30E+14 neutrons from a DT reaction would raise the temperature to 9.2 K. In La Cave, a yield of 1.42E+15 neutrons should result in the same disruption. Note that the preceding calculations were based on the assumption that the neutrons' quantum efficiencies of the energy deposition are 100%, which is unlikely. So, it is unlikely that the superconducting circuit will be disrupted.

These calculations are based on the assumption that the whole circuit has to be heated, when, in fact, only a single segment of the RSFC circuit needs to be made non superconducting to allow for disruption in the quantized flux stored.

IV. Conclusion

Data obtained using semiconductors and their alternatives have been compromised in high neutron-yield environments.

In this project, an experimental setup was designed to test the viability of superconducting circuits. A circuit board was created, and the correct electrical bias was determined. A computer program was designed to facilitate communication between the OMEGA Server, a fast oscilloscope and the hardware timing system. Additionally, theoretical calculations give evidence of the circuit's viability.

Further tests on OMEGA will hopefully support these findings.

V. References

[1] P.A. Jaanimagi, R. Boni, and R. L. Keck, "Neutron-induced background in charge-coupled device dectors", Review of Scientific Instruments, Vol. 72, No. 1, (2001).

[2] N. Rando, A. Poelaert, R. den Hartog, D. Lumb, P. Verhoeve, A. Peacock, B. Nickson, L. Adams, W. Hajdas, "Proton induced radiation damage on high quality Superconducting Tunnel Junction Detectors", Nuclear Instruments And Methods A 394 (1997) 173-179.

[3] S. E. King, R. Magno, and W. G. Maisch, "Radiation Damage Assessment Of Nb Tunnel Junction Devices", IEEE Transactions on Nuclear Science, Vol. 38, No. 6, (1991).

[4] S. Sarwan, D. Gupta, A. F. Kirichenko, T. Oku, C. Otani, H. Sato, and H. Shimizu, "High-sensitivity high-resolution dual-function signal and time digitizer", Applied Physics Letters, Vol. 80, No. 11, (2002).

VI. Acknowledgments

Categorization and Analysis of Defects in Cryogenic Laser Fusion Targets

Lauren M. Weiss

Brighton High School
Rochester, NY

Adviser: Luke M. Elasky

Abstract

Laser fusion is a technology under development that will use the fusion of hydrogen isotopes as a power source. It uses laser energy to irradiate a small, cryogenic target containing deuterium ice, causing the deuterium in the target to compress to extreme densities and fuse. In the process of freezing the deuterium, defects can form. This work focused on defects, which are localized nonuniformities in the ice that can hinder fusion reactions. Defects in a variety of targets were catalogued using shadowgraphy, a type of imaging. Categorization was based on the defect's size, shape, depth in the ice layer, and light intensity pattern. Principal defect categories include bumps, cracks, double defects, and ghost rings. The locations of the defects were analyzed to determine whether environmental factors in the layering sphere (the spherical chamber in which the ice layer is formed) were causing the defects. This analysis showed that 1) many bumps and closed cracks occur in diametrically opposite pairs, and 2) the defects known as ghost rings occur in a specific location relative to glue spots (which are used to mount the targets) on one side of the layering sphere, suggesting that the glue spots cause these defects. The glue spots are most likely heated by nearby bright spots in the layering sphere because the defects only occur in a certain region.

1. Introduction

1.1 Cryogenic Targets

To achieve laser fusion, it is necessary to uniformly compress as much deuterium fuel as possible to a very high density. To maximize the amount of fuel, cryogenic targets are used (see Fig. 1a). Cryogenic targets are preferable to room-temperature

targets because solid deuterium is denser than gaseous deuterium, so more deuterium is available for fusion in a cryogenic target.

Cryogenic targets are formed by filling a plastic shell with 1000 atm of deuterium gas and placing it in an apparatus called the layering sphere (see Fig. 1b). The layering sphere is maintained just below the deuterium triple point, which is 18.73 K. When the target has frozen, mid-infrared irradiation bounces around the inside of the layering sphere to heat the target uniformly. Because thick regions of ice absorb more IR radiation, the deuterium in these regions heats up, sublimes, and then condenses in colder regions of the target. This continues until the deuterium ice layer achieves thermal equilibrium, a condition that theoretically results in a uniform ice layer.[1]
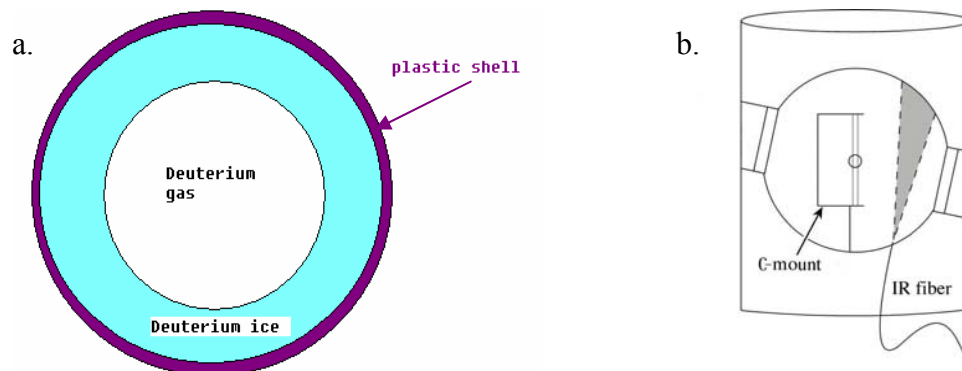
Figure 1. (a) Cross-section of a cryogenic target. The diameter of the target is ~900 μm, the ice is ~100 μm thick, and the plastic shell is 3 μm thick. **(b)** A cross-section of the layering sphere. The tiny circle in the center is the target, which is suspended from four strands of spider silk which are attached to a C-mount. The IR fiber provides internal heating to create a uniform temperature within the layering sphere.

In order for fusion reactions to occur, the target must compress uniformly. By Newton's Law, F=ma, the pressure from the plasma formed by laser irradiation on the target's plastic shell will accelerate thin regions of ice toward the target's center faster than thick regions, because thin regions are less massive. Efficient fusion relies on as much fuel as possible reaching the center of the target simultaneously, so any time lag

decreases the amount of fuel available for fusion and the maximum compression that can be achieved, and thus the number of fusion reactions. Therefore, the ice layer must be uniform to maximize energy output.

There are two general types of nonuniformity in the ice layer. One is an asymmetry, in which the change of the ice thickness around the target is gradual, like a slope in a road. The other is a defect, which is a localized nonuniformity in the ice layer, like a pothole. Although past research has studied asymmetries[2,3], little work has been done to analyze defects because of their complexity. To understand why defects are relatively difficult to interpret, one must understand shadowgraphy.

1.2 Shadowgraphy

Targets are characterized using shadowgraphy, an imaging process that involves backlighting the target to produce an image (see Fig. 2). Collimated light starts behind the target, travels through the target, is collected by a lens in front of the target, and is imaged onto a CCD. Light that is collected in the optics appears to come from the plane through the target's center (the object plane), so the light intensity patterns in the image correspond to the light intensity patterns in that plane. Light intensity is scaled from black to white, with black corresponding to no light in that area of the object plane, and white corresponding to very high intensity light.

Two types of rays are collected: A-rays and B-rays. A-rays pass through a large central region of the target, whereas B-rays refract off the inner ice surface. When the paths of B-rays are traced back to the object plane, they appear to come from a narrow

region known as the "bright ring." A defect can alter or obstruct either type of ray, as illustrated in Fig. 2b.
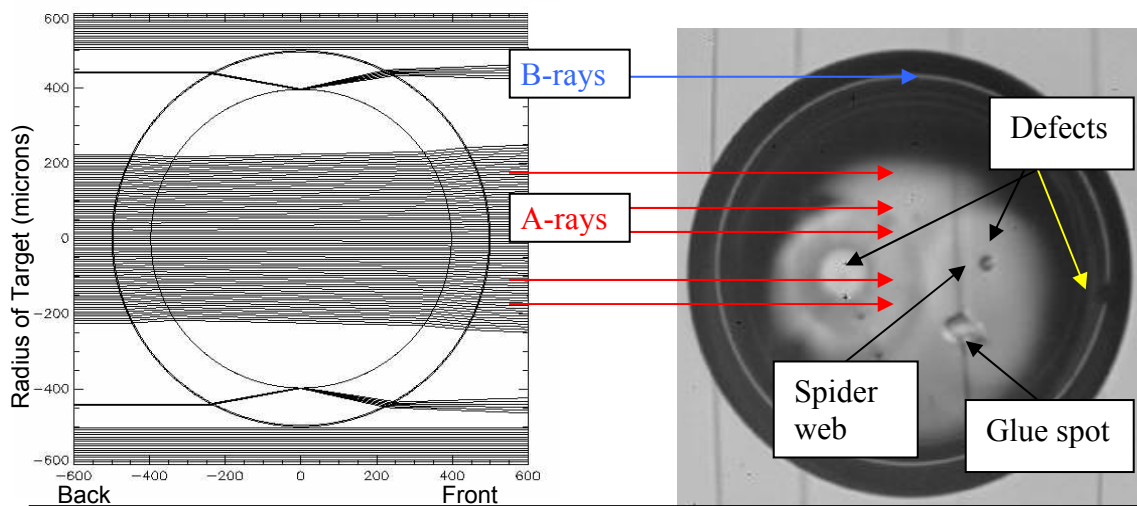
Figure 2. (**a**) Side view of the target showing light rays traveling from the back of the target to the front. A-rays pass through the center of the target; B-rays bounce once off the inner ice surface. The window scale is from -600 to 600 μm. (**b**) A typical shadowgram. The outermost black circle is a silhouette of the target. The spider web and glue spots that suspend the target are visible. The light central area of the shadowgram is from the A-rays and shows two circular defects. The thin white ring near the edge of the target is the bright ring produced by the B-rays and also indicates a defect.

To understand what causes defects, it is necessary to know where they form. Therefore, the defect's origin is mapped with respect to a coordinate system embedded in the target using standard spherical coordinates, with θ measuring the angle from the vertical z-axis and Φ measuring the angle about the z-axis.

In order to find and categorize all of the defects on a target, multiple shadowgrams are taken from different angles by rotating the target about its vertical axis. Each target is viewed by two cameras, at θ = 78° and 63°, which take 25 images each. This creates a shadowgram for every 15° of rotation in each camera's image set.

1.3 Defect Categorization

Scientists have studied cryogenic targets extensively using the bright ring to analyze ice surface nonuniformities and simulated defects.[2,3,4] Although defects have always been visible in the A-rays, no work had been done to understand their nature because there was no way to determine the depths of defects in the ice layer until a program known as Liger was developed.[5] Liger enables the depth of a defect to be calculated, making it possible to include this information in the characterization of defects. In Ref. 5, Liger was used to characterize a single defect in a single target.

This work used Liger and my own observations to systematically investigate defects. Twenty-six defects in eleven targets were analyzed. Many defects had similar physical properties. These defects were categorized. The most important factors in categorizing a defect were the defect's shape, size, light intensity pattern, depth in the ice, and the changes produced in the bright ring when the defect was on the side of the target.

Most of the defects that were examined were categorized as bumps, open cracks, closed cracks, ghost rings, or double defects, all of which are discussed in detail in the following sections.

**2. Bumps**

2.1 Observations

Bumps are the round, smooth defects pictured in Fig. 3. Bumps usually range from 150 to 200 microns in diameter. They appear gray on the front of the target and white on the back. This allows us to conclude that they are convex structures on the inner ice surface, as explained in Section 2.2.
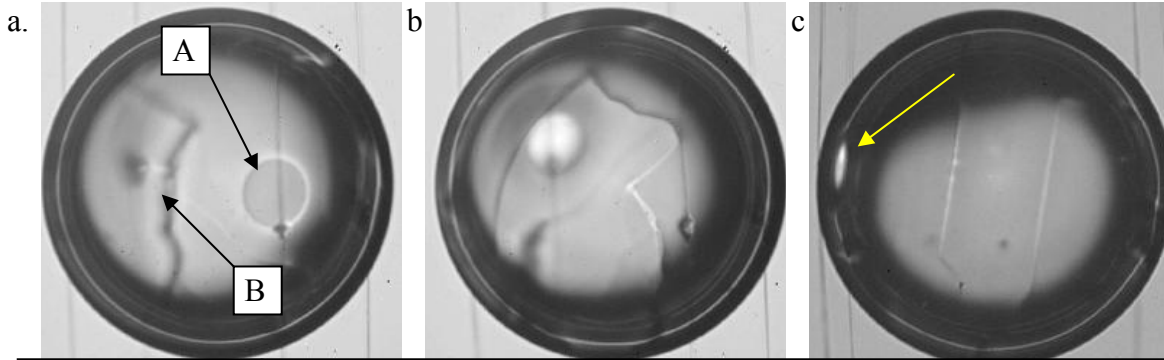
Figure 3. Three views of a target containing a circular defect (a bump) [A] and an open crack [B]. (**a**) On the front of the target, the bump is a gray spot surrounded by a thin white ring. (**b**) On the back of the target, the bump is a white spot surrounded by a thin gray ring. (**c**) The bump forms a rice-grain shaped region of high-intensity light in the bright ring (indicated by the arrow) when the bump is on the left side of the target. Target: Cryo-2041-315; Shadowgram sets: 2x16817, 2y16817; Date: 2004-04.

2.2 Liger Analysis

Liger uses both A-rays and B-rays to approximate the depth of a defect in the ice. Liger displays 50 shadowgrams in sequence. A user examines each shadowgram and flags points around the perimeter of the defect to form a polygon (see Fig. 4). The program establishes a grid of pixels in the central region of the shadowgram. The user clicks once in the area that is not part of the defect, marking the rays that go through it as "good" A-rays. The user also flags the abnormal arcs in the bright ring. The paths that these rays would have followed if they were not blocked are known as "bad" B-rays.
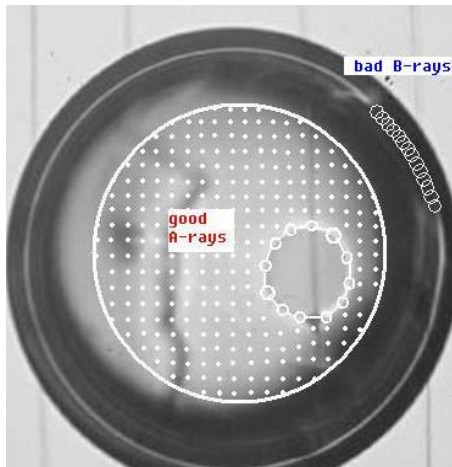
Figure 4. User's selection of good A-rays and bad B-rays from Fig. 3a. The user flags points indicated by the circles; the white dots represent the good A-rays (although the program traces more rays than those shown).

Liger calculates the paths of the good A-rays and bad B-rays and stores the paths in a 3-D matrix. By counting the number of rays that pass through each cell, Liger constructs a 3-D model of the target. The user views the model in horizontal slices similar to those of a CAT scan. A Liger analysis of a bump defect is shown in Fig. 5. The intensity is scaled so that cells that contain only good A-rays are white, cells that contain zero good A-rays are black, and cells that contain some good A-rays are shades of gray. The defect lies within the black area in the upper left of Fig. 5a. However, it could be at any depth within this area.

To indicate the depth of the defect, Liger incorporates the paths of the bad B-rays into the 3-D model. The intersection of bad B-rays with cells that contained zero good A-rays is shown in Fig. 5b. This intersection maps the approximate depth of the defect because the B-rays and A-rays that were blocked followed different paths through the ice. Figure 5b indicates that the defect is on the inner ice surface.
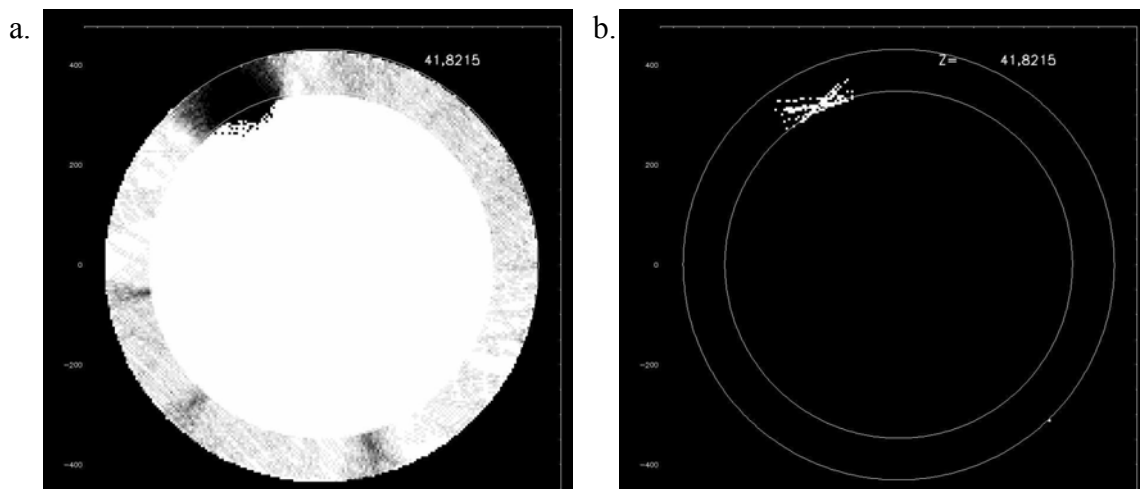
Figure 5. (**a**) Liger analysis of a bump defect using only A-rays, in the plane $z = 42$ μm. The white areas correspond to the paths of good A-rays. The dark region near the upper left indicates the general location of the defect. (**b**) Analysis including B-rays, showing the intersection of the dark region of (a) and the bad B-rays. This narrows the possible region in which the defect could be. The window scale is from -400 to 400 μm.

Although it can locate a defect, Liger cannot determine whether the defect is a concave region, a convex region, or a region that contains impurities; it merely shows that the region blocked or scattered light. Yet, we can determine whether a round defect is convex or concave based on its light intensity pattern,[6] as indicated in Fig. 6.

When light goes through convex defects on the back, it is refracted inwards, as indicated in Fig. 6a. The apparent area of the defect is smaller than its true area, and so the defect appears brighter. A narrow region of low-intensity light surrounds the defect because the rays that ordinarily would have gone through this area went through the small, bright region instead. The resulting shadowgram is seen in Fig. 3b. When the convex defect is viewed on the front, the refracted rays projected back to the object plane appear to come from a larger area, and so the defect appears darker. A narrow region of high-intensity light surrounds the defect because the rays that extend beyond the true area of the defect enter regions that already contain rays, thus increasing the concentration of rays there (see Fig. 3a). Concave defects disperse light, and so they create the reverse of the convex patterns. Ray-traces similar to those shown in Fig. 6 indicate that a bump that is 3 μm high produces an intensity pattern similar to those of typical bump defects.[7]
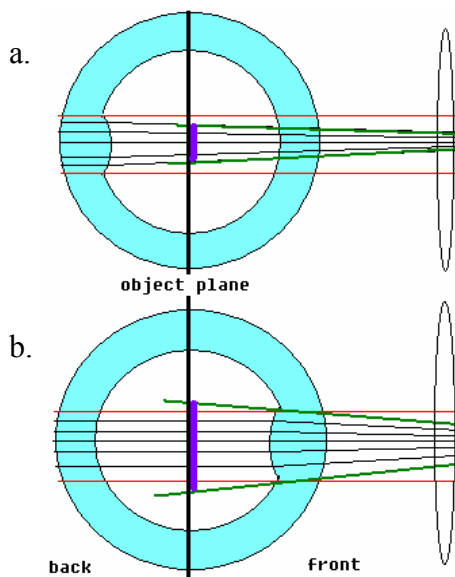

Figure 6. Side view of ray paths through a bump. (**a**) Light from the back of the target is refracted by the bump. As the green rays indicate, it passes through an area on the object plane (indicated in purple) that is smaller than the true area of the defect. (**b**) Light that passes through a convex defect on the front of the target appears to come from an area larger than the true area of the defect when it is projected back to the object plane.

3. Open Cracks

3.1 Observations

Open cracks are long and narrow, as shown in Fig. 3. They are narrower than 20 microns and longer than 200 microns. Although we cannot determine the concavity of open cracks, we assume that they are cracks because the ice contracts when the target is cooled to ~1K below its triple point.

Because open cracks are so narrow, they cause limited interference to the rays that form the bright ring. Cracks that run mostly vertically, like the one in Fig. 3, will make large voids in the bright ring, but only when they are lined up exactly on the side of the target. Cracks that run horizontally will only make a small break in the bright ring, but this break will show up at more angles of target rotation.

z = 219 µm

z = 126 µm

z = 82 µm

z = -190 µm
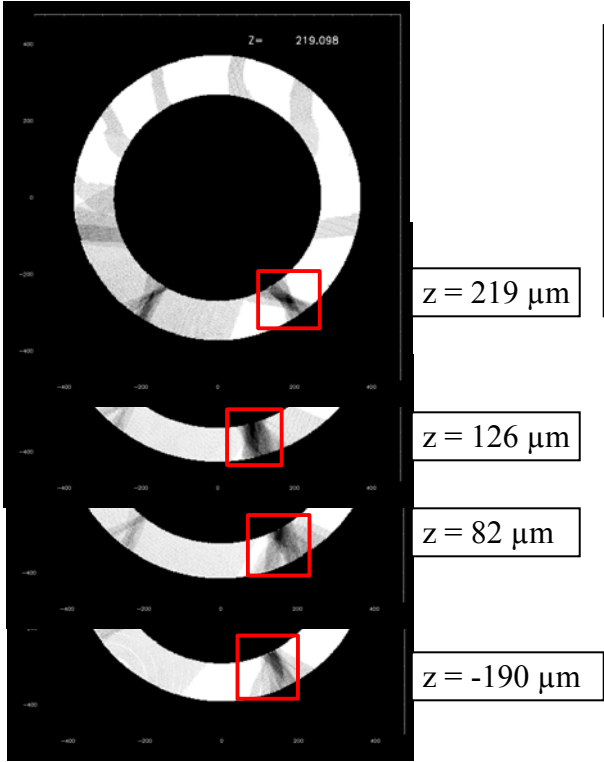
Figure 7. Liger analysis of the open crack shown in Fig. 3. Slices are taken at different heights in the target. The red boxes indicate portions of the crack discussed in the text. Cryo-2041-315, 2y16817, 2004-04.

3.2 Liger Analysis

A Liger analysis of the open crack in the target of Fig. 3 is shown in Fig. 7. Because open cracks have limited impact on the bright ring, they are difficult to identify in the B-rays of a target. However, they are narrow enough that the combination of A-rays from different angles can resolve their depth. This can be seen in the bottom three slices of Fig. 7, in which the black regions taper as their distance from the inner ice layer increases. This indicates that the open crack occurs near the inner ice surface. Also, only a defect on the inner surface could leave the light gray shadows that fan out from the inner ice surface. These shadows occur because the defect prevents A-rays from passing through the normal ice at certain angles.

4. Closed Cracks

4.1 Observations

Closed cracks are complex cracks of polygonal structure that are generally from 100 to 400 microns in diameter. One example of a closed crack is shown in Fig. 8. Of all the defects, closed cracks vary the most in appearance; no two have the same shape. Every closed crack encountered in this work was opposite a bump, although only three of five targets that had a bump had a closed crack opposite the bump.

The Liger analysis of a closed crack is very similar to that of a bump, so it is not shown. The intersection of A-rays and B-rays shows that closed cracks are located on the inner ice surface. Liger also shows that the bump and closed crack are ~180 degrees apart, as illustrated in Fig. 8b.
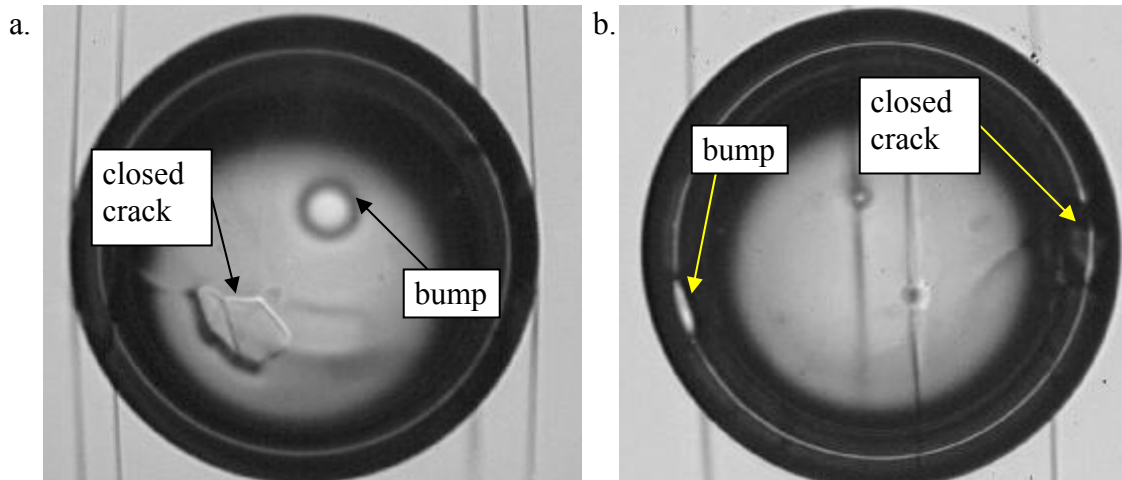
Figure 8. (**a**) A polygonal closed crack on the front of the target, viewed at Φ=340°. The closed crack is opposite a bump on the back. (**b**) The same target, with the closed crack on the right and the bump on the left, viewed at Φ=241°. The bump produces the rice-grain of light in the bright ring on the left, and the closed crack produces the void and blemish in the bright ring on the right. Cryo-2039-313; 2x15832, 2y15832; 2004-04.

4.2 Possible Explanation

The diametrically opposite positioning of the bump and the closed crack might be a result of how the deuterium ice layer is formed. To form the ice layer, the target is cooled in such a way that the liquid deuterium first crystallizes at a single point. Crystallization continues from the seed and expands around the surface of the target.

One place where a defect could form is the location of the seed crystal. Because the target would be colder there, the ice would form a thicker layer. This might cause a bump in the ice. Since the crystal surface must eventually reconvene at the polar opposite point from the seed crystal, another defect could form at the point of convergence as the crystal fronts come together. The closed crack possibly forms this way because it appears to have a crystalline structure, and it often appears to contain several overlapping features.
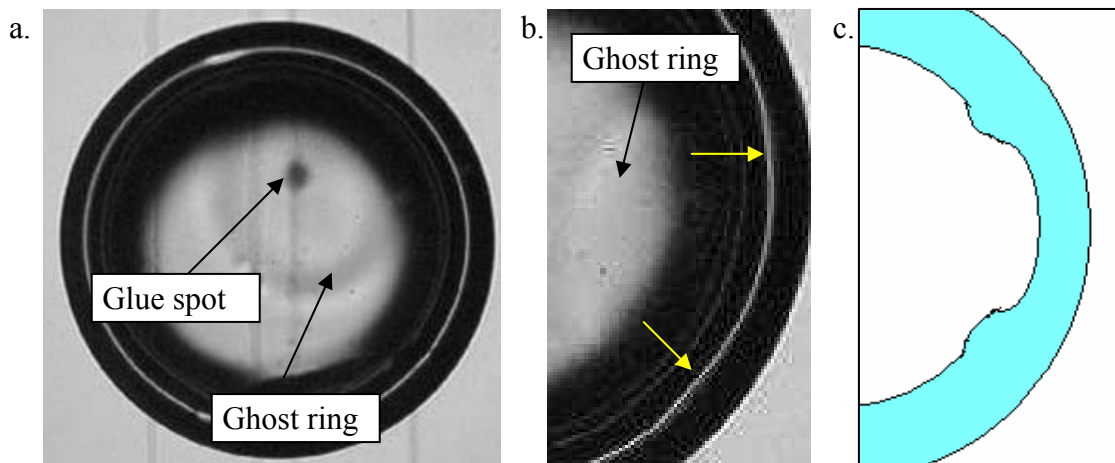
5. Ghost Rings

5.1 Observations

Ghost rings are halo-like regions that are usually centered on the glue spots used to mount the target, as shown in Fig. 9a. There are four glue spots on each target, positioned equidistantly around the equator. Ghost rings only form around or near large glue spots (~50 μm in diameter) in a certain region of the layering sphere. This region is along the equator between approximately $\Phi = 250°$ and $300°$.

The curvature of the ghost ring is very subtle because it does not create a break or void in the bright ring; it only produces a slight ripple, as shown in Fig. 9b. This perturbation is too subtle and gradual for Liger to analyze. Therefore, Liger cannot characterize ghost rings effectively.

Ghost rings on the front are dark with a white interior (see Fig. 9a), and on the back they are white with a dark interior.

Figure 9. (**a**) A ghost ring on the front of the target. The ring is dark with a bright interior. The dark spot is a glue spot. (**b**) Perturbations in the bright ring caused by the ghost ring indicated with yellow arrows. (**c**) Proposed cross-section through a ghost ring (exaggerated).

5.2 Proposed Explanation

Ghost rings appear to be formed by the glue spots at their centers. According to this model, the glue spot absorbs energy from the IR radiation and dissipates it as heat through the ice layer by conduction and thus creates a hot spot on the inner ice surface. The extra heat causes the deuterium atoms on the inner ice surface to sublimate, creating thinner ice in the region of the hot spot.[1] When the displaced deuterium atoms encounter sufficiently cold ice, they condense, forming a thick ring of ice around the hot spot.

We can infer the thickness of the ice in a target based on the radius of the bright ring.[3] Thick ice creates a small radius, whereas thin ice creates a large radius. From the variations in bright-ring radius, we can postulate a cross-section of the ghost ring (see Fig. 9c). This suggests that the ghost ring is a region of thin ice surrounded by a region of thick ice, where the thin ice is the hot spot in the middle and the thick ice is the ring.

The only glue spots that produce ghost rings are large (50 μm in diameter) and are located between $\Phi = 250°$ and $300°$. Why do ghost rings only form around these types of glue spots? A large glue spot would create a more pronounced hot region than a small glue spot because a large glue spot would absorb more IR radiation. The location of the glue spot during target freezing affects whether a ghost ring will form because the distribution of IR radiation inside the layering sphere is not completely uniform. A region of the layering sphere at $\Phi \approx 285°$ is much brighter than the rest of the layering sphere. This is because the injected IR light from the short optical fiber makes its first bounce at that location[8] (see Fig.10). Because the initial bounce is significantly brighter than other bounces, the target receives more illumination from this angle than any other angle. Therefore, a hot spot is formed on the side of the target nearest this incident

radiation. If a large glue spot is in the vicinity of the hot spot, it will absorb some of the excess radiative energy and form a ghost ring. However, the hot spot would not affect the ice in the absence of a glue spot because the ice only absorbs ~10% of the IR light, whereas the glue spot absorbs nearly all of it.
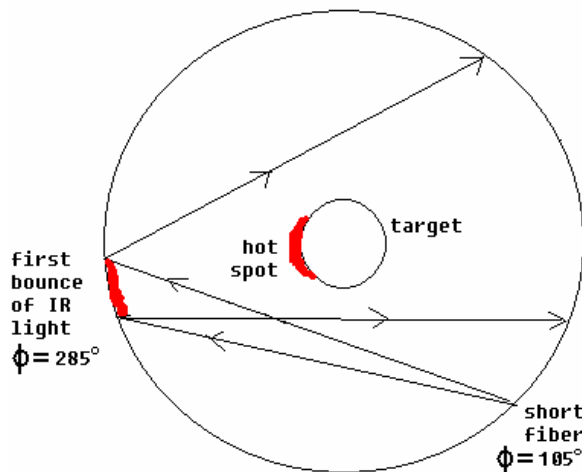
Figure 10. Schematic cross-sectional side view of the layering sphere. The short fiber at Φ=105° illuminates the inside of the sphere with mid-IR radiation. The light first bounces off the inside of the sphere at Φ = 285°, resulting in the target being preferentially heated to form the hot spot shown.

6. Double Defects

Double defects appear to be two mutually concentric defects, as shown in Figure 11. The key elements of the double defect are an inner defect of about 100-150 microns in diameter, which resembles a bump in the shadowgrams, and an outer defect of about 300-350 microns in diameter that surrounds it. On the front of the target, double defects have a gray inner defect, and the outer defect is barely visible (see Fig. 11a). On the back, double defects have a white inner defect, and the outer defect is easily visible as a dark ring (see Fig. 11b). Because the inner defect is bright on the back, it is a convex feature.
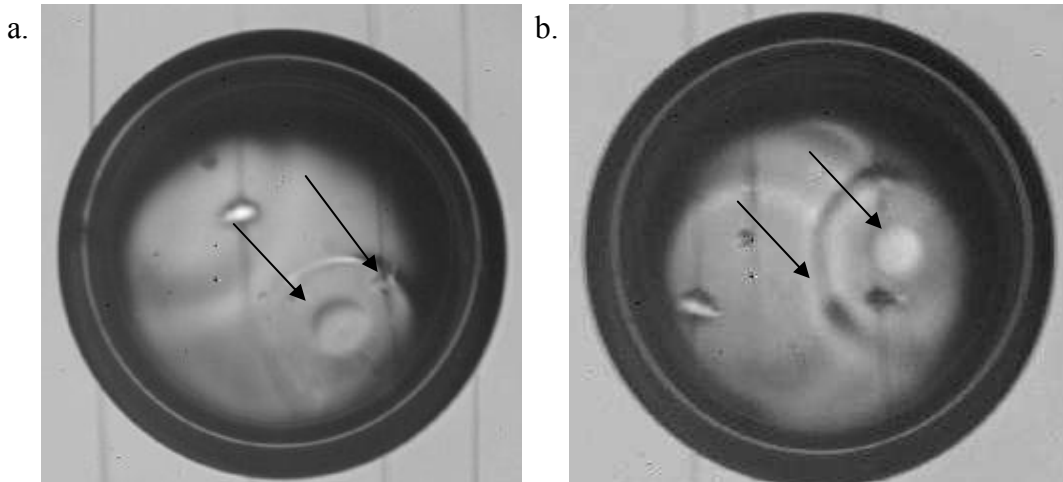
Figure 11. Two views of a double defect. **(a)** Double defect on the front of the target, with the inner and outer defects indicated with arrows. **(b)** The same double defect on the back of the target, with a bright inner area and a dark outer ring. Cryo-2036-344, 1y18730, 2004-07.
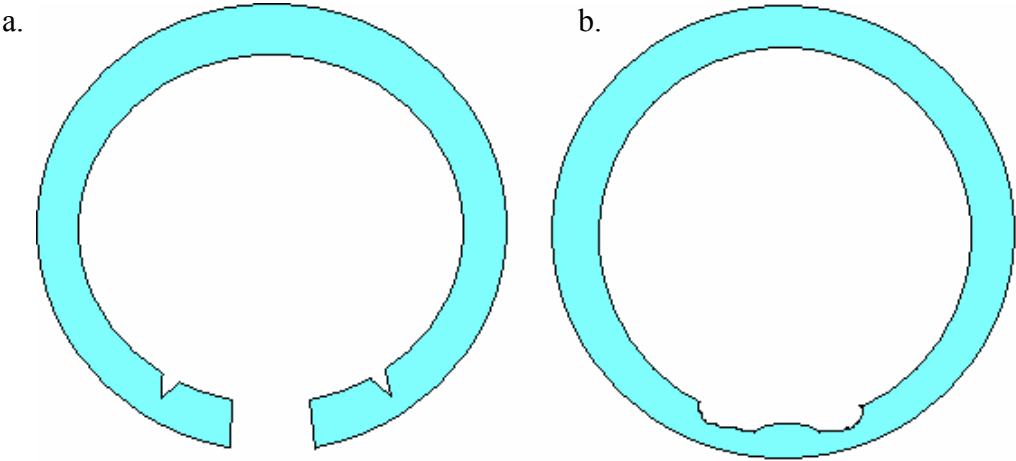
6.2 Liger Analysis

Several attempts were made to analyze double defects with Liger. An example for a target similar to that shown in Fig. 11 is shown in Fig. 12. The A-rays helped determine the size of the inner and outer defects (see Fig. 12a). However, analyses including the B-rays did not display believable depths for the inner defect. Fig. 12b shows an inner defect that appears to extend through the entire volume of the ice. However, as illustrated by the blue ray path in Fig. 12b, the apparent depth of the inner defect is probably a result of bad B-ray paths from the outer defect intersecting the inner dark region of Fig. 12a. Thus, B-rays that were blocked by the outer defect appear to have been blocked by the inner defect also. This interference of the outer defect makes it impossible for Liger to accurately characterize double defects. Because Liger and the shadowgrams do not provide sufficient information about double defects, no explanation for their origin has been proposed.
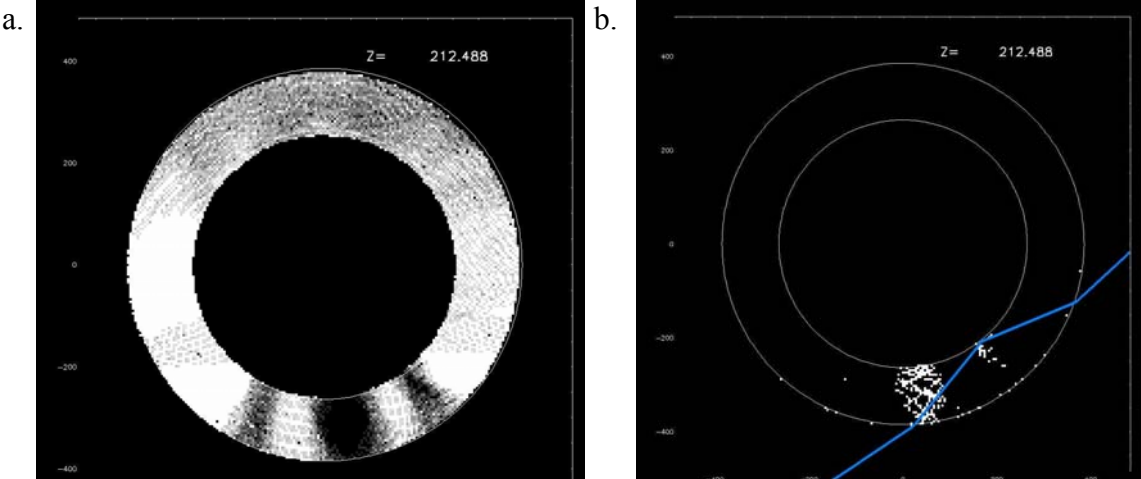
Figure 12. Liger analysis of a defect similar to that of Fig. 11, in the plane z = 212 µm. (**a**) Analysis based on the A-rays alone, showing the double defect but providing no depth information. (**b**) Intersection of paths of bad B-rays and the dark area of (a), showing an inner defect of about 100 µm in diameter that appears to extend through the full volume of the ice, surrounded by a thin, ring-shaped outer defect of about 350 µm in diameter that occurs on the inner ice surface. The blue ray path illustrates how B-rays blocked by the outer defect could appear to be blocked by the inner defect. Cryo-2044-302, 2x15633, 2y15633, 2004-04.

Because of its limitations, Liger proposes the cross-section of a double defect similar to that of Fig 13a. However, an analysis based on the light intensity pattern of the defect yields a proposed cross-section that is shown in Figure 13b.

Figure 13. (**a**) Cross-section through a double defect based on Liger analysis. (**b**) A more likely cross-section through the defect (exaggerated).

7. Summary and Conclusion

In this work, defects in cryogenic targets used for laser fusion research were categorized based on their shape, size, light intensity pattern, depth in the ice, and the fluctuations they produced in the bright ring. Many defects display similar physical properties and are thus easily categorized. The principal categories of defects are bumps, open cracks, closed cracks, ghost rings, and double defects. The results of observations of these defects are summarized in Table 1.

Defect Type	Shape	Diameter (µm)	Concavity	Location	Explanation
Bump	circular	100-200	convex	inner ice surface	coldest spot in crystal formation
Open crack	long and narrow	>200 x <20	concave	inner ice surface	contraction and splitting of cold ice
Closed crack	polygonal	100-400	?	inner ice surface	overlapping crystals
Ghost ring	ring	300-400 (ring ~50 thick)	concave interior, convex ring	inner ice surface, $250^{o}<\Phi<300^{o}$	sublimation by hot glue spot
Double defect	concentric circles	300-350 (inner 100-150)	convex interior	inner ice surface	??

Table 1. Physical properties of common defects and proposed explanations.

All of the observations in this report were made using only eleven targets and twenty-six defects. Except for the double defect, explanations were proposed for how each type of defect formed. It is vital to continue taking shadowgraphs of targets so that more targets can be characterized to test the validity of these explanations.

The only type of defect that is found to correlate with a particular region of the layering sphere is the ghost ring. All of the other defects are distributed randomly.

Bumps and cracks frequently lie on diametrically opposite points on the target. Bumps are possibly formed where a single point on the target is cooled to begin crystallization, and closed cracks could form where the crystal fronts reconvene on the

opposite side and overlap. To determine if a relationship exists between the defects'
positions and the point from which the seed crystal is formed, bumps and closed cracks
occurring in diametrically opposite pairs must be further examined, especially during the
early stages of the freezing process.

Open cracks probably form when the target is ~1K colder than its triple point,
causing the deuterium ice to contract.

Ghost rings are almost certainly formed by conductive heating from large glue
spots at their center, which absorb extra IR radiation from a bright spot in the layering
sphere at $\Phi \approx 285°$. To prevent ghost rings from forming, smaller glue spots should be
used, as they would absorb less IR energy.

By understanding how defects form, we can take measures to prevent them by
altering the process for manufacturing cryogenic targets. By eliminating defects, we can
make the fusion process more energy efficient.

8. Acknowledgements

I would like to thank Mr. Elasky for supervising and guiding my project and for
introducing me to the wonders of the cryogenics laboratory. I would also like to thank
Dr. Craxton for selecting me to participate in the High School Summer Research program
at the Laboratory for Laser Energetics and for taking personal interest in my work. I
would also like to thank the other students and staff at LLE for making my summer
enjoyable.

9. References

[1] D.N. Bittner et al., *Forming Uniform HD Layers in Shells Using Infrared Radiation,* Fusion Technology **35**, 244-249 (1999).

[2] J.A. Koch et al., *Numerical Raytrace Verification of Optical Diagnostics of Ice Surface Roughness for Inertial Confinement Fusion Experiments,* Fusion Science and Technology **43**, 55-66 (2003).

[3] J.A. Koch et al. *Quantitative Analysis of Backlit Shadowgraphy as a Diagnostic of Hydrogen Ice Surface Quality in ICF Capsules,* Fusion Technology **38**, 123-131 (2000).

[4] J. Sater, D. Bittner. *Shadowgraphy and Spherical Capsules,* General Atomics Report GA-A23240 **5**, 5-12 (1999).

[5] Brewington, Bruce. *3-D Characterization of Deuterium Ice-Layer Imperfections in Cryogenic Inertial Confinement Fusion Targets,* 2004 Summer High School Research Program for High School Juniors, Laboratory for Laser Energetics **337** (March 2005).

[6] Edgell, Dana, Laboratory for Laser Energetics, personal communication (2005).

[7] Brewington, Bruce, *Computer Simulation of Shadowgraphy,* unpublished report, Laboratory for Laser Energetics (2005).

[8] Elasky, Luke, Laboratory for Laser Energetics, personal communication (2005).

Analysis of inner ice surface perturbations using bright ring characterization

Rosie Wu

Brighton High School
Rochester, NY

Advisor: Dr. Dana Edgell

Laboratory for Laser Energetics
University of Rochester
Rochester, NY

Abstract

The uniform implosion of cryogenic targets is imperative to a successful fusion reaction. It is necessary to analyze the inner ice surface to an extremely precise degree as tiny imperfections on the surface of the target grow during the course of an implosion. When a shadowgraphic target is viewed with a CCD camera, it exhibits a bright ring, which can be used to estimate the radius of the inner ice surface. However, when comparing the actual surface radius with the experimental radius (determined according to the bright ring using only one view of the bright ring), discrepancies of up to 1 micron are observed. A program was devised that averaged two opposite views of the bright ring, resulting in a difference of less than 0.2 microns. Unfortunately, as the two cameras on the actual OMEGA system are situated at 12.6 and 22.6 degrees above the horizontal, it is physically impossible to observe two exact opposite views. Therefore, modifications were made to the program in order to incorporate the OMEGA system's actual design. It was found that the averaging of opposite views using a tilted camera yielded good results for modes up to n=5 (in other words, if the nonuniformities are broad and gradual).

Introduction

The purpose of the Laboratory for Laser Energetics is to perform high
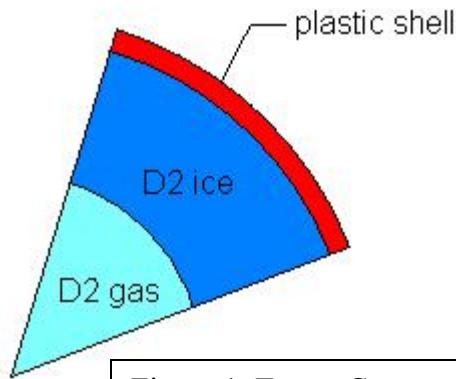

Figure 1. Target Cross-section

energy laser fusion. A small target is shot with the 60 powerful laser beams of the OMEGA laser system. As it implodes, the target generates an enormous amount of heat, which triggers a fusion reaction. A cryogenic target consists of an outer shell made of hydrocarbon plastic (~3 μm thick), a thick layer of deuterium (D2) or occasionally deuterium tritium (DT) ice (~80 μm thick, with a temperature of about 18 K) and a center of deuterium gas. The entire target has a diameter of about 900 μm.

However, for the fusion reaction to be successful, the irradiation and the inner surface of the deuterium ice layer must be uniform. To achieve uniform irradiation, the target is suspended by spider silk and the 60 laser beams impact the target from all directions. A uniform inner ice surface (the gas-ice interface) is difficult to achieve, and irregularities on the surface are problematic. Thinner sections of the ice will implode faster than thicker sections, causing an uneven implosion that will fail to generate enough heat for a fusion reaction.

Shadowgraphy

A method by which the surface of a target can be determined uses a technique called shadowgraphy. A target is backlit with a collimated light source, and the image is taken by a CCD camera.

There are three major kinds of light rays recorded by the shadowgraphs. "A" rays pass through the deuterium gas area of the target. "C" rays miss the target entirely. "B" rays, however, enter the target and reflect off the inner ice surface, exiting as a diverging group of rays that all appear to come from a single radius in the plane through the center of the target. These B rays are viewed in the shadowgraph as a bright ring (see Fig. 3). The position of this bright ring can be used to calculate the inner ice radius by using a simple theory for spherical surfaces. Therefore, nonuniformities on the bright ring can be used to calculate nonuniformities on the ice surface. If shadowgraphs of the target are taken from many different views, they can be used to create a 3-D model of the target.
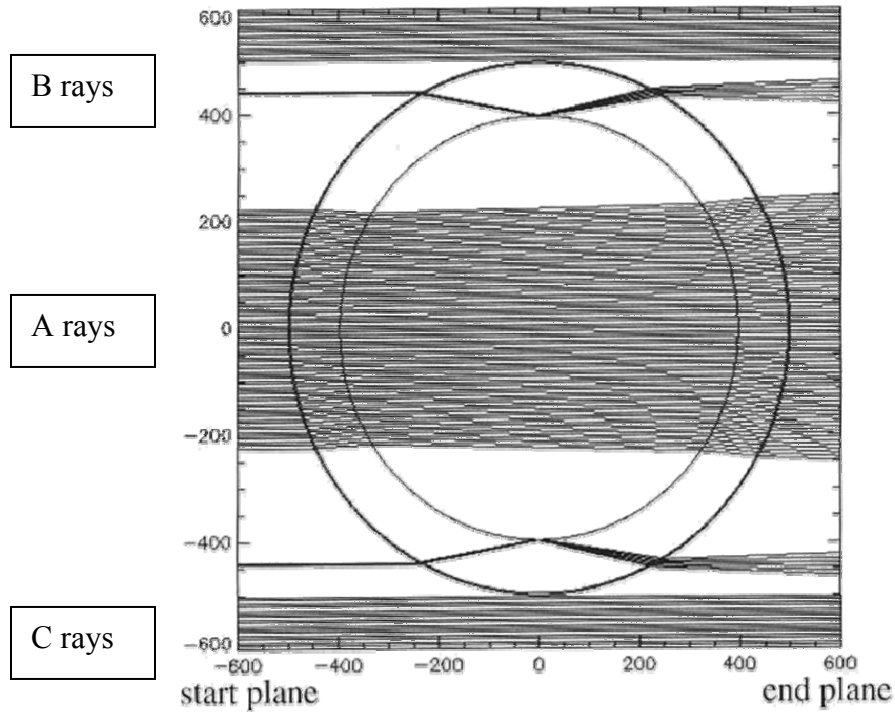
B rays

A rays

C rays

start plane   end plane

Fig. 2: A, B, and C ray paths through a cryogenic target from left to right (from Ref. 1).
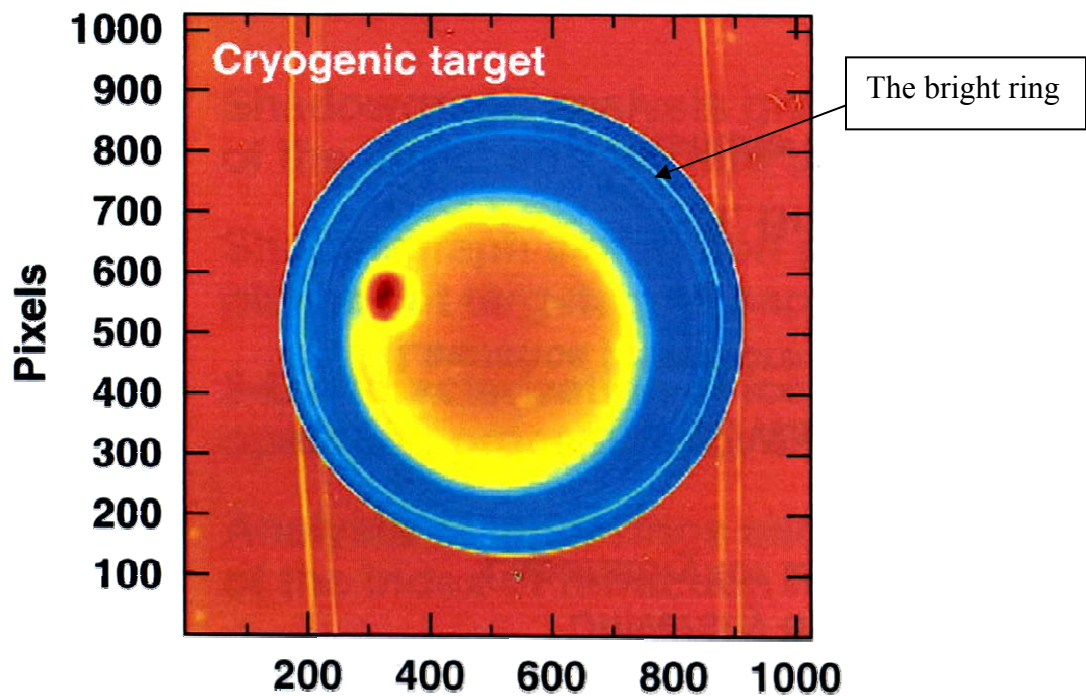

The bright ring

Fig.3: A shadowgraph showing the bright ring (from Ref. 2).

5

Noting from Fig. 2 that the emerging B rays appear to come from a single point, the radius of the bright ring is equal to the radius of the B ray that emerges exactly p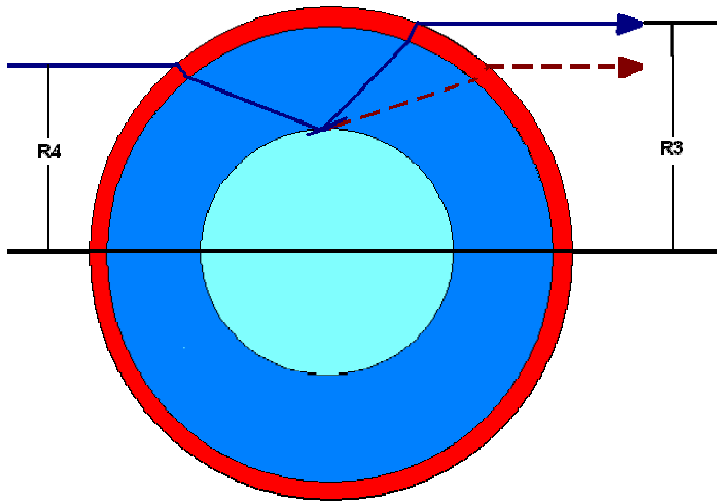arallel to the horizontal axis. Thus, the shadowgraphs taken from opposite views should be the same. However, if there are nonuniformities on the surface, the B rays will exit at a different level as shown in Fig. 4. Thus, a shadowgraph taken from one position will show a bright ring of a different radius than a shadowgraph taken from the opposite position. [2]

Fig.4: Paths of rays forming the bright ring for a uniform ice surface (dashed) and for an irregular surface (solid).

Therefore, any single view of the bright ring does not uniquely define an aspherical ice surface, and calculating the radius of the target using only a single view will yield errors of up to 1-2 microns, as can be seen in Figure 5.
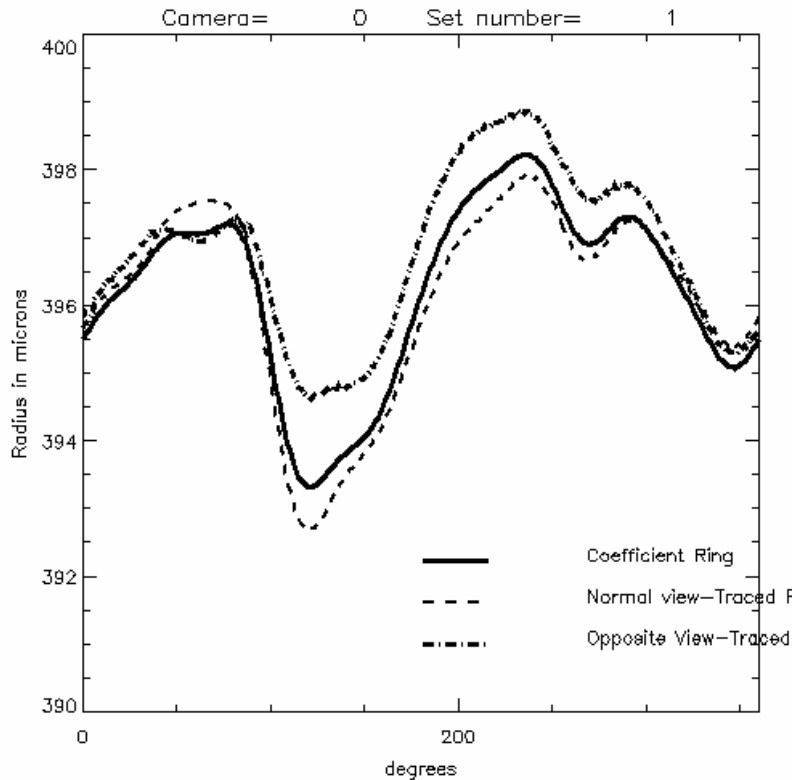
Fig. 5: The solid line represents the actual ice surface represented as a sum of spherical harmonics; the dotted lines are the calculations using only one view of the bright ring (from Ref. 2).

The Program

A program was written by Gregory Balonek [2] that traced rays through the target and found the radius of the surface.

To find the correct rays to make up the bright ring, it shoots rays through one side of the target. The first ray leaves the target on the other side with a positive angle to the direction it came in, and the program continues to launch rays at higher successively higher levels until the ray leaves the target with a negative angle. Then, the program ceases to launch rays, and interpolates to

7

find the level at which the outgoing ray is parallel to the direction it came in. The program does this for 360 degrees around each view, by one degree increments, and for fifty views of the target.

The program sets up a cube, on each side of which is a grid. The intersection of a line passing through the origin, in a given direction expressed through phi and theta, with any face of the cube can be determined. The radius of the surface can be calculated with a formula

$$R(\theta,\varphi) = \sum_{L=0}^{Lmax} \sum_{M=0}^{L} [Ac(l,m)Clm(\theta,\varphi)+As(l,m)Slm(\theta,\varphi)]$$

in which Clm's and Slm's are standard spherical harmonic functions, Ac's and As's are predetermined coefficients, and Lmax is typically 11. [1] As the radius is expressed in terms of phi and theta, it is possible to determine the radius of the surface at each point of the grid, and thus trace rays through perturbed surfaces. At each point of the grid, three radii are stored: R1 is the outer radius of the plastic shell, R2 is the radius of the plastic-ice interface, and R3 is the radius of the gas-ice interface.

The program then averages the values of R3 for views 180 degrees apart, and graphs it in comparison to the actual surface (determined through the spherical harmonic sum). The averages were found to correspond well to the true surface, with an error of about 0.2 microns.

The original program was modified to change the angle of the cameras. One camera was kept at 0 degrees, for purposes of comparison. The other camera was elevated to 12.6 degrees corresponding to an actual shadowgraphy view used on Omega. The cameras would take data at 25 positions. The slanted camera was unable to obtain opposite views, so it averaged views in a slightly different way. For example, in Figure 6, the red and blue circles are opposite views as seen by the slanted camera. (The tilt is exaggerated.) The bright ring radii at point A and point B would be averaged in order to determine the bright ring radius at point C.
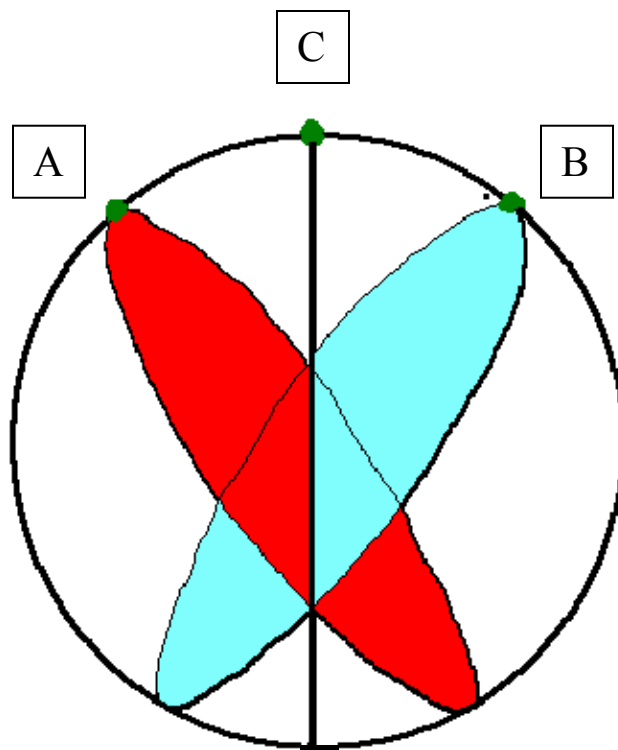

Fig. 6: The blue and red circles are the exaggerated views of the target taken 180 degrees apart seen by a slanted camera.

Results

The averaging of two slanted views yielded the graph in Figure 7. This method is relatively accurate for gradual changes in the ice surface. Thus, the overall shape is fairly accurate. However, for sudden changes in the surface radius, such as occurs between 225-275 degrees, the average values are unable to accurately predict the surface. This could be because, were the nonuniformity to occur between points C and B of Figure 6, the camera using the blue view would be able to detect the nonuniformity, but the camera using the red view would not. However, if the camera was equatorial, this problem would not occur.
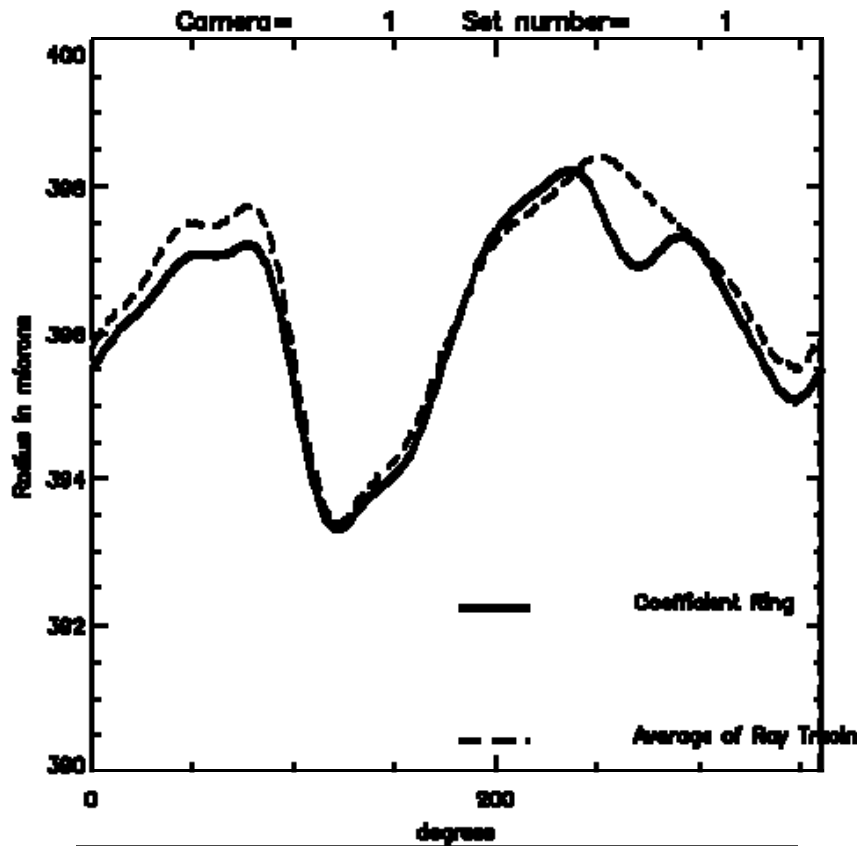

Fig.7: The actual surface (solid graph) vs. average of two slanted views (dotted graph).

Conclusion

The average of opposite views using the camera at 0 degrees yielded excellent results, with an error of about 0.2 microns. The averaging of opposite views using the slanted camera works relatively well for gradual non-uniformities (modes up to n = 5). Thus, the program is able to predict changes in the thickness of the ice layer that occur slowly over a large area. However, if there are irregularities localized to a small area, the camera may be situated so that the defect can only be seen in one view. Thus, slanted cameras view different surface perturbations than equatorial ones. Improved characterization is possible with two slanted views, but only for long-wavelength nonuniformities.

Acknowledgements

References

[1] Jin, Sharon "A Ray-Tracing Model for Cryogenic Target Uniformity Characterization" 2002 Summer High School Research Program at the University of Rochester Laboratory for Laser Energetics.

[2] Balonek, Gregory J. "How Good is the Bright Ring Characterization for Uniformity of Deuterium Ice Layers within Cryogenic Nuclear Fusion Targets?" 2004 Summer High School Research Program at the University of Rochester Laboratory for Laser Energetics.